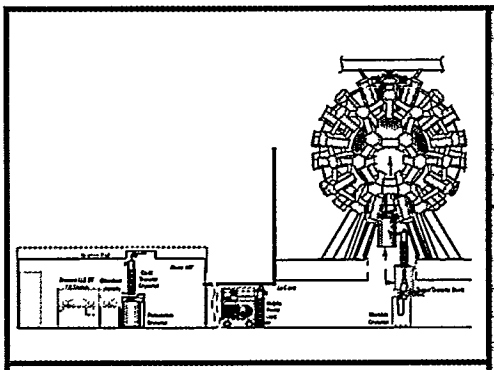

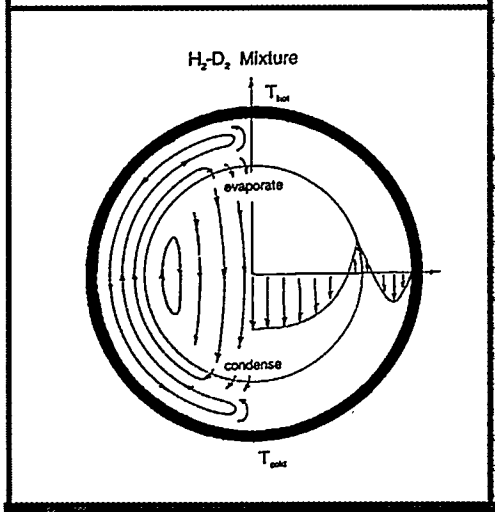

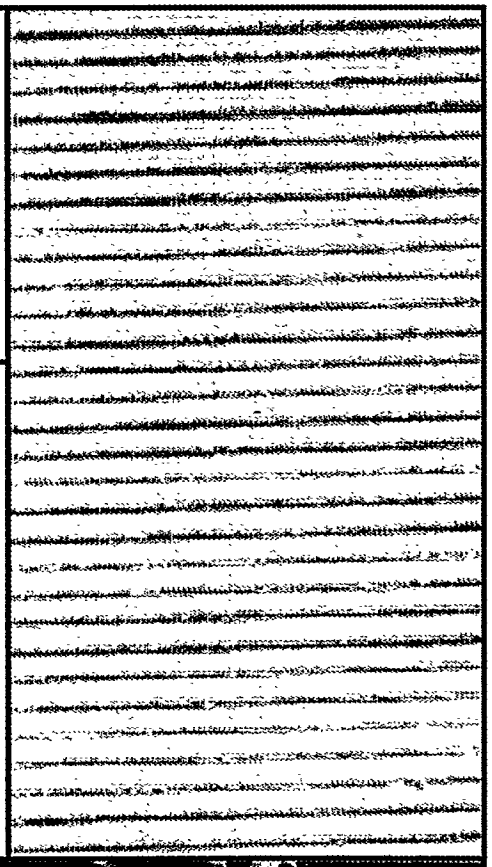

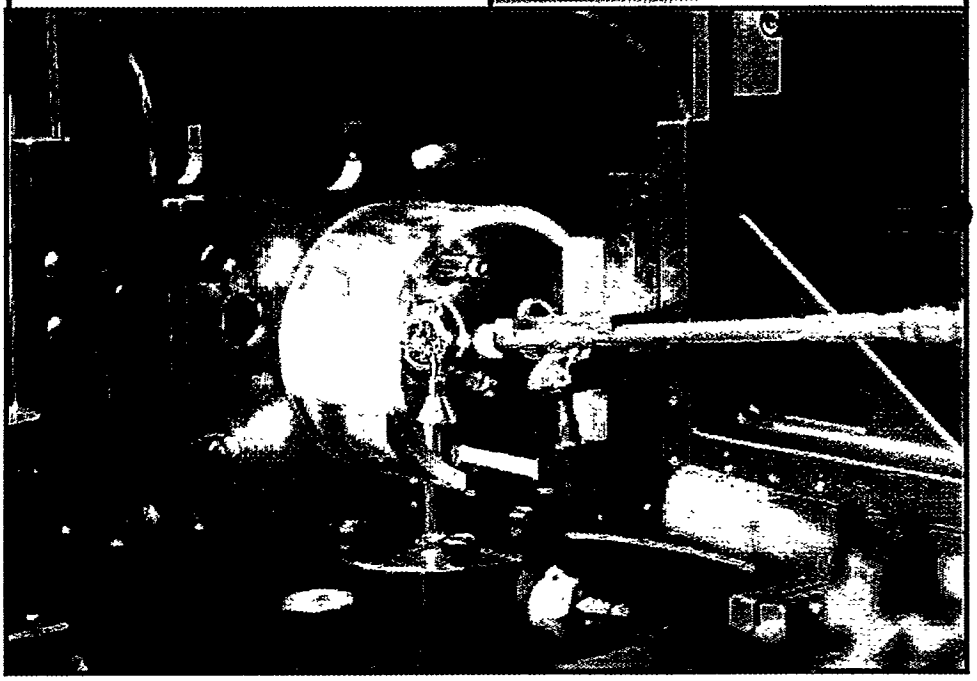

INERTIAL CONFINEMENT FUSION

ANNUAL REPORT

OCTOBER 1, 1994
THROUGH
SEPTEMBER 30, 1995

W. J. SCHAFER ASSOCIATES, INC.
Soane Technologies Inc.
GENERAL ATOMICS

GA–A22305
UC-712

INERTIAL CONFINEMENT FUSION TARGET COMPONENT FABRICATION AND TECHNOLOGY DEVELOPMENT SUPPORT

ANNUAL REPORT TO THE U.S. DEPARTMENT OF ENERGY

OCTOBER 1, 1994 THROUGH SEPTEMBER 30, 1995

by
PROJECT STAFF
Martin Hoppe, Editor

Work prepared under
Department of Energy
Contract No. DE-AC03-91SF18601

GENERAL ATOMICS PROJECT 3896
DATE PUBLISHED: MAY 1996

GENERAL ATOMICS

The FY1995 ICF Target Fabrication and Target Technology Development Team

General Atomics
San Diego, California

Neil Alexander, Wes Baugh, Chuck Beal, Don Beighley, Gary Bentley, Dave Bernat, Gottfried Besenbruch, Karl Boline, Lloyd Brown, Don Czechowicz, Sharon Considine, Fred Elsner, Bob Fagaly, Mark Foster, Chuck Gibson, Jane Gibson, Kett Gifford, Ileese Glatter-Schneir, Steve Grant, Matt Hansink, Martin Hoppe, Dave Husband, Jim Kaae, Greg Laughon, Jim Lindgren, Roy Mangano, Barry McQuillan, Wayne Miller, Abbas Nikroo, Lonnie O'Brien, Joe Pontelandolfo, John Ruppe, Chuck Schneidmuller, Ken Schultz, Clyde Shearer, John Sheliak, Richard Stephens, David Steinman, Bob Stemke, Ted Torres, John Vanderzanden, Don Wall, David Woodhouse, Wane Wier.

W. J. Schafer Associates
Livermore, California

Tom Alberts, Thom Bahrs, Bob Bieri, Don Bittner, John Burmann, Frank Carey, Brendan Casey, Andrea Denton-Paul, David Diffenderfer, Steve Dropinski, Illges Faron, Scott Faulk, Chuck Hendricks, Barbara Lane, Derek Mathews, Michael McClellan, Michael Monsler, Brian Motta, Craig Rivers, Jim Sater, Diana Schroen-Carey, Keith Shillito.

Soane Technologies, Inc.
Hayward, California

Travis Boone, Lisa Cheung, Don Nelson, Thai Nguyen.

ABSTRACT

On December 30, 1990, the U.S. Department of Energy entered into a contract with General Atomics (GA) to be the Inertial Confinement Fusion (ICF) Target Component Fabrication and Technology Development Support contractor. This report documents the technical activities of the period October 1, 1994 through September 30, 1995. During this period, GA was assigned 15 tasks in support of the Inertial Confinement Fusion program and its laboratories. A portion of the effort on these tasks included providing direct "Onsite Support" at Lawrence Livermore National Laboratory (LLNL), Los Alamos National Laboratory (LANL), and Sandia National Laboratory Albuerque (SNLA).

The ICF program is anticipating experiments at the National Ignition Facility (NIF) and the OMEGA Upgrade. Both facilities will require capsules containing layered D_2 or deuterium-tritium (D-T) fuel. We are part of the National Cryogenic Target Program to create and demonstrate viable ways to generate and characterize cryogenic layers. Progress has been made on ways to both create viable layers and to characterize them.

We continued engineering, assembly and testing of equipment for a cryogenic target handling system for University of Rochester's Laboratory for Laser Energetics (UR/LLE) that will fill, transport, layer, and characterize targets filled with cryogenic fuel, and insert these cryogenic targets into the OMEGA Upgrade target chamber for laser implosion experiments.

This report summarizes and documents the technical progress made on these tasks.

TABLE OF CONTENTS

TABLE OF CONTENTS (CONTINUED)

TABLE OF CONTENTS (CONTINUED)

LIST OF FIGURES

LIST OF FIGURES (CONTINUED)

LIST OF FIGURES (CONTINUED)

LIST OF FIGURES (CONTINUED)

LIST OF FIGURES (CONTINUED)

LIST OF TABLES

1. TARGET FABRICATION PROGRAM OVERVIEW

On December 30, 1990, the U.S. Department of Energy (DOE) entered into a contract with General Atomics (GA) to be the Inertial Confinement Fusion (ICF) Target Component Fabrication and Technology Development Support contractor. This report documents the technical activities of the period October 1, 1994 through September 30, 1995. GA was assisted by W.J. Schafer Associates (WJSA) and Soane Technologies, Inc. (STI) and we have carried out the ICF Target Fabrication tasks as a fully integrated team effort.

1.1. INTRODUCTION

In FY95, the GA/WJSA/STI team maintained previous production capabilities in all areas of ICF target fabrication. In addition, in several areas of target fabrication we have developed and/or added new capabilities.

1.2. FY95 TASKS SUMMARY

During FY95, the GA/WJSA/STI team was assigned 15 formal tasks, as shown in Table 1–1. These tasks are described briefly here. Additional technical detail on selected topics is given in Sections 2 through 6 of this report.

1.2.1. LL01 ONSITE SUPPORT FOR LLNL

Our onsite team at Lawrence Livermore National Laboratory (LLNL), composed of Andrea Denton-Paul, Steve Grant, Craig Rivers, Derek Mathews, and John Ruppe, emphasized activities in micromachining of target components, assembling target components into complete targets, and characterizing target components and capsules to assure their quality for use in NOVA ICF experiments.

TABLE 1–1
FY95 TARGET FABRICATION TASKS

Task No.	Task Title Description	Total $K	Task Leader
LL01	Onsite support for LLNL	561	Miller
LL02	Micromachined target components	1,012	Kaae
LL03	Composite polymer capsules	768	Miller
LA01	Onsite support for Los Alamos National Laboratory (LANL) at LLNL	144	Miller
LA02	Composite polymer capsules	793	Miller
NR01	NRL target development	899	Hendricks
SL01	Fabrication of foils, filters, and hohlraums	873	Kaae
UR01	Polymer capsules for Laboratory for Laser Energetics (LLE)	914	Miller
UR02	Production of large polymer shells	190	Nelson
CR/LL1	Cryogenic layering development	830	Bittner
CR/LL2	Foam shell development	304	Schroen-Carey
CR/LA1	Beta layering support at LANL	208	Simpson
CR/LA2	Deuterium-tritium (D-T) layer characterization by NMR	105	Alexander
CR/UR1	OMEGA-Upgrade target system eng.	2,487	Fagaly
CR/UR2	Shell characterization development	76	Stephens
	Total	10,164	

1.2.2. LL02 MICROMACHINED TARGET COMPONENTS

Our production of gold-plated hohlraum mandrels met the needs of LLNL and Los Alamos National Laboratory (LANL). These mandrels take the form of many different shapes, but they generally have the requirements that the specified dimensions, including gold coating thickness, be controlled to about ±5 μm. Surface finishes must be better than 1000 Å RMS. We usually achieve dimensional control to ±2 μm, better than the specified tolerances. The surface finishes are also better than those specified with surface roughness about 200 Å rms routinely achieved.

We delivered seven hundred and two (702) gold-plated mandrels of 31 different kinds to LLNL this fiscal year, and 68 mandrels of two different kinds to LANL.

Production of witness plates has not proceeded as well as the production of hohlraum mandrels. There are a number of reasons for this, among which are:

1. Until the first of this year, the Rocky Flats #3 lathe did not operate consistently after it was transferred from Rocky Flats to WJSA.

2. The Rocky Flats #2 lathe has been out of operation since early this year due to a controller failure.

3. The LLNL sputter coater which was used to prepare substrates for the machining of witness plates has been out of operation since the middle of the year.

In spite of these problems, a pair of high-quality Rayleigh-Taylor molds and a set of acceptable plastic witness plates were delivered to LLNL. A few acceptable aluminum witness plates, produced by a direct machining technique that bypassed the need for sputter coating, were also delivered. However, questions remain about whether the direct machining technique can reliably meet the thickness tolerances required for witness plates. Efforts to resolve this question are ongoing. Also, the LLNL coater will be operational again early in FY96, and we plan to use it to prepare sputtered aluminum substrates for witness plate machining as soon as possible.

We also produced copper sine-wave plates by direct machining which were delivered to LLNL. While these sine-wave plates were used in NOVA tests, the sine-waves were slightly distorted. We are working to understand the reason for the distortion so that it can be eliminated.

Tests have shown that our Precitech lathes do not produce as good surface finishes as the Rocky Flats #3 lathe or modern Precitech lathes. The DOE-owned Precitech lathe has been returned to the factory for upgrading to improve the capability of the lathe for producing the fine surface finishes needed for witness plates. In the meantime, hohlraum mandrel production has been switched to the GA-owned Precitech lathe.

1.2.3. COMPOSITE POLYMER CAPSULES

With the upgrade of the OMEGA laser, University of Rochester's/Laboratory for Laser Energetics (UR/LLE) joined LLNL and LANL in requiring target-quality capsules for experiments. Not surprisingly, capsule deliveries dominated our efforts throughout the year, especially after April when OMEGA came on-line, as shown in Fig. 1–1. Overall, we

delivered nearly three times more composite polymer capsules in FY95 than in FY94, as shown by Fig. 1–2. In addition to the composite polymer shells, glass shell production at GA became a significant effort. We developed a way to make target quality glass shells over 1500 μm diameter that were strong enough to survive a 45 atm burst test. We delivered 153 selected and characterized glass shells plus four batches of uncharacterized glass shells.

LL03 Composite Polymer Shells For LLNL. The goal of this task was to manufacture, characterize, and deliver low-z fuel capsules required by LLNL and to develop improvements in the manufacturing process. GA made 15 capsule deliveries with specifications shown in Table 1–2. This is an increase over the six deliveries in FY94. In all we delivered 199 polymer composite capsules and one batch of glass shells, compared to 104 composite capsules in FY94. The capsules were in many nstances more complex, taking advantage of newly developed or improved processes. Some of the complexities were inner mandrels doped with titanium (P-37), outer layer of glow discharge polymer (GDP) doped with

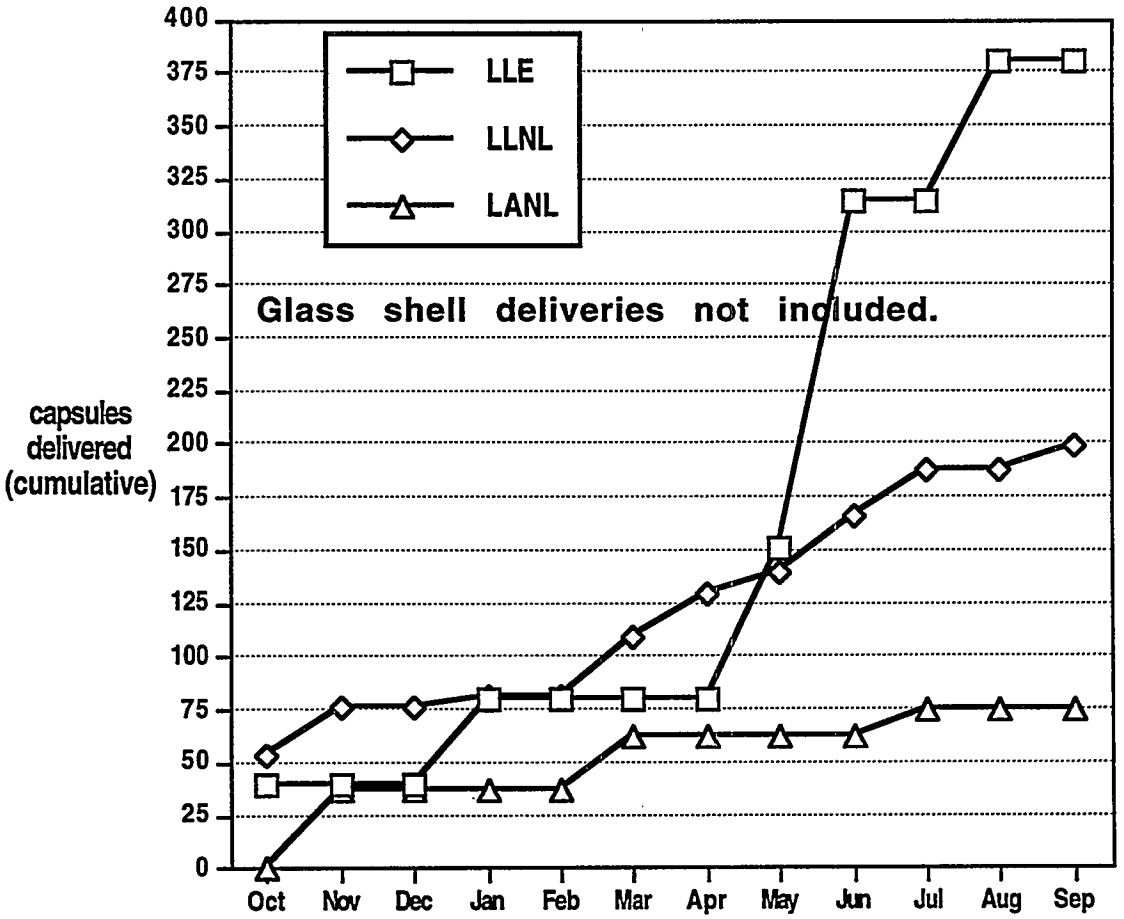

Fig. 1–1. Composite polymer capsule deliveries in FY95.

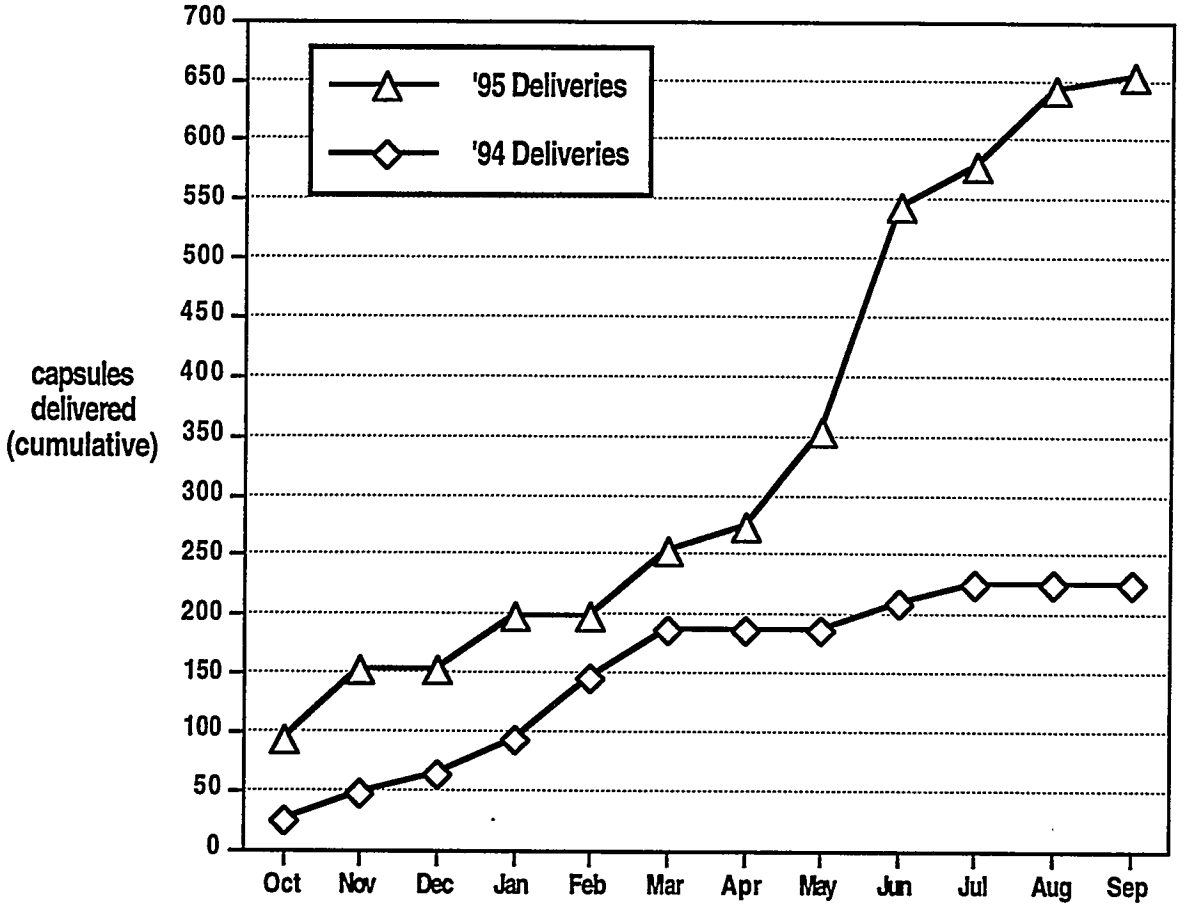

Fig. 1–2. Composite capsule deliveries were nearly three times greater in FY95 than in FY94.

germanium (P-23, P-27, P-28, P-33, P-38, andP-61), diagnostic gas mixtures (P-21, Ar/Ne; P-35, Xe; and P-48, Ar/CD_4), and capsules selected for low permeability to deuterium (P-33 and P-34).

The titanium-doped and germanium-doped capsules are products of the R&D efforts in FY94. The techniques are described in last year's report.

The new diagnostic gas mixtures were possible due to a new technique. Previously we filled capsules with argon, the diagnostic gas, before the shells were coated with the permeation barrier polyvinyl alcohol (PVA). This process resulted in significant pressure differences from shell to shell. This year we filled the capsules after the PVA and the CH layers were deposited, by heating the capsules and permeating the diagnostic gas into the capsule. This technique virtually eliminated shell-to-shell variations in diagnostic gas pressure, and also allowed fills with precise mixtures.

TABLE 1–2
LLNL CAPSULE DELIVERIES

Item	Shell Type	Fill Pressure (atm)	Total Wall Thickness (Mandrel + PVA + CH)	Comments $\Delta w = w_{max} - w_{min}$ Background SF ≤ 1000 Å	No. Sent
P-20	PS	0.10 ± 0.03 Ar	62 ± 3 μm CH	Total Δw ≤ 6 μm	13
P-21	PS	0.10 ± 0.03 Ar 10.0 ± 1.0 Ne	62 ± 3 μm CH	Total Δw ≤ 6 μm	14
P-22	PS	0.05 ± 0.02 Ar	58 ± 3 μm CH	Total Δw ≤ 6 μm	10
P-23	PS	0.05 ± 0.02 Ar	43 ± 3 μm CH	2 ± 0.5% Ge in GDP Total Δw ≤ 5 μm	17
P-27	PS	0.05 ± 0.02 Ar	45 ± 3 μm CH	1.26 ± 0.25% Ge in GDP Total Δw ≤ 5 μm	22
P-33	PS	0.05 ± 0.02 Ar	45 ± 3 μm CH	1.26 ± 0.25% Ge in GDP Total Δw ≤ 5 μm D_2 perm. $t_{1/2}$ ≥ 30 hr	12
P-34	PS	0.05 ± 0.02 Ar	65 ± 5 μm CH	Total Δw ≤ 5 μm D_2 perm. $t_{1/2}$ ≥30 hr	16
P-35	PS	12.5 ± 2.5 Xe	~20 μm CH	Not target quality	6
P-37	PS with 0.07±.03% Ti	0.05 ± 0.02 Ar	59 ± 4 μm CH	Total Δw ≤ 5 μm	16
P-38	PS	0.05 ± 0.02 Ar	43 ± 3 μm CH	1.25 ± 0.25% Ge in GDP Total Δw ≤ 5 μm	20
P-39	PS	0.12 ± 0.03 Ar	55 ± 3 μm CH	Total Δw ≤ 5 μm	10
P-48	PS	0.10 ± 0.03 Ar 10.0 ± 1.0 CD_4	62 ± 3 μm CH	Total Δw ≤ 6 μm	10
P-54	PS	0.10 ± 0.03 Ar	62 ± 3 μm CH	Total Δw ≤ 6 μm	22
P-61	PS	None	43 ± 3 μm CH	1.25 ± 0.25% Ge in GDP Total Δw ≤ 5 μm	11
LLNL 6/95	Glass	None	N/A	1,000 ± 50 μm (o.d.) 4 ± 3 μm (wall)	1 batch

We developed a new technique for selecting the capsules with lower permeability to deuterium. Previously, the permeation rate was determined by interferometry or dew point techniques. Those techniques were time consuming and/or prone to error. However, determining the permeation rate of argon was relatively fast and accurate using x-ray fluorescence (XRF). Thus we determined the ratio of the permeation rate of argon at 113°C to deuterium at room temperature. The results are shown in Fig. 1–3. Using this relationship

we determined the permeation rate of capsules for argon and selected the ones with the lowest permeability for D-T fills.

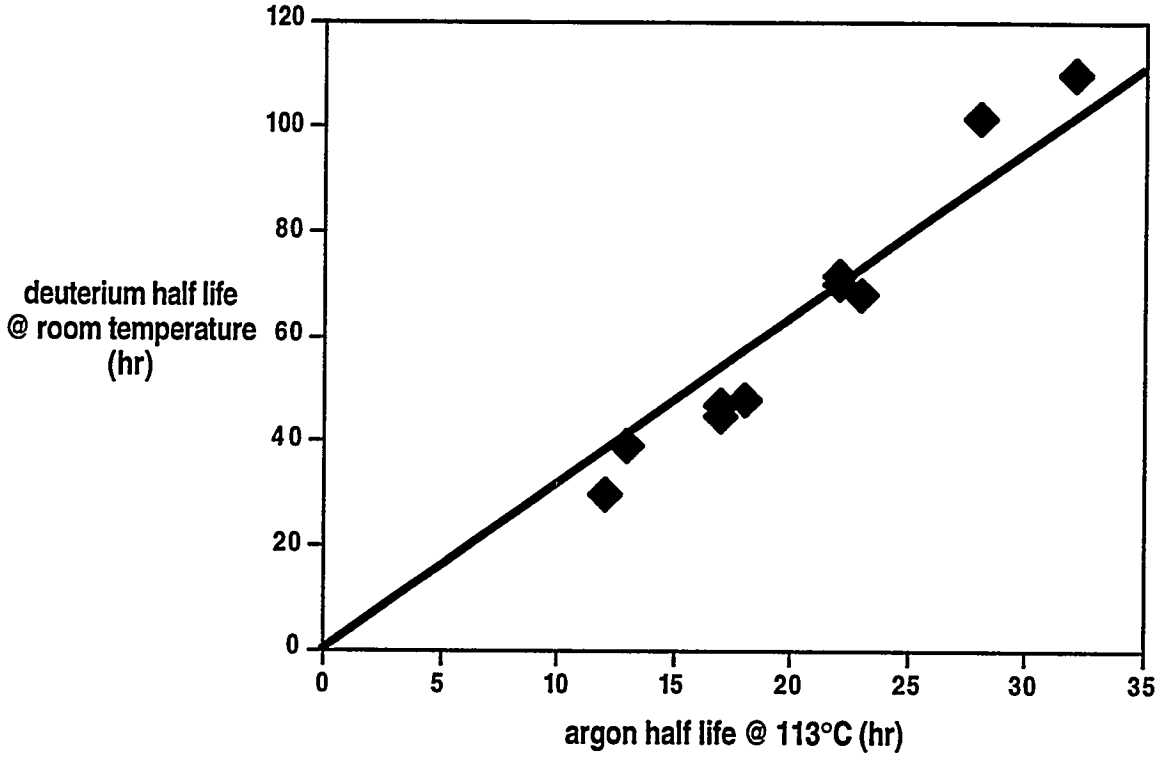

Fig. 1–3. The relationship between the permeation half life for argon at about 113°C to the permeation half life for deuterium at room temperature is highly correlated. Since analysis for argon is more rapid, and may be more precise, we selected capsules for lower permeability for deuterium by determining the permeability for argon and applying the relationship show in this figure.

LA02 Composite Polymer Shells For LANL. The goal of this task was to manufacture, characterize, and deliver low-z fuel capsules required by LANL and to develop improvements in the manufacturing process. GA made four composite capsule deliveries and three glass shell deliveries with specifications shown in Table 1–3. In all we delivered 55 polymer composite capsules and 97 glass shells, compared to 100 composite capsules in FY94.

A major development in these deliveries compared to FY94 was in glass shells. LANL required larger glass shells than had been made in the program before. Previously, water vapor was used to increase shell diameters. We combined helium with water vapor and made target-quality shells over 1,500 μm diameter, a significant increase over the previous limit, as

TABLE 1-3
LANL CAPSULE DELIVERIES

Item	Shell Type	Fill (atm)	Wall Thickness (Mandrel + PVA + CH)	Comments $\Delta w = w_{max} - w_{min}$ Background SF ≤ 1000 Å	No. Sent
P-28	Deuterated PS	0.10 ± 0.03 Ar	45 ± 3 μm CH	1.3 ± 0.3% Ge in GDP Total Δw ≤ 5 μm	17
P-29	Deuterated PS with 1 at. % Cl	0.10 ± 0.03 Ar	55 ± 5 μm CH	Total Δw ≤ 5 μm	15
P-36	Deuterated PS	0.05 ± 0.03 Ar	45 ± 3 μm CH	1.3 ± 0.3% Ge in GDP Total Δw ≤ 5 μm	11
P-55	Deuterated PS	0.05 ± 0.03 Ar	55 ± 3 μm CH	Total Δw ≤ 6 μm	12
LANL 4/95	Glass	None	N/A	>1,200 μm (o.d.) 3.5 ± 2.5 μm (wall) Survive 45 atm burst test	43
G-11	Glass	None	N/A	≥1,200 μm (o.d.) 3.3 ± 1.3 μm (wall) Survive 45 atm burst test	20
G-12	Glass	None	N/A	675 ± 50 μm (o.d.) 5.5 ± 1.0 μm (wall)	34

shown in Fig. 1–4. On July 26, these shells were used to set a world's record for the highest neutron yield from an ICF experiment, 3.6×10^{13} neutrons on NOVA.

UR01 Composite Polymer Capsules For UR/LLE. The goal of this task was to manufacture, characterize, and deliver low-z fuel capsules required by UR/LLE as shown in Table 1–4. In addition, we were to develop chlorine-doped GDP layers, and to transfer and develop the capability to make GDP shells by the depolymerizable mandrel technique. In all we delivered 380 polymer composite capsules. We also delivered 56 selected and characterized glass shells and three batches of glass shells. One of the batches, LLE 5/95, consisted of 14 ml of glass shells. On August 11, one of the glass shells was used to set a world's record for the highest neutron yield from an ICF experiment, 5.0×10^{13} neutrons on OMEGA.

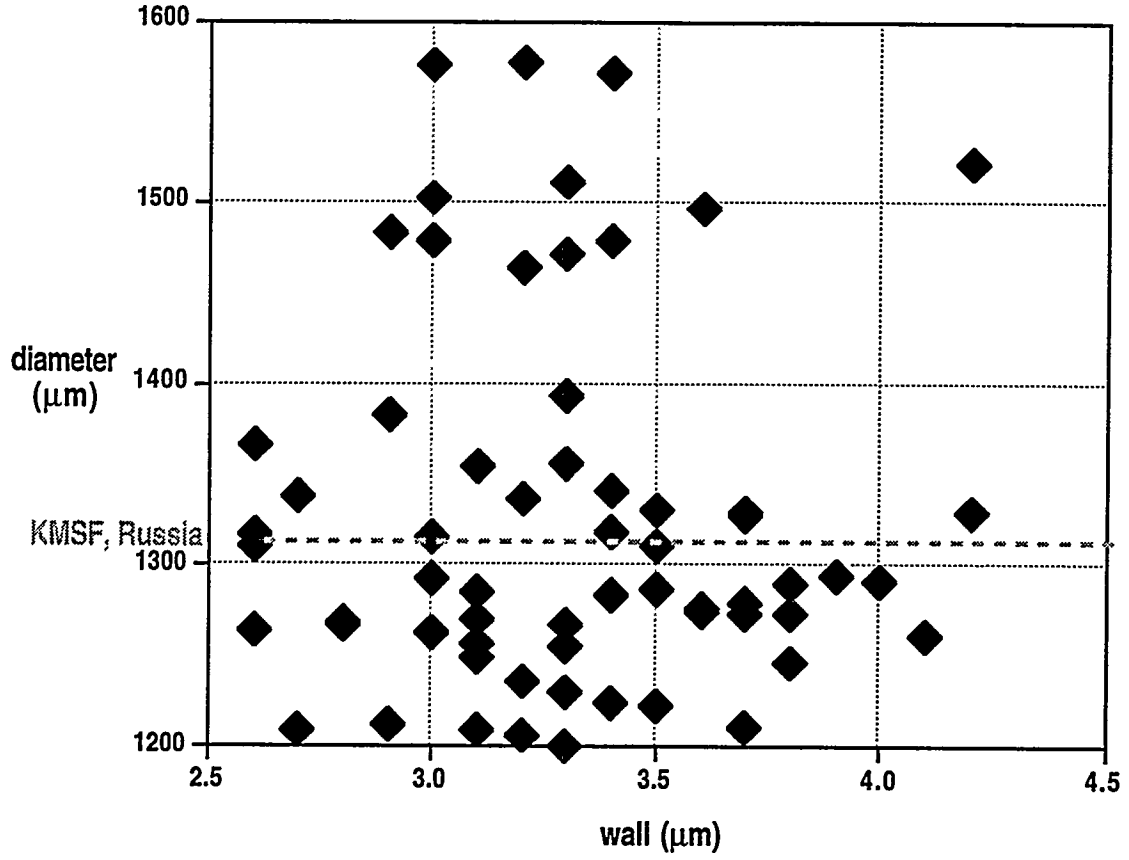

Fig. 1-4. Large, target quality, glass shells delivered to LANL. Previously the largest glass shells were made at KMS Fusion (KMSF) and Russia. These shells, prepared in an atmosphere of water vapor and helium, were strong enough to survive a 45 atm burst test.

Developing a technique for doping GDP with about six atomic percentage chlorine was a major effort. We constructed a new coater for this development and for later production. We tested seven different dopant compounds for their effect on chlorine concentration in the layer, stress, optical clarity, and surface finish. Coating parameters were also explored with each dopant. Finally we found acceptable conditions. We will begin applying chlorine-doped GDP to composite polymer capsule targets in FY96.

1.2.4. LA01 ONSITE SUPPORT FOR LANL AT LLNL

Kett Gifford worked with our onsite team at LLNL, but primarily on LANL targets where he assembled and characterized numerous targets.

TABLE 1–4
UR/LLE CAPSULE DELIVERIES

Item	Shell Type	Mandrel ID (μm)	Total Wall Thickness (Mandrel + CH)	Comments	No. Sent
P-24	PS	~1000	10 ± 2 μm GDP	Background SF ≤1000 Å	20
P-25	PS	~1000	20 ± 3 μm GDP	Background SF ≤1000 Å	20
P-30	PS	~1000	10 ± 3 μm GDP	Background SF ≤1000 Å 15 atm pressure test	13
P-31	PS	~1000	20 ± 3 μm GDP	Background SF ≤1000 Å 15 atm pressure test	14
P-32	PS	~1000	30 ± 3 μm GDP	Background SF ≤1000 Å 15 atm pressure test	13
P-40	PS	800–940	2.5 ± 1 μm of GDP	12 atm He burst test	20
P-41	PS	870–890	7.0 ± 1 μm of GDP	10 atm He burst test	9
P-42	PS	870–910	10.0 ± 1 μm of GDP	10 atm He burst test	13
P-43	PS	830–910	13.5 ± 1 μm of GDP	10 atm He burst test	29
P-44	PS	910–970	7.0 ± 1 μm of GDP	10 atm He burst test	25
P-45	PS	900–920	10.0 ± 1 μm of GDP	10 atm He burst test	10
P-46	PS Bead	N/A	10.0 ± 1 μm of GDP	2.75 ± 0.25 Ge in GDP 900 ± 25 μm final diameter	37
P-47	PS Bead	N/A	12.0 ± 1 μm of GDP	2.75 ± 0.25 Ge in GDP 900 ± 25 μm final diameter	14
P-49	PS	870–905	2.5 ± 1 μm of GDP	10 atm He burst test	23
P-50	PS	885–925	11 ± 1 μm of GDP	10 atm He burst test	28
P-51	PS	845–880	Batch average = 30 ± 2.5 μm	10 atm He burst test	13
P-52	PS	880–900	Batch average = 40 ± 2.5 μm	10 atm He burst test	7
P-53	PS	880–925	Batch average = 50 ± 2.5 μm	10 atm He burst test	7
P-56	PS	786–820	Batch average = 30 ± 2.5 μm	10 atm He burst test	14
P-57	PS	790–820	Batch average = 40 ± 2.5 μm	10 atm He burst test	7
P-58	PS	781–815	Batch average = 50 ± 2.5 μm	10 atm He burst test	6
P-59	PS	797–814	Batch average = 20 ± 2.5 μm	25 atm He burst test	18
P-60	PS	790–815	Batch average = 30 ± 2.5 μm	40 atm He burst test	20
LLE 2/95	Glass	850–200	5 ± 4 μm		Batch
LLE 5/95	Glass	900±200	5 ± 4 μm		Batch
G-10	Glass	900±100	5 ± 4 μm		56
G-10	Glass	900±100	5 ± 4 μm		B

1.2.5. NR01 NRL TARGET DEVELOPMENT AND DELIVERIES

This task is divided into two subtasks: (a) target production and (b) characterization development. The NIKE laser has become fully operational during this fiscal year and, therefore, a continuous flow of targets has been required for the NIKE experimental program. During FY95 the targets listed Table 1–5 were delivered to NRL for use in the NIKE laser program.

TABLE 1–5
NIKE TARGET DELIVERIES

Single foil targets	214
Double foil targets	81
Un-cut films on silicon wafers	5
Cut film (un-mounted foils ready to mount)	161
One inch square characterized films	3

There are several instruments available which employ various techniques for the examination of the morphology of surfaces. These include interferometers, atomic force microscopes, various stylus instruments, and other optical microscopes. We have elected to use the Photon Tunneling Microscope (PTM) as the best instrument by which to characterize the surface of the foils used in the NIKE targets. This instrument has been discussed at length in various publications in recent times regarding both theoretical discussions of the PTM instrument and practical aspects of the using the PTM for the examination of surfaces. PTM's have vertical resolutions of tenths of a nanometer and a circular, lateral field of view about 100 μm diameter. The addition of a charge coupled device (CCD) array camera to the PTM allows us to store and analyze the target surface data directly with the aid of a computer. The computer files can also be sent, electronically, directly to NRL for their use and analysis.

1.2.6. SR01 FABRICATION OF FOILS, FILTERS AND HOHLRAUMS

This task was broken down into six subtasks which are described below.

1. Fabrication of foils
2. Deuterated GDP coatings
3. Onsite Support for Sandia National Laboratories (SNL)

4. Diamond-turned break-out plates
5. Fabricate hohlraum caps
6. Fabricate hohlraums

Fabrication of Foils. Ninety-six (96) foils were fabricated, characterized and delivered to SNL in the Fabrication of Foils Task. These foils consisted of 1.0 μm of gold on 1.5 μm thick Mylar mounted on 2-in. diameter brass retaining rings. The thickness of both the gold and the Mylar were measured on each foil using alpha spectrometry, and each foil was inspected to ensure the absence of pinholes in the gold.

Deuterated GDP Coatings. In the second task, a process was developed to coat SNL acrylic hohlraum mandrels after they initially had been coated with 1.5 μm of gold. A GDP shell coater was modified for the purpose by replacing the pan used to hold the shells with a small rotator to spin the mandrel during coating. In addition, the bottom end of the coater tube was expanded out in a bell shape which produced a more uniform coating distribution over the mandrel. Deuterium and deuterated butane were used as gas feedstock to the coater. Conditions for coating mandrels with a nearly uniform coating were developed. Then, three gold-coated mandrels were coated with deuterated GDP and were delivered to SNL for evaluation.

Onsite Support for SNL. One scientist (T. Alberts) was assigned to SNL full time. His assignments were to fabricate foils to satisfy urgent needs, to act as a liaison between GA and the experimenters at SNL, helping to set specifications, and to receive shipments form GA and to distribute them. In addition, he fabricated and assembled complex SNL targets.

Diamond Turned Break-Out Plates. Aluminum-coated polycarbonate witness plates with both wedge and step profiles were produced by diamond machining followed by sputter coating in the fourth subtask. Since sufficiently thick polycarbonate sheet stock was not readily available, and there was an immediate need for the witness plates, acceptable but thinner than desired witness plates were delivered. Fabrication of witness plates meeting the specifications was underway at the end of the fiscal year.

Fabricate Hohlraum Caps and Hohlraums. Conventional machining followed by polishing was replaced by diamond turning in the fabrication of both hohlraum caps and hohlraums. This allowed us to achieve better dimensional control with a better surface finish. Sixteen (16) hohlraum caps, where the 12 μm of gold coating was applied first by sputtering on a thin layer and then electroplating, were delivered to SNL this year. Also, fifteen (15)

hohlraums were delivered to SNL this year. After coating with 1.5 μm of gold by sputtering some of these were coated with 3 μm of parylene N, some were coated with 3 μm of parylene D, and some were coated with 3 μm of deuterated GDP.

1.2.7. UR02 PRODUCTION OF LARGE POLYMER SHELLS

The previous year (FY94) we demonstrated the capability to produce polystyrene shells with target quality diameters, wall thicknesses, sphericities, and concentricities via controlled-mass microencapsulation. In order to provide target mandrels meeting the specifications of the Omega Upgrade program, the goals of this year's (FY95) task were to: (a) limit shell diameters to 850–1000 microns; (b) reduce the levels of vacuoles, dimples, and debris; and (c) make initial deliveries to from STI to GA for subsequent coating operations.

We have been successful in all of these areas. The triple-orifice, originally designed to produce 1–2 mm diameter shells, was redesigned to achieve the desired 850–1000 μm dimension. Vacuoles were reduced by extensive (sub-micron) filtering of the shell-making solutions and limiting the wall thickness. Dimpling was avoided by lowering the shell solidification temperature and adopting a less aggressive ethanol-water extraction procedure. Environmental debris levels have been reduced through use of a HEPA-filtered shell handling area and a filtered shell drying chamber.

During the last three months of FY95, the five scheduled deliveries to General Atomics were fulfilled. All specifications for the initial Omega Upgrade mandrel requests were met. According to Wayne Miller of GA, the surface finishes following subsequent GDP coating are within current target specifications. According to Mark Whitman at LLE, our polystyrene shells are now the best microencapsulated shells within the ICF community.

1.2.8. CR/LL1 CRYOGENIC LAYERING DEVELOPMENT

Solid D-T layering experiments have been performed in 1 mm and 2 mm toroidal geometry in order to provide data relevant to the requirements of the LLE Omega Upgrade system at the University of Rochester. The first toroidal cell design includes a 1 mm i.d. toroidal bore and low thermal conductivity windows to prevent solid D-T buildup on the windows with resulting distortion of the layer image. In addition, the front window was heated with an integral thin film heater to insure a solid-free optical path if necessary. Data has been analyzed for equilibrated and temperature stepped surface roughness. The results show that a 110 μm toroid layer has about a 1.2 μm rms roughness which is a slightly better

surface than was observed in the previous re-entrant type cell. At modes above P10, the surface roughness drops below 1 μm for the torus. Later data have shown that this geometry can produce D-T layers with surface roughness below 1 μm rms.

Lessons learned previously were applied to the design of the 2 mm torus, which included an integral axial heating element to permit studies of layer smoothing with external heating mechanisms. This cell has virtually eliminated the light piping and light scattering effects observed in the 1 mm torus. It also prevents D-T solid from wrapping onto the front window in the region where this solid could distort the image of the layer edge of interest. Additionally, a new illumination system allows precise focusing of the illumination beam so that there is very little internal light scattering and only the layer edge region of interest is illuminated. This cell also permitted, for the first time, studies of the surface roughness inherent in native beta-layering (no external heating), as well as surface roughness attainable using varying levels of external heating.

In addition, a 2 mm hemi-spherical cell design was tested. The 2 mm hemi was designed to permit studies of D-T solid layering in spherical geometry without the imaging distortions that are inherent in full spherical cells. This cell is NIF (National Ignition Facility) size and includes a low conductivity front window to prevent solid D-T buildup obscuring the optical path and distorting the image of the layer edge of interest. This window was only partially successful in preventing solid from distorting the layer image, since a small amount of solid did wrap onto the window in the region of the layer edge. Additionally, the cell contained low mode defects which imprinted on the layer, making the measurement of layer surface roughness very difficult and inconclusive.

Detailed discussion of the results of these experiments are presented in Section 5.

1.2.9. CR/LL2 FOAM SHELL DEVELOPMENT

The foam shell development task is a joint task with LLNL to produce foam capsules appropriate for cryogenic layering experiments associated with the National Cryogenic Program. The capsule designs have hollow interiors, 90 to 100 μm foam walls, 5 to 10 μm solid barrier overcoats and final diameters of 1 to 2 mm. Areas of concern include optical transparency, wall uniformity and sphericity, and final surface finish. In 1995 we pursued two different foam systems for making foam shells: ethylenedimethacrylate (EGDM) and resorcinol-formaldehyde (RF). We were unable to develop small enough foam cell size with the EGDM foam to allow optical transparency and so focused our resources on the RF sys-

tem. Optical transparency has been demonstrated for resorcinol-formaldehyde foam mandrels of the desired sizes. Production capability has been developed for this mandrel using droplet generator technology. Various overcoating technologies are being explored and results are presented in Section 5.

1.2.10. CR/LA1 BETA LAYERING SUPPORT AT LANL

The beta-layering work at LANL during FY95 has included four individual experiments, one involving the measurement of the optical system Point Spread Function (PSF), and three solid layering experiments performed in differing cell geometries. All work completed has been in support of the beta-layering program at LANL, under the direction of Jim Hoffer, and has focused on the attempt at production and characterization of D-T solid layers with surface roughness of less than 1 μm rms.

An important aspect of the measurement of D-T solid surface roughness has been the attempt to improve measurement resolution, i.e. to more precisely determine surface roughness. This would allow us to more closely monitor the layering process, including the effects of D-T cell temperature and layer surface smoothing techniques on rms roughness. These schemes have, in general, improved our ability to view the layer edge and make more precise measurements of D-T solid layer surface roughness. In the latest series of heat-enhanced solid layering experiments in toroidal geometry, these schemes have enabled us to measure surface roughness to a resolution of about 0.25 μm rms.

D-T solid layering experiments have been conducted in 1 mm toroidal and 2 mm hemispherical geometries, and are continuing in a 2 mm toroidal geometry. In all cases an unobstructed and non-distorted view of the layer edge was obtained by using a low thermal conductivity cell window in the optical path, which remained warmer than the cell and thereby clear of D-T solid. In addition, the 2 mm toroidal cell was designed to eliminate the "light piping" observed in the 1 mm torus (causing an ambiguous layer edge location), and included a new illumination scheme to permit precise back illumination of only the layer edge of interest. The use of these new cell geometries has provided the clearest view of the D-T layer yet, and has produced surface roughness measurements down to 0.25 μm rms.

1.2.11. CR/LA2 D–T LAYER CHARACTERIZATION BY NMR

This task was to characterize samples of D-T for possible isotopic fractionation occurring during the beta-layering symmetrization procedure. A doubly tuned, one-dimensional (1-D)

spatially resolved NMR probe was used for this study. By resonating the probe with the deuteron and triton resonant frequencies, it is possible to determine the ratio of deuterium to tritium with respect to elevation within the sample.

The NMR probe that was designed and built last year leaked upon cool down. This leak was found to be in the fill capillary. The capillary line was re-designed and the probe was re-built in the new configuration. To fit the existing sample cell and probe, some of the capillary was custom made. The new probe survived the thermal shock of cool-down with liquid nitrogen without leaking. The probe was transferred to the Center for Magnetic Resonance (CMR) building at LANL were the D-T fill station is located. A fast slewing current driver (amplifier) was built for operating the self-shielded magnetic field gradient coils. It is the field gradient that provides the spatial resolution to the NMR resonance. Experiments with this probe will be conducted in FY96.

1.2.12. CR/UR1 OMEGA-UPGRADE TARGET SYSTEM ENGINEERING

The OMEGA Upgrade Cryogenic Target Delivery System engineering task has as its goal the design, fabrication and installation of equipment that will: fill targets with D_2 or D-T to approximately 1100 atm; condense the gases at temperatures below 30 K; transfer the cold targets to *La Cave* beneath the OMEGA target chamber; carry out layering and diagnostics of the D-T; and insert the cryogenic targets into the LLE target chamber for experiments. The complete system is shown in Fig. 1–5.

To facilitate the engineering design effort the system was divided into several areas: target filling and condensation; target transport; and target insertion (including layering and diagnostics). Significant progress was made in each of these areas.

The fill station hardware was purchased, installed and shakedown tested. Several of the individual components of the system were successfully tested, passing all test specifications:

1. The intensifier, which is capable of compressing fill gases to >1500 atm, achieved pressure control with 5 atm increments and was found to be leak-free at 1500 atm.

2. The cryogenic valves and permeation cell, constructed from beryllium-copper (BeCu) alloy, had leak rates that were an order of magnitude better than specifications.

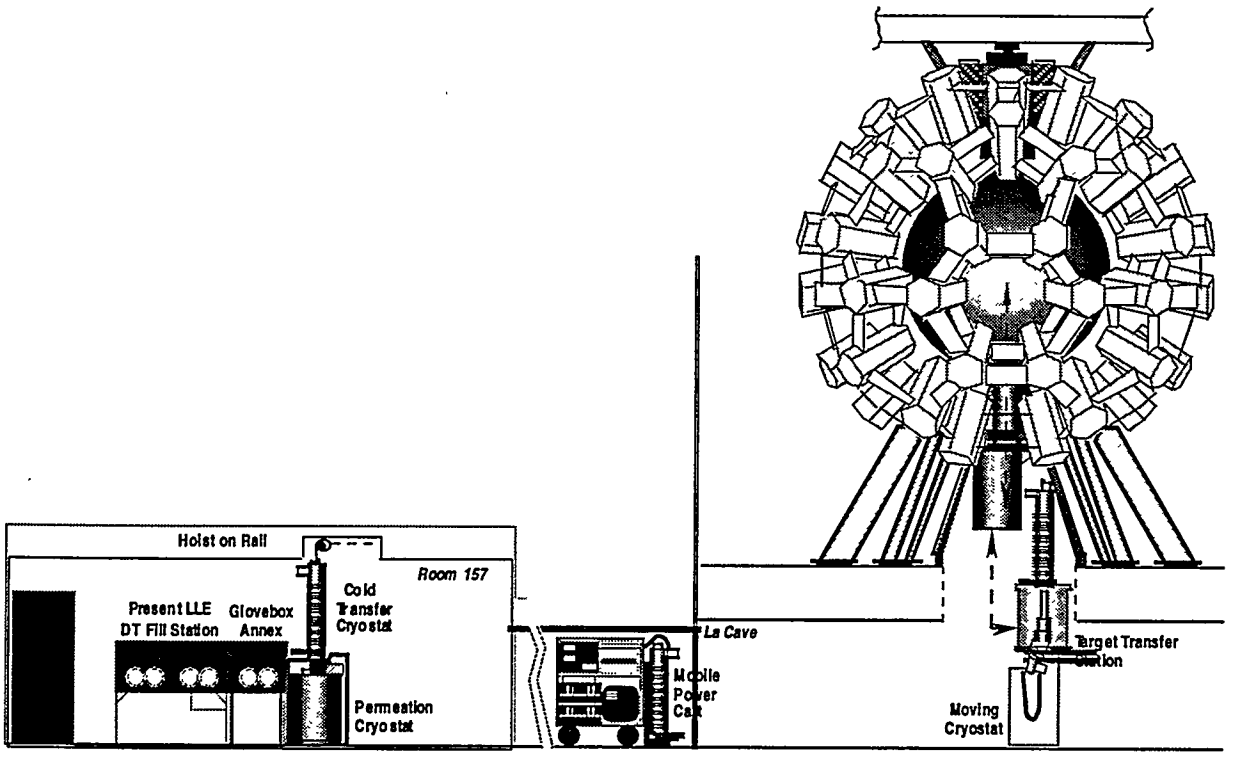

Fig. 1-5. Schematic layout of the OMEGA cryogenic target delivery system.

3. The cryogenic wrench which closes and opens the lid of the permeation cell without transferring any torque to the permeation cryostat was successfully torqued to it's full design capacity of 200 ft-lb.

The permeation cryostat was delivered and tested. The results showed that the specified 20 K was not be achieved. A number of heat leaks were identified which could have prevented the system from reaching the specified 20 K. These leaks have been repaired and the system is again in testing.

The cold transfer cryostat which removes the targets from the permeation cryostat and transfers them to *La Cave* via the mobile power cart was assembled and successfully tested. The system cools to less than 20 K in 8 hr. Target rack positioning into the cell and pick-up from the cell were demonstrated automatically using the computer. The mobile power cart which transfers the cold transfer cryostat with the targets from the fill station to *La Cave* was successfully tested, demonstrating 40 minutes of operation without power from the grid. The cryogenic target positioning system conceptual design was started and is nearing completion. Two concepts are under consideration and a selection will be made after testing of a critical element in one of the design concepts in early FY96. Up to this point we have not identified

any issues that could prevent successful design and installation of a cryogenic target insertion system at LLE. Details on this task are presented in Section 6.

1.2.13. CR/UR2 SHELL CHARACTERIZATION DEVELOPMENT

In FY97, cryogenic ICF targets will require characterization of their inner surfaces. Since these shells will be transparent, we have been investigating optical profiling as a possible technique. The Chapman Instruments MP2000+ profiler was suggested by Mark Wittman. It seems to work well in this application, and next year we will construct a prototype spheremapper.

The objective of this work was to investigate the suitability of this instrument by understanding the effects of the upper surface of a film on measuring the profile of its lower surface (Fig. 1–6). Computer modeling experiments were used to model the phenomena. Comparison of experimental measurements of the same film surface from both above and through the back surface were used to verify the modeling.

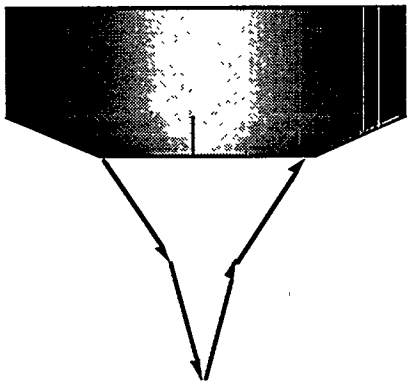

Fig. 1-6. Typical light ray path for optical profiler focused on the back surface of a plastic film.

The roughness of the upper surface can imprint onto the apparent lower surface by the variable refractions it causes in the rays traveling through it. One can see in Fig. 1–6 that the beam has a substantial diameter when passing through the upper surface, so much of this roughness can be averaged out. In fact, computer modeling suggested that the apparent roughness of a perfectly smooth lower surface, caused by the upper surface, is less than 1/10 of the upper surface roughness (Fig. 1–7). This was confirmed by measurements of a GDP film made on a mica substrate. The mica was stripped off and both surfaces of the film

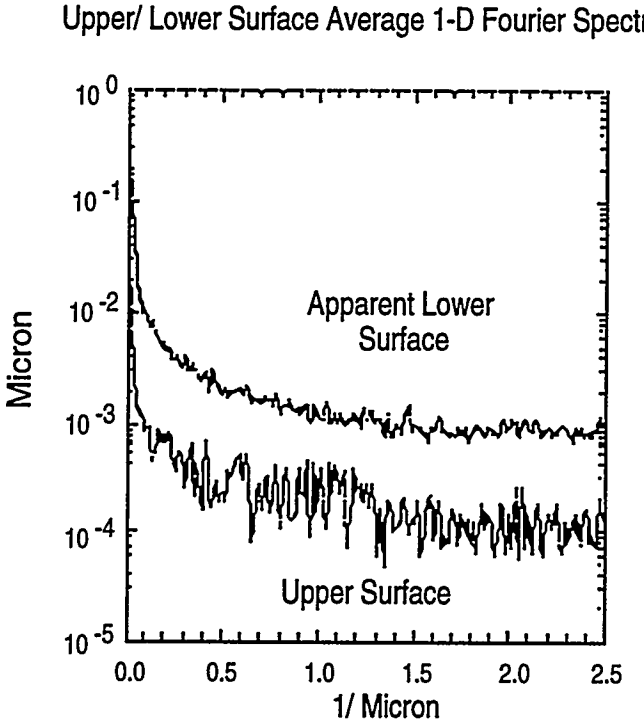

Fig. 1-7. Fourier transform of upper surface profile and apparent lower surface profile. The upper surface is about 10X rougher than the roughness imprinted on the lower surface.

measured from both sides. The roughness of the free surface was typical of our GDP coated shells. The roughness of the mica interface was much smaller (barring some remaining flakes of mica). One could easily measure the true roughness of the smoother surface through the rougher in spite of the order of magnitude difference in roughness (Fig. 1–8).

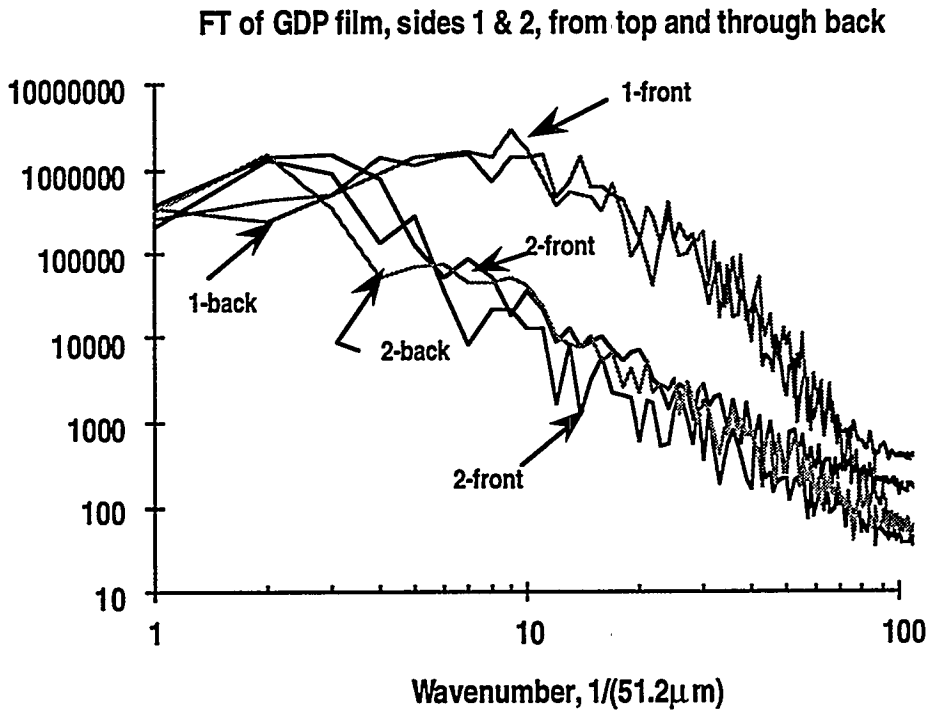

Fig. 1-8. Fourier transform of profiles of the surfaces of a 50 μm thick GDP film on mica.

2. COMPOSITE POLYMER CAPSULE DEVELOPMENT AND PRODUCTION

A major element of the ICF target fabrication activity is development of new techniques for production of improved targets for future deliveries. Some of these activities are described here.

2.1. COATINGS FABRICATION-DOPED GDP COATINGS

In the past year we constructed a new coater in order to explore the possibility of coating ICF target shells with chlorine doped GDP films. The coater was to be used as a development system initially to determine coating parameters that would produce GDP films with as much as six atomic percent (at. %) chlorine. Eventually, the coater would be used as a production coater to supply target quality chlorine doped GDP coated shells. Construction of the coater was completed in late January and the first runs were performed in early February. The development of this system presented two major challenges. First was obtaining coatings that contained some and eventually the desired amount of chlorine. Second, the chlorinated films had to be of good enough quality so that the overcoated shells were target quality.

2.1.1. CHLORINE DOPED GDP COATINGS

Undoped GDP coatings are normally produced by combining trans-2-butene (≈0.1–0.2 sccm) with an excess of hydrogen (10–12 sccm), used as a copolymerizing gas, in the coating chamber. For the chlorinated GDP system a chlorine containing dopant gas was also added (0.1–0.5 sccm) to the system similar to the addition of tetramethylgermanium in the germanium doped GDP coating process. The choice of the dopant was a variable that needed to be determined for obtaining the best coatings that contained the desired amount of chlorine. Initially, flat silicon chips, mica sheets, and glass slides were used as substrates. Later on polystyrene and polymethyl-alpha-styrene shells were coated.

Coating Parameters. It became obvious early on that the presence of hydrogen in the chamber led to coatings that contained virtually no chlorine. Reducing the amount of hydrogen in the chamber produced coatings that did contain chlorine but the films were severely stressed. With all coating parameters unchanged, as the hydrogen flow into the chamber was reduced the coating rate increased. Elimination of hydrogen from the coating process led to extremely high coating rates and tremendous amount of gas phase polymerization. The result was the formation of flakes of GDP in the gas phase in the chamber. These flakes then simply fell on the substrates without adhering to them. This was an undesirable situation for producing target quality shells. In addition, the films formed on the substrates were severely stressed. The stress manifested itself in wrinkling and detachment of the film from the substrate. The films were also very much darker than undoped GDP films. However, it was not apparent originally whether the darker color was a result of the poor coating conditions or a fundamental property of chlorine containing GDP films. Replacing hydrogen with argon in the coating process did not solve the stress problem although it led to coatings that did contain chlorine. In order to reduce the coating rate in the absence of hydrogen the radio frequency (rf) power applied to the gases in the chamber was lowered from the values, 10–12 watts, used in the undoped GDP coating process to 2–4 W. This reduction of the rf power apparently also reduced the coating rate to acceptable levels leading to films that were adherent to the substrate with no gas phase polymerization. The coating rate at the lower rf power was between 0.1 and 1 μm/hr, comparable to undoped GDP coating rates. Depending on the dopant gas used, the films on flat substrates in many cases did contain residual stress, but much lower than in the high rf power runs. The coating on the shells, in general, did not exhibit any stress related features.

Dopants. A number of different chlorinated hydrocarbons were used as the dopant gas (Table 2–1). The maximum amount of chlorine in the coatings resulted when the dopant gas was the only gas in the chamber. Therefore, in order to obtain high amounts of chlorine in the coatings, trans-2-butene was also eliminated from the coating process except when the dopant was chlorine (Cl_2) gas. 2-chloro-2-butene yielded coatings of the best quality. The color of these films was very similar to undoped GDP films. The maximum amount of chlorine in such coatings, however, was only 4.9 at. %, below the desired 6 at. %. With the combination of Cl_2 and trans-2-butene as much as 12.4% chlorine was obtained in the coatings on the shells. However, Cl_2 is very corrosive and difficult to use in the coating system. In addition, the coatings in many cases contained debris on the surface. Better filtering of gas line should eliminate the debris problem.

TABLE 2–1
MAXIMUM AMOUNT OF CHLORINE DOPING (at. %) IN THE GDP COATINGS ON FLAT SUBSTRATES AND SHELLS

Dopant	Flat	Shell	Stress	Opaque
Cl-Styrene	4.3		Yes	Yes
DCE	5.0		Yes	Yes
MeCl	22.0	8.8	No	Yes
Cl-Benzene	7.1	4.4	Yes	Yes
Cl-butene	4.8	4.9	No	No
DiCl-butene	5.0	4.5	Yes	Yes
Chlorine	17.0	12.4	No	No

Note: The quality of the film is measured by its color (opacity) and residual stress on flat substrates. Chlorine was always mixed with trans-2-butene in the coating runs.

Surface finish. Chlorine doped GDP films had smooth surfaces with rms background surface roughness of about 20 nm. This value is higher than the 2–4 nm value for undoped GDP films but is well within the 100 nm rms tolerance. The rms background roughness increased as the coating rate increased and the typical value of 20 nm was obtained at a coating rate of approximately 0.3 μm/hr. The surfaces of the coated shells as examined in the SEM, however, appeared to be sprinkled with small circular features, 0.1–0.5 μm in diameter (Fig. 2–1). The flat substrates did not show the same features. The spots are, in general, too small for EDX elemental analysis but EDX studies on some larger spots did not reveal any difference between a spot and the background. In addition, the occurrence of these features was very inconsistent. They were not always present on the films and in some cases they were present on only a subset of the shells in a given coating run. These features seemed to disappear if the shells were examined 10 days to 2 weeks after coating. Post coating plasma treatment of the coated shells seemed to reduce or eliminate the dots, while washing the shells in water did not. At the moment, the origin of these spots remains somewhat of a mystery.

2.2. CHARACTERIZATION

The following subsections describe the significant improvements achieved in characterization capabilities over the past year.

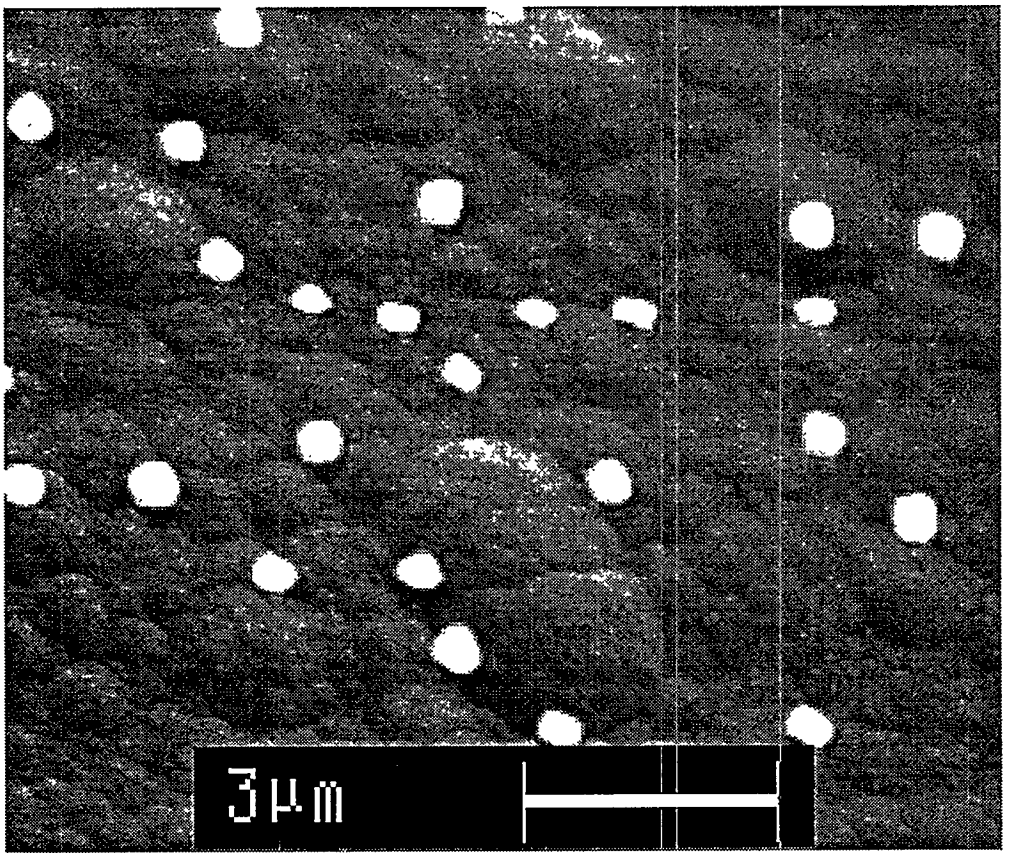

Fig. 2–1. An SEM scan of the surface of a chlorine doped GDP coated polystyrene shell. The background is rather smooth with a typical rms roughness of 20 nm. However, in many cases the surface is sprinkled with features (disks, 0.1–0.5 μm in diameter) that appear brighter than the background in the SEM image.

2.2.1. NIKON INTERFERENCE MICROSCOPE

During FY95 we developed several techniques for improving capsule characterization using our Nikon Optiphot reflectance interference microscope. We fitted this instrument with a 5X Michaelson or a 20X Mirau interferometric objective and a New Focus Z-translation piezo-electric stage having a range of 1 mm and an accuracy of 0.1 μm. Using this reflectance interferometer in the white light mode, we can measure capsule diameter, wall thickness, 4π wall uniformity, layer thicknesses, and the indices of refraction of shell wall materials.

Diameter, Wall and Layer Thickness Measurement. White light interferometric capsule measurement relies on the identification of a specific "reference" fringe that is used to determine the optical path length (OPL) through the material of interest (i.e., the ICF target capsule). We use a black and white TV monitor connected to our microscope to image the

reference fringe (either the blackest fringe or the white fringe between two equally black fringes) reflecting off a given surface. To measure the OPL between two reflective surfaces, we place the sample on the piezo-electric stage under the microscope, and raise or lower the stage from one surface to the other as precisely determined by the reference fringe's appearance on each surface. The optical path length between the two surfaces is simply the physical distance the stage is moved.

To measure a capsule's diameter, we place the capsule on a glass block on the piezo-electric stage (Fig. 2–2). A glass block is used rather than a mirror so that the back-reflected light doesn't wash out the fringes reflecting from capsule surfaces. We then find the stage position where the reference fringe reflects off the top surface of the capsule. Next, the stage is raised until we find the reference fringe reflecting off the glass block upon which the capsule sits. The change in stage height is equal to the capsule diameter.

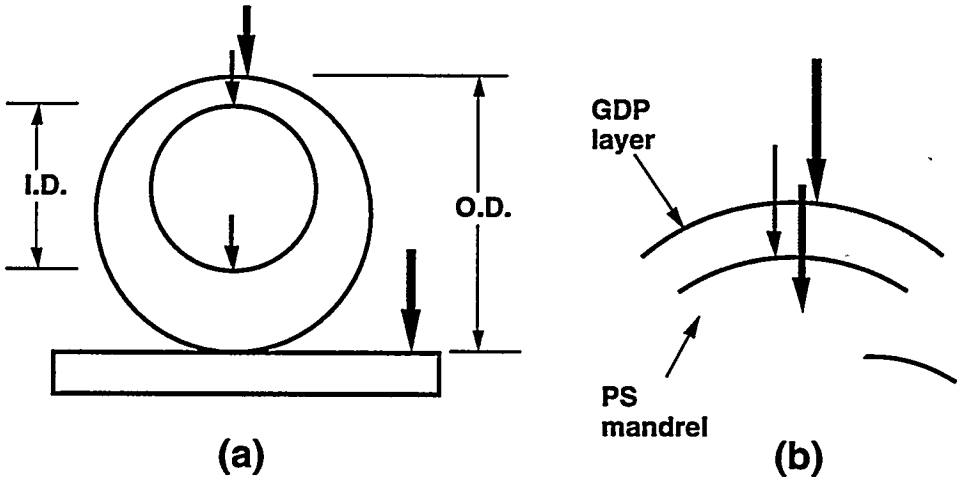

Fig. 2-2. (a) Capsule inner and outer diameters are measured using the reflection off shell and glass block surfaces. b) Layer thickness is measured using the reflection from layer interfaces.

To measure a capsule's average wall thickness we measure both the capsule's outer and inner diameters and use the relationship:

$$\text{Average wall thickness} = \frac{\text{o.d.} - \text{i.d.}}{2}$$

To measure the capsule's inner diameter we find the stage position at which the reference fringe reflects from the inner top surface of the capsule. The stage is then raised until the

fringe reflects from the capsule's inner bottom surface. In this case, the index of refraction of the gas contained by the shell (n_{void}) must be taken into account when calculating the inner diameter from the measured shell void OPL (Δ stage position). This relationship is expressed as:

$$\text{Shell i.d.} = \frac{n_{air}}{n_{void}} \times \Delta \text{ stage position}$$

The wall thickness measurement method described above requires no knowledge of the refractive indices of the shell wall materials. Thus, the average total wall thickness of a capsule having numerous layers can be measured regardless of the number of layers or their compositional uniformity.

Capsule layer thicknesses can also be determined using white light reflectance interferometry. This is done by using the most intense fringe reflecting from layer interfaces. We have found that interface fringes are discernible as long as the two adjacent layers have indices of refraction that differ by more than two percent.

To illustrate layer thickness measurement, consider the case of a GDP layer on a CH shell. We again use the reference fringe as a marker to find the OPL (Δ stage position) from the outer GDP surface to the GDP/polystyrene interface. Dividing this measured optical path length by the index of refraction of GDP gives the physical thickness of the GDP layer.

Index of Refraction Measurement. The index of refraction of a material (for a given wavelength) is defined as the optical path length through that material divided by its physical thickness. We can measure the physical thickness of a sample as described above using our Nikon reflectance interferometer. We adjust the piezo-electric stage until the reference fringe is visible on top of the sample then raise the stage until the fringe is visible on the surface upon which the sample is resting. In similar fashion, the optical path length through the sample is measured from the stage position at which the reference fringe is visible on top of the sample to the position at which the fringe is visible through the sample. The ratio of these two optical path lengths gives the index of refraction of the material under white light illumination using our optical system.

4π Non-Concentricity Measurement. We have developed and now regular use a technique that can measure the 4π non-concentricity (NC) of a capsule from a single view. This method is applicable to capsules possessing only a P1 type defect, wherein the shell's

outer surface and inner void are both perfectly spherical and have centers offset from one another by the distance ε. For this case, shell NC is defined as:

$$\text{NC } \% = \frac{\varepsilon}{\text{Average wall thickness}}$$

The standard method of measuring 4π capsule NC requires that the capsule be oriented such that the P1 defect lies on the X-Y plane normal to the viewing Z-axis. In this orientation, the interferometric bull's-eye is most displaced from the center of the shell. To make this measurement, the capsule is held by a vacuum chuck (or other suitable holder) and rotated under the interference microscope until the correct orientation is achieved. The operator must judge when the interferometric bull's-eye is most displaced from the center of the shell and then measure its offset. A ray tracing program is used which provides for the conversion of the offset measurement to non-concentricity.

Our method is much simpler and is more precise for thick walled (>20 μm) composite capsule measurement. In our method, the capsule is placed on a glass block. First, the X-Y axis NC of the capsule is found using the standard technique of measuring the offset of the interferometric bull's-eye. Here, the Newton's ring, marking the capsule/glass block contact point, determines the center of the shell and simplifies that task for the operator.

Second, the Z-axis NC is found by measuring the average two wall thickness and the bottom wall. The average two wall thickness is found by measuring the difference of the optical path length of the light passing through the shell and reflecting off the glass block (Point B in Fig. 2–3) compared to the adjacent air path reflecting off the glass block (Point C). The bottom wall thickness is found by measuring the optical path length from the capsule's inner bottom wall surface (Point A) to the outer surface (Point B) than dividing this length by the index of refraction of the wall.

The Z-axis NC can then be calculated from the relationship:

$$\text{NC}_Z = \text{Absolute}\left(1 - \frac{\text{Bottom Wall}}{\text{Average Wall}}\right)$$

Finally, capsule 4π NC is calculated by vectorally combining the X-Y and Z axes measurements:

$$4\pi\,\text{NC} = \sqrt{\text{NC}_{XY}^2 + \text{NC}_Z^2}$$

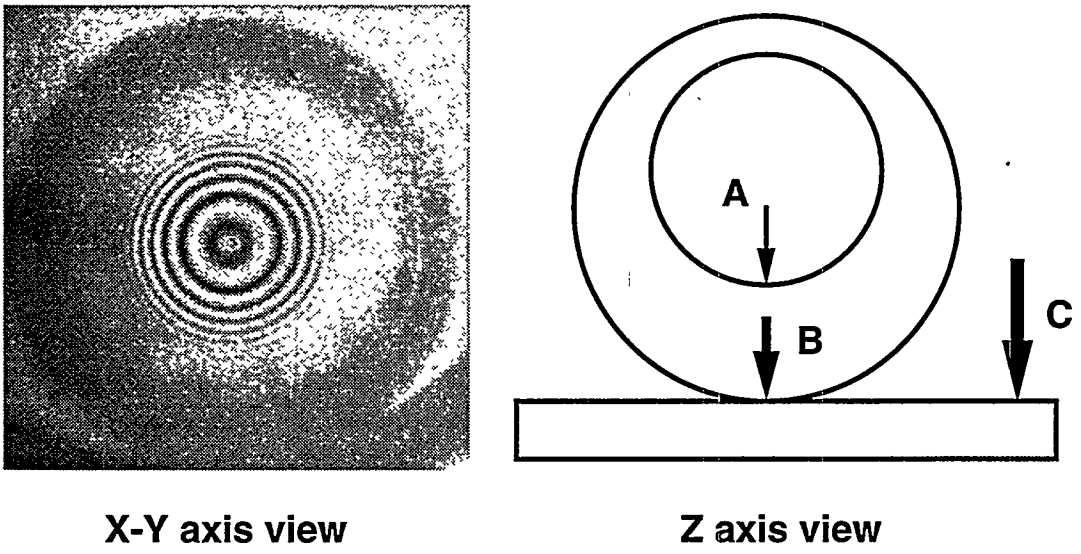

Fig. 2–3. 4π non-concentricity capsule measurement has been greatly simplified.

For further information, please contact D. Steinman (GA)

2.2.2. ATOMIC FORCE MICROSCOPE

We constructed an Atomic Force Microscope (AFM) Spheremapper to assist process development and for deliverable characterization using the LLNL AFM Spheremapper as a prototype. We modified the LLNL design to accommodate our limited space and to optimize stability of the AFM platform.

Because of the limited space, we built the whole instrument into one counter (Fig. 2–4). The AFM head must be separately supported on a vibration isolation table to reduce measurement noise, so a 2 ft × 4 ft optical table was mounted on sufficiently short legs to hide it under the counter (Fig. 2–5). The steel casting for the air bearing supports a breadboard which in turn supports the AFM head. Only this breadboard is exposed through the counter top, so the table is substantially isolated from surrounding disturbances. To further minimize vibrations, ancillary equipment was mounted on the counter, rather than the isolated table, whenever possible. The viewing cameras and interface electronics are mounted on a Unistrut frame which is supported on the counter. Because the cameras are not mounted on the isolated breadboard, one often sees substantial motion in the shell images; that indicates vibration in the camera mount rather than the shell.

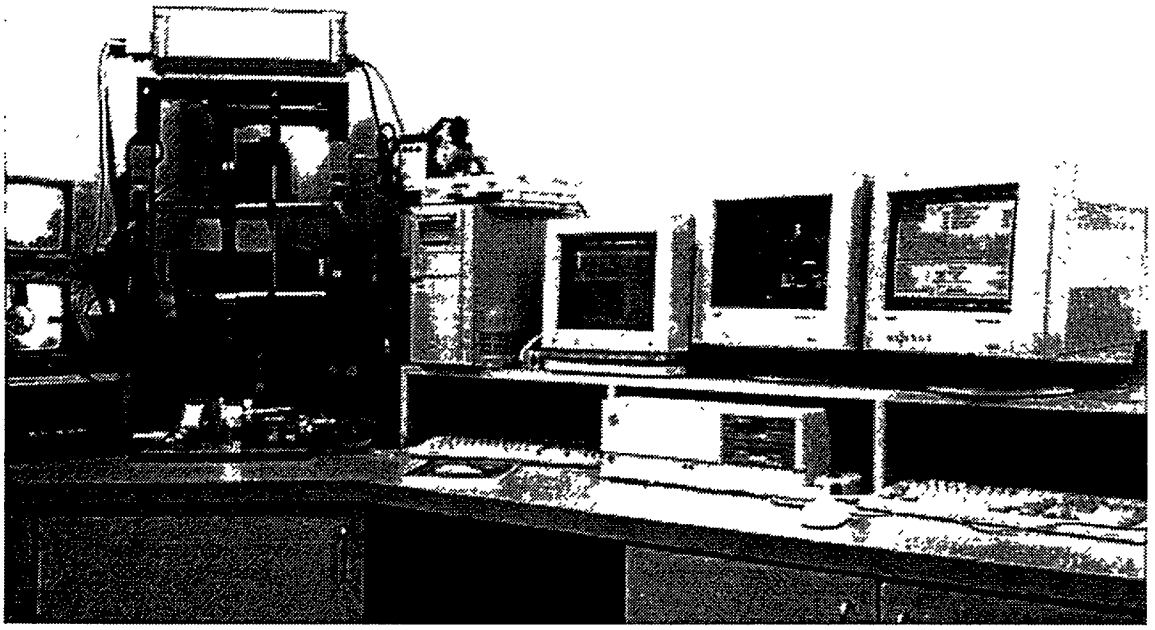

Fig. 2–4. GA AFM Spheremapper. The Unistrut frame on the left supports interface electronics and sample viewing cameras. The spheremapper is under the front of that frame, with the vibration isolation support table hidden under but separate from the counter.

The area around the AFM head was somewhat isolated from air currents with a plastic cylinder which extended out over the air-bearing (Fig. 2–6). Holes were drilled at the top and back to provide a clear view for the cameras, and a white patch was painted on opposite sides to provide appropriate back-lighting.

The electronics and computer hardware and software were only minimally modified. A Stanford Research active filter replaced the LLNL built "Alias Assasin", and the shaft encoder interface box was modified so that the motor control and piezo Z signal went into it; that reduced connections to the interface board to a single ribbon cable.

Finally, the Digital Instruments AFM was modified to provide larger dynamic Z range. It was feasible to extend the range to ~7 μm (compared to ~4 μm for the standard model) using a longer length of their standard hardness piezoelectric material if we gave up about half of the range for X-Y scans. Using softer piezo material would allow a longer Z range without sacrifice of X-Y range, but at a cost of substantially larger non-linearities and possible drift.

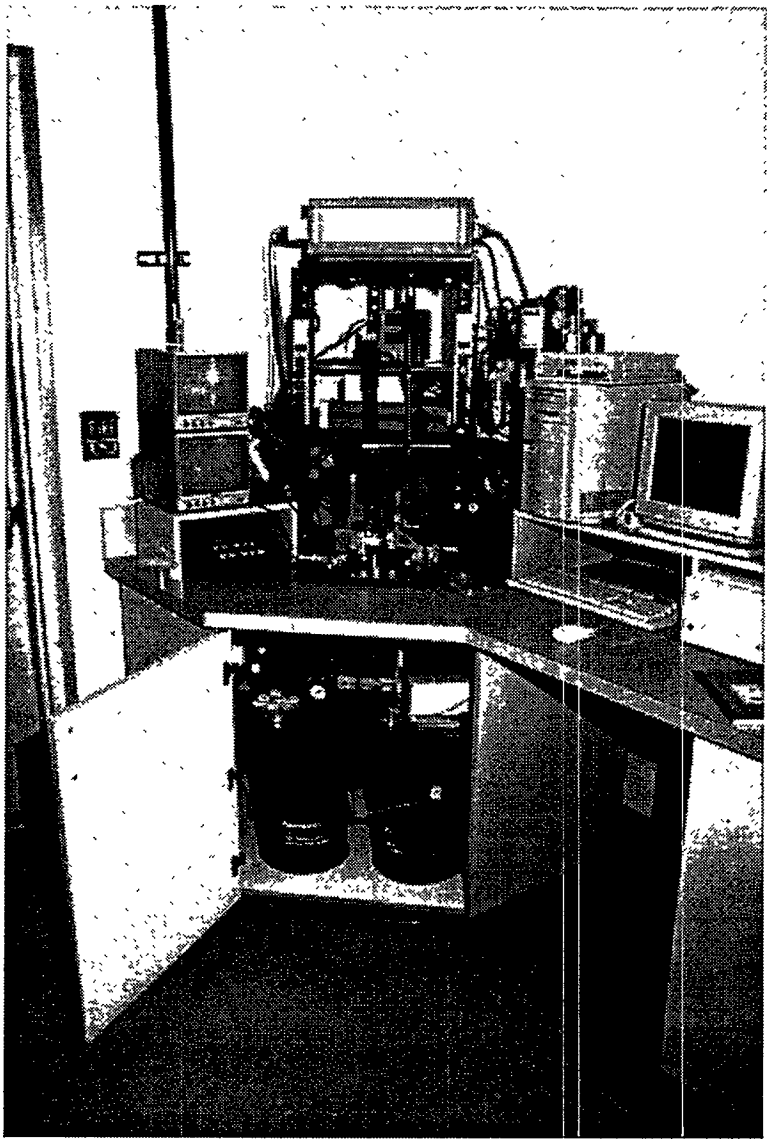

Fig. 2–5. The table under the counter is mounted on short vibration isolation legs. A steel casting on the table supports an air-bearing and the breadboard which shows through the counter. The breadboard, holding the AFM head, is completely isolated from the counter and Unistrut frame surrounding it.

The electronics and computer hardware and software were only minimally modified. A Stanford Research active filter replaced the LLNL built "Alias Assasin," and the shaft encoder interface box was modified so that the motor control and piezo Z signal went into it; that reduced connections to the interface board to a single ribbon cable.

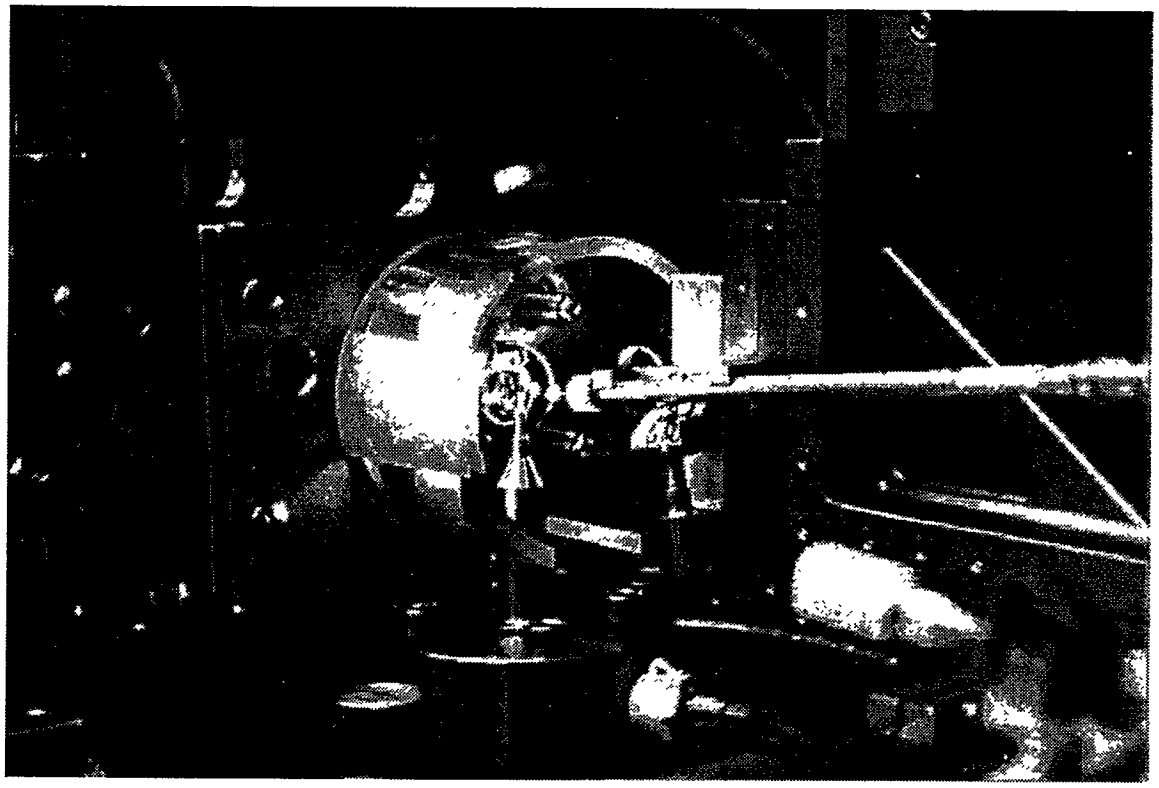

Fig. 2–6. The AFM head is surrounded by a plastic draft shield which extends over the air-bearing and shell. The shell is inserted from the opposite side. Holes are cut in the draft shield to give a clear camera view, and a white patch on the shield provides diffuse back-lighting.

Finally, the Digital Instruments AFM was modified to provide a larger dynamic Z range. It was feasible to extend the range to ~7 μm (compared to ~4 μm for the standard model) using a longer length of their standard hardness piezoelectric material if we gave up about half of the range for X-Y scans. Using softer piezo material would allow a longer Z range without sacrifice of X-Y range, but at a cost of substantially larger non-linearities and possible drift.

For further information, please contact R. Stephens (GA).

2.2.3. DETERMINING MASS OF CAPSULES

There is a need to accurately characterize shells by their mass per unit area, σ. Previously that had been done by combining specific gravity, average shell wall thickness, and average outside diameter. Uncertainties in measurements of wall thickness cause σ uncertainties larger than 5% because of the need to average the wall thickness over the whole shell image.

Higher resolution cameras exist, and their use would have improved the accuracy of σ proportional to their pixel count, but that would have required expensive upgrades and slowed the characterization rate.

Instead, we have set up the capability to weigh the shells to ~0.1%. Combining that with diameters accurate to ~0.2% give σ uncertainty under 0.5%. A typical shell weighs 100 μg, so a weighing precision of ~0.1μg is required.

We obtained a Cahn C-34 microbalance whose precision and accuracy is stated as ±0.1 μg. Setting the balance in a temperature controlled room with minimal air circulation, and with appropriate measuring care, we find a measurement repeatability between 0.1 and 0.2 μg for a set of 10 shells. There are no weight standards in this range—the μbalance is calibrated with a 200 mg weight — thus we assume the reproducibility reflects the accuracy.

For further information, please contact R. Stephens (GA).

2.3. DIAGNOSTIC GAS PERMEATION

Precision filling of composite capsules with diagnostic gases via post coating permeation was begun in FY94. This year we have made improvements in our permeation filling capabilities and have developed a method to predict hydrogen retention properties of individual capsules by measurement of its respective Ar retention properties.

2.3.1. IMPROVEMENTS IN PERMEATION FILLING

A new dedicated permeation station was designed and built. This new station is more friendly and reliable than the previous station attached to our XRF system. The new design also allows for precise permeation filling of capsules with gas mixtures, starting from nominally pure single dopant gases, with fill pressures up to 20 atm. This capability allows for reduced cost and faster turn-around time for capsule deliveries. The design of the new permeation station is shown in Fig. 2–7.

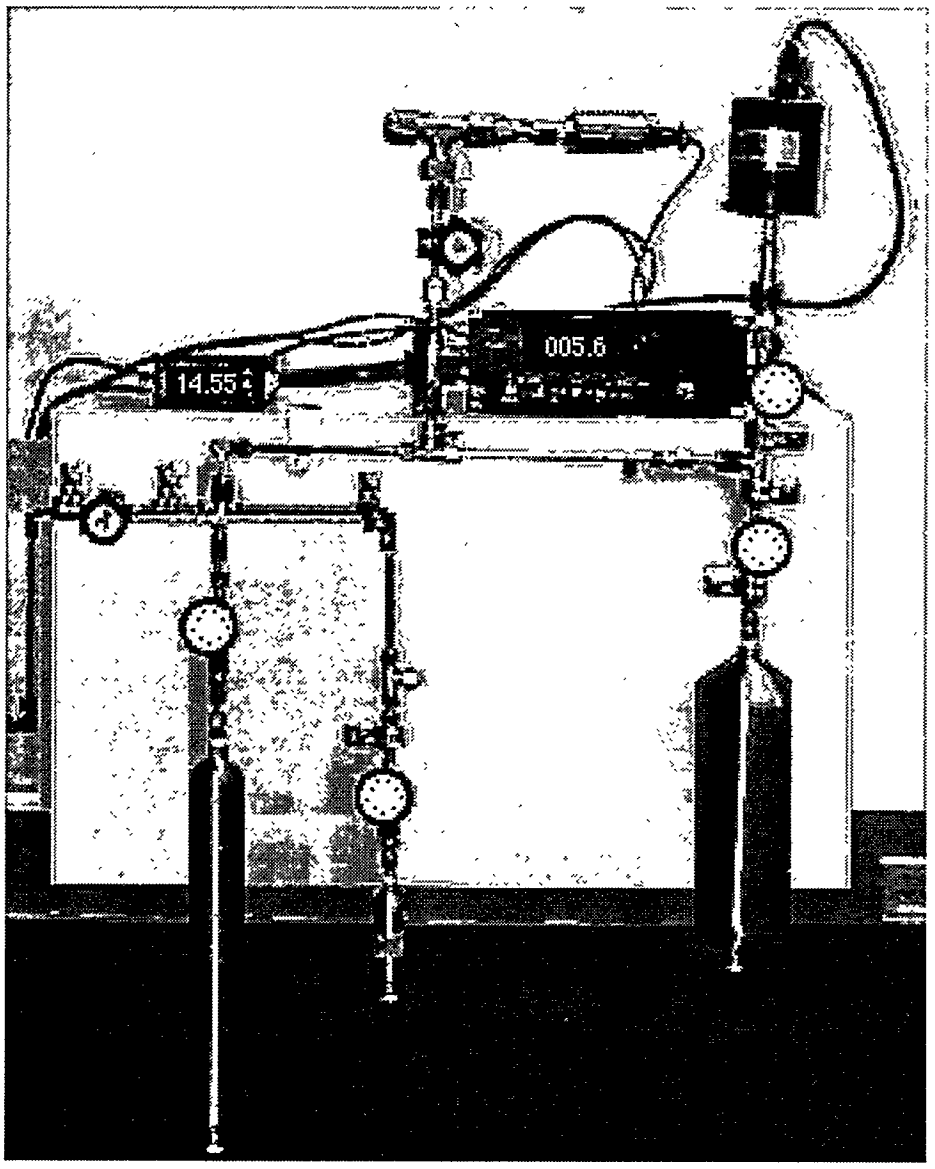

Fig. 2-7. New permeation filling station allows for precise filling of capsules with either a single dopant gas or gas mixtures starting from nominally single dopant gases.

2.3.2. PREDICTION OF A CAPSULE'S HALF-LIFE

Prediction of a capsule's hydrogen (including isotopes) retention capabilities is reliably determined by measuring its respective argon permeation half-life (the time required for half of a capsules initial gas fill to leak out of the capsule) via XRF. A selection of GDP/PVA composite capsules were permeation filled at 113°C for 20 hrs. Each capsule's Ar half-life was determined by using the XRF system to measure the Ar content of each shell. These

capsules were then filled to 50 atm with deuterium (D_2) in a specially designed fill-crate which allows optical measurement without removal of the capsule from the crate (Fig. 2–8).

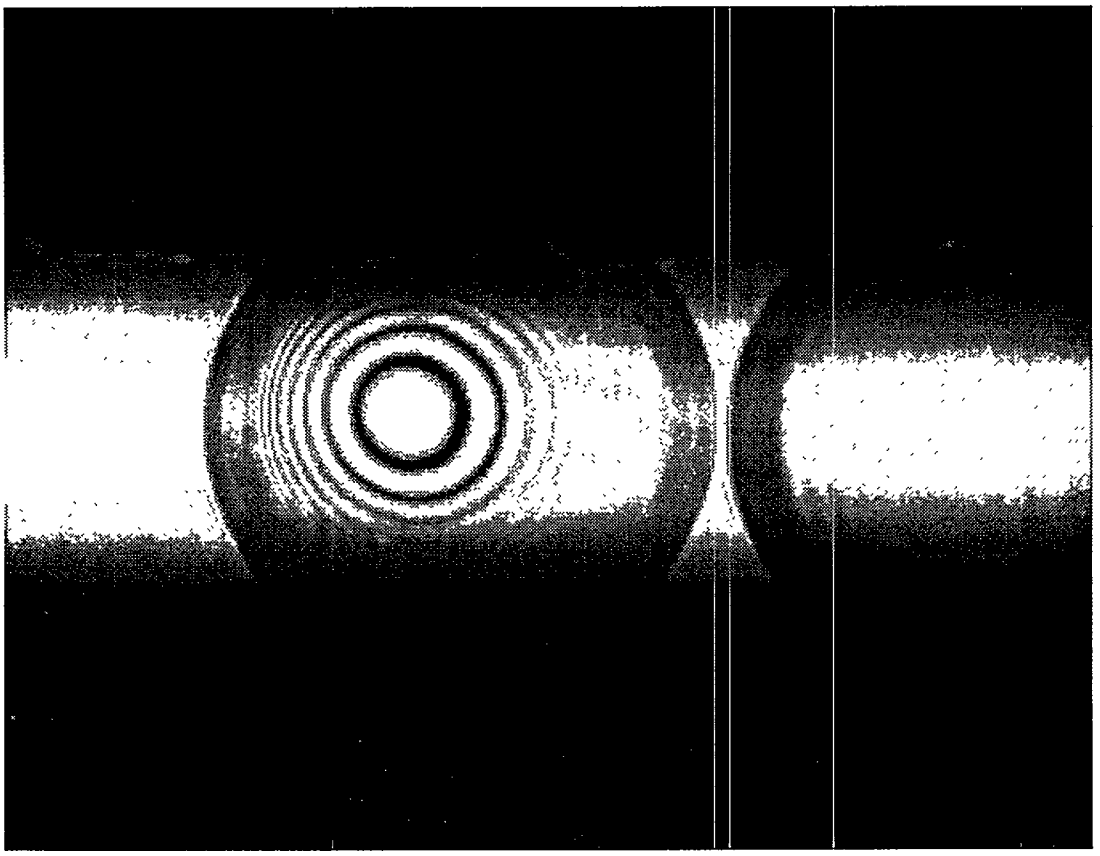

Fig. 2–8. Fill-crate allows optical measurement of capsules without removal of the capsules from the crate.

Plotting of capsule Ar half-life against measured D_2 half-life yields a graph with a very high correlation coefficient (Fig. 2–9).

The high correlation between the measured Ar half-life and the corresponding deuterium half-life allows future capsule deuterium half-lives to be measured by Ar XRF alone with a high degree of confidence. This technique reduces the handling required for each capsule and shortens the time necessary to perform the half-life characterization.

For further information, please contact M. Hoppe (GA).

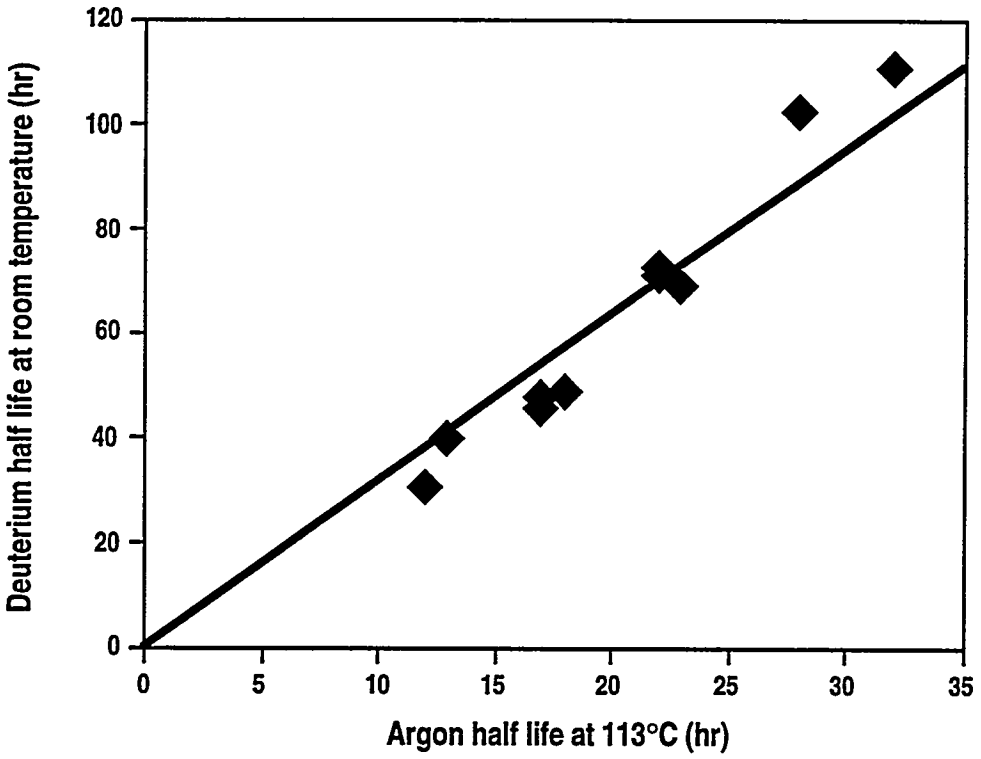

Fig. 2-9. Graph of Ar half-life vs. D_2 half-life indicates that the D_2 half-life is reliably predicted by measurement of the Ar half-life alone.

2.4. BURST TESTING OF POLYMER AND GLASS SHELLS

We conducted helium burst test experiments on polymer shells to learn what gas fill pressures these shells could hold. The polymer shells consisted of spare batches (not necessarily target quality) of microencapsulated polystyrene shell mandrels made by the target fabrication group at LLE/UR. The shells had ~800 μm diameters and ~8 μm walls. We overcoated them with GDP to bring their total wall thicknesses up to the desired 10 to 40 μm total wall thickness ranges. These shells were filled and burst tested with helium at room temperature typically using four atmosphere steps with 10 minute intervals. Preliminary burst test results for the polymer shells are shown in Fig. 2–10.

These burst test results are considered to be strictly "preliminary" due to the limited supply of "target quality" shells that were available at the time of testing. Future burst tests will use these results as a starting point to more precisely determine the burst strength of target quality composite capsules to be used at UR/LLE for experiments on OMEGA Upgrade.

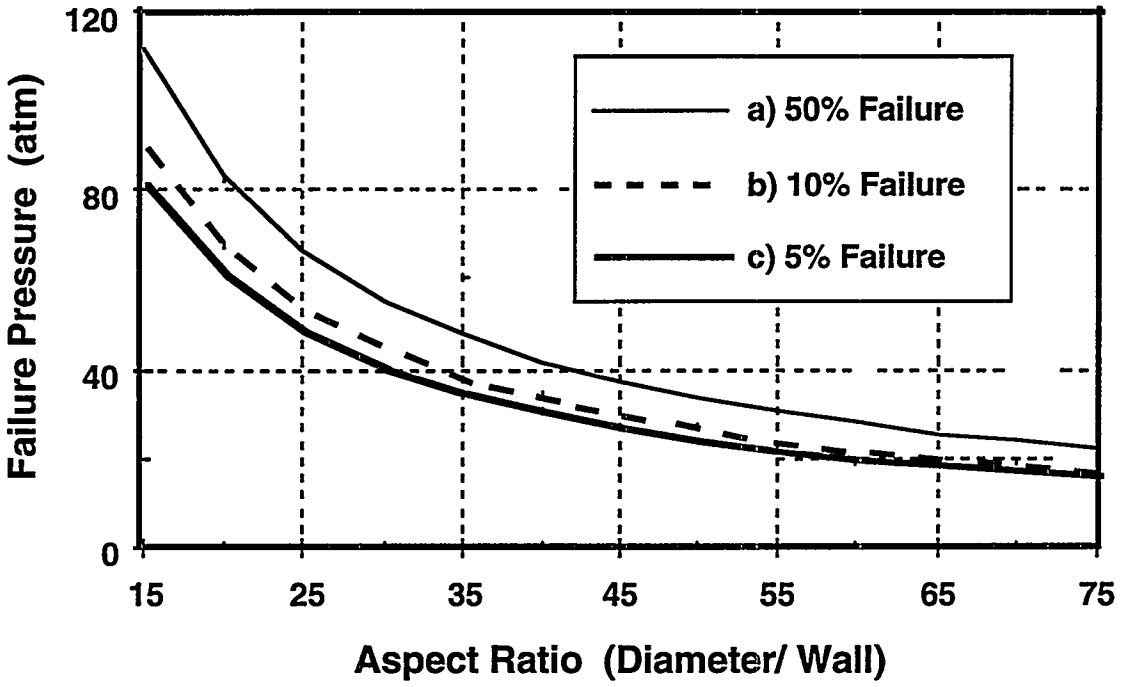

Fig. 2–10. Preliminary burst test results of composite polymer capsules.

We also burst tested glass shells for the purpose of culling out those shells too weak to hold twenty atmospheres of D-T. The glass shells we tested were made in our high temperature drop tower and were typically 1200 μm in diameter with ~3 μm walls. These shells were initially buckle tested to three atmospheres in large batches then filled in two atmosphere steps with six minute intervals in helium at 350°C. The final pressure achieved was 48 atmosphere prior to an instantaneous vent to atmospheric pressure. The surviving shells were fully characterized, sent to Mound Lab for D-T filling, then shot at both LLNL and UR/LLE, producing record neutron shots.

For further information, please contact D. Steinman (GA).

3. MICROMACHINED TARGET COMPONENTS

An important part of our target fabrication activities involves micromachining of hohlraum mandrels and other indirect drive target components.

3.1. PRECITECH LATHE SURFACE FINISHES

While our Precitech lathes have proved to be capable of controlling the dimensions of parts to very tight tolerances, they do not produce as fine surface finishes as the latest model Precitech lathes or the Rocky Flats' No. 3 lathe. A series of tests that demonstrate this are described in this section.

In this study, the surface finishes produced in a series of facing cuts on copper discs were analyzed by atomic force microscopy. The surfaces were also studied using optical microscopy. The facing cuts were all made with a cut depth of 0.002 mm at a spindle speed of 600 rpm on a previously machined surface. The same diamond tool with a radius of 0.025 mm was used in every case while the tool feed rate was varied from 4 mm/min. to 0.08 mm/min.

The appearances of surfaces cut at various feed rates are shown in Figs. 3–1 to 3–4. The grooves produced by the tool are readily apparent and decrease in size as the feed rate decreases. However, for feed rates below about 1 mm/min there is little change in the appearance of the surface. This observation is supported by surface roughness measurements made in the atomic force microscope, an example of which is shown in Fig. 3–5. The data are compared with the theoretically expected peak-to-valley distance. Below, a feed per revolution value about 20 μm there is no improvement in surface finish.

GA has two Precitech lathes, a first-generation unit purchased by DOE, and a second-generation unit purchased by GA. The latest, third-generation, or "modern" Precitech lathes produce much better surface finishes than our lathes. The appearances of surfaces produced by one of these lathes are shown in Figs. 3–6 to 3–9. As the feed rate decreases, the groove size decreases until at the lowest feed rate, grooves are no longer observable. The roughness of this latter surface was about 50 Å rms which is well below the best surface produced by our lathes (250 Å rms).

Based on this study, we decided to return the DOE-owned Precitech lathe to the factory for upgrading to bring it up to the capability of the latest model Precitech lathes.

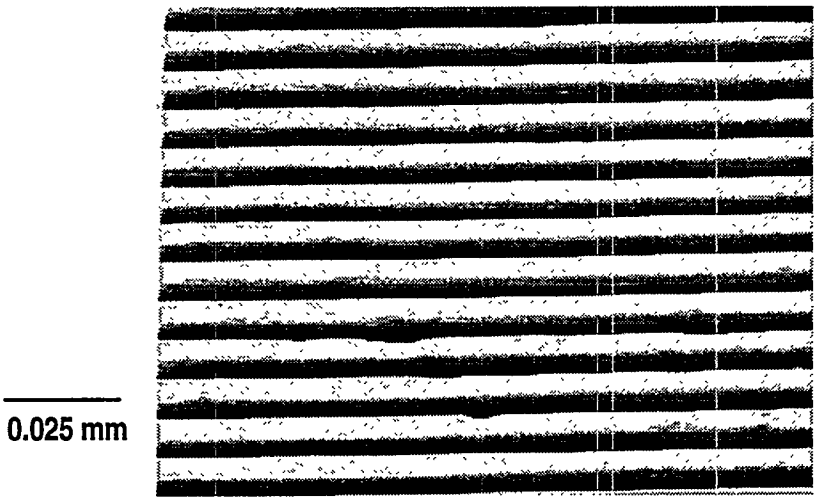

Fig. 3–1. No. 1 Precitech 600 rpm 0.025 μm radius tool, 4 mm/min tool feedrate.

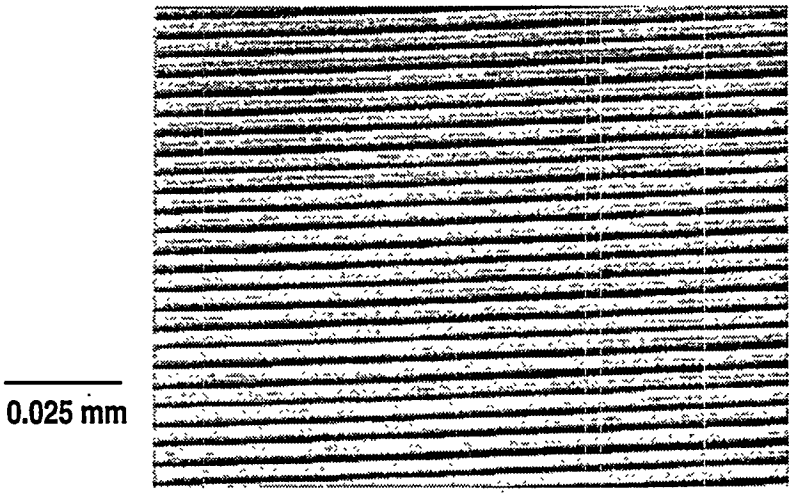

Fig. 3–2. No. 1 Precitech 600 rpm 0.025 μm radius tool, 2 mm/min tool feedrate.

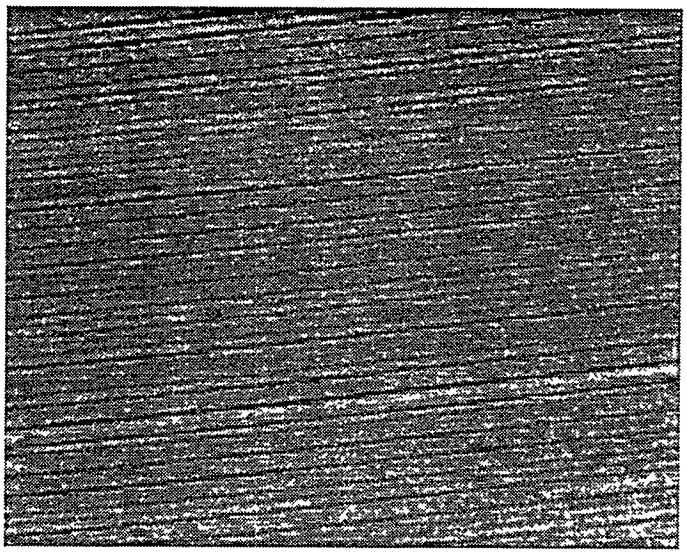

Fig. 3–3. No. 1 Precitech 600 rpm 0.025 μm radius tool, 1 mm/min tool feedrate.

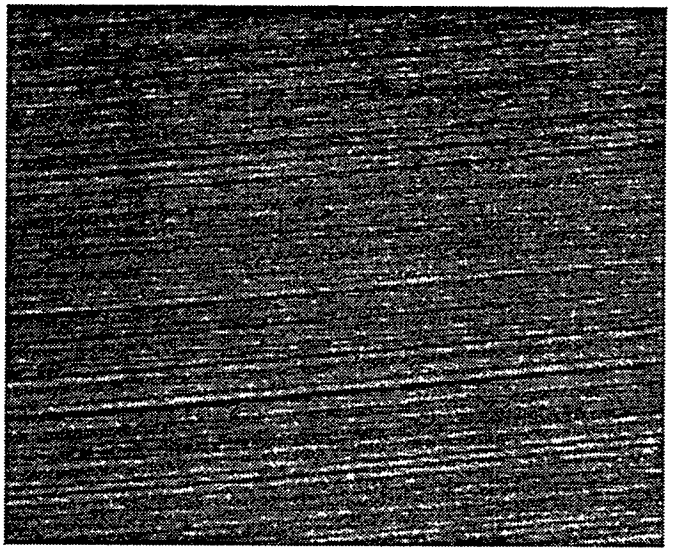

Fig. 3–4. No. 1 Precitech 600 rpm 0.025 μm radius tool, 0.08 mm/min tool feedrate.

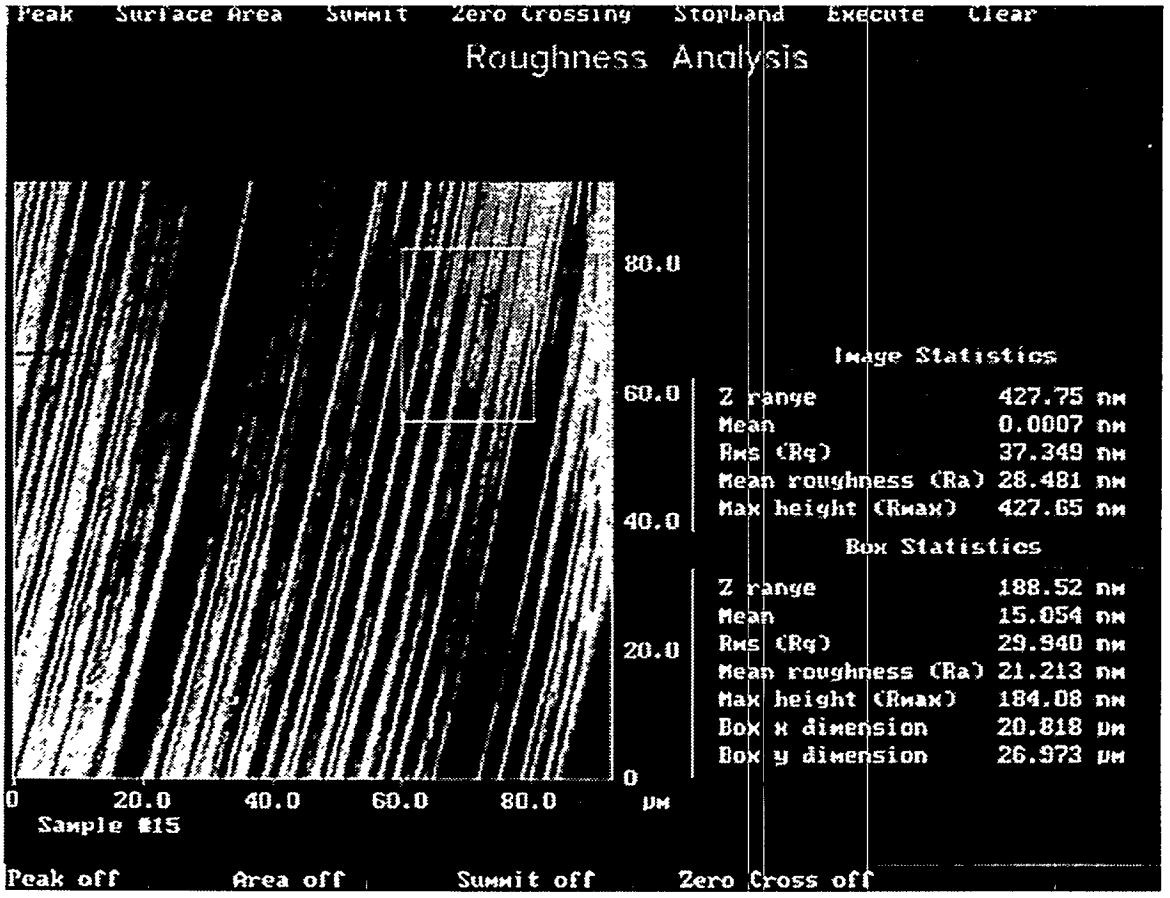

Fig. 3–5. Surface roughness measurements made in the atomic force microscope

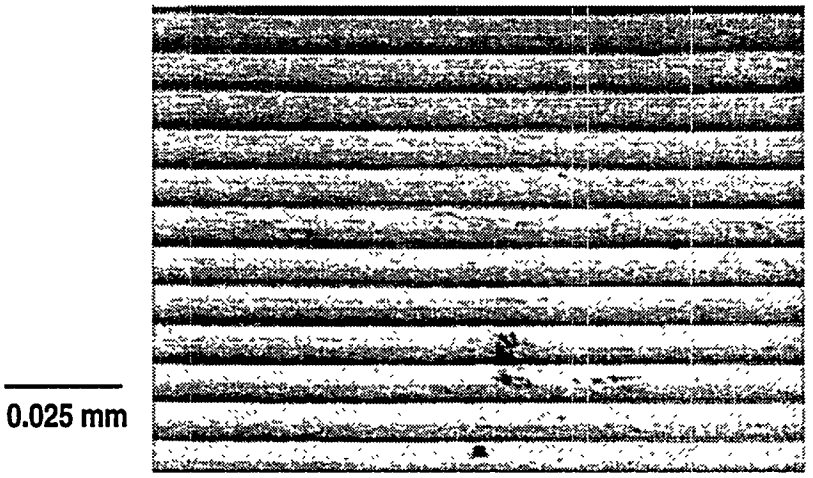

Fig. 3–6. Modern Precitech 600 rpm 0.025 μm radius tool, 4 mm/min tool feedrate.

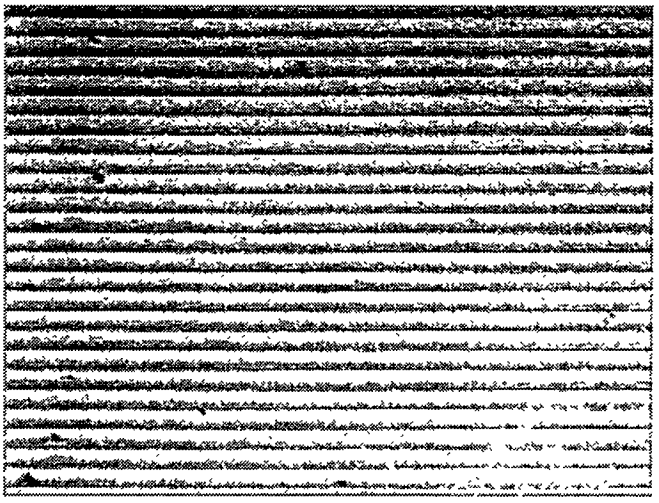

Fig. 3–7. Modern Precitech 600 rpm 0.025 µm radius tool, 2 mm/min tool feedrate.

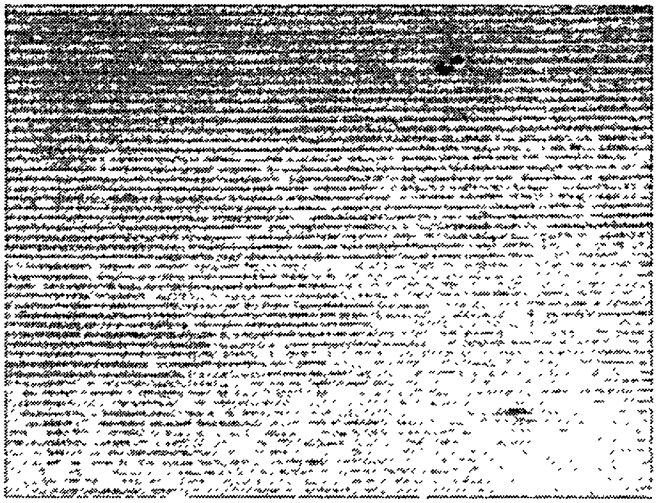

Fig. 3–8. Modern Precitech 600 rpm 0.025 µm radius tool, 1 mm/min tool feedrate.

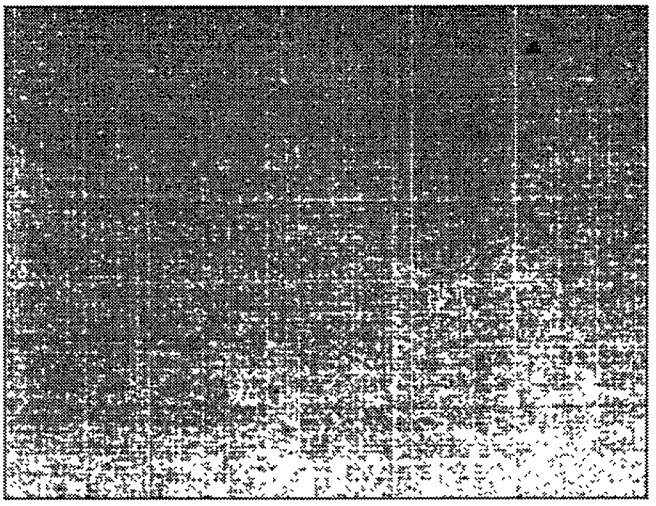

Fig. 3–9. Modern Precitech 600 rpm 0.025 μm radius tool, 0.08 mm/min tool feedrate.

4. OTHER TARGET DEVELOPMENT

In addition to development of improved capsules and hohlraums described in Sections 2 and 3, we also pursued development of a wide variety of targets for the various elements of the national ICF program.

4.1. NIKE TARGET DEVELOPMENT

The NIKE target development task is divided into two subtasks: (a) target production and (b) characterization development. The NIKE laser has become fully operational during this fiscal year and, therefore, a continuous flow of targets has been required for the NIKE experimental program.

4.1.1. TARGET PRODUCTION

The targets for the NIKE laser are flat hydrocarbon polymer foils with surface morphology, foil curvature, geometrical dimensions, and chemical composition which meet the specifications set forth in detail by the NIKE project team at NRL. Some of the targets are single foils whose thicknesses are between 10 and 100 micrometers. Other targets consist of two foils, parallel to each other and spaced apart from 50 to 400 micrometers with one foil (the "second foil") 10-15 micrometers thick and the other foil (the "first foil") 50100 micrometers thick. Still other targets are required to have sine wave or other patterns of various spatial wavelengths on the foil surfaces.

Because of the requirements imposed on the target characteristics by the experiments being planned and executed using the NIKE laser, the targets must have their detailed properties measured (characterized) and provided to the NIKE team together with the targets.

NRL Target Specifications. The basic specifications for the NRL NIKE targets are as follows:

1. Planar foils whose surfaces, in the spatial wavelength range 2 mm < 1 < 200 μm, have peak to valley roughness less than 100 Å.

2. Planar foils whose curvature is less than 1 μm/mm.

3. The foils are to be of CH polymer with a clear area of at least 2 mm x 2 mm with thickness in the range 10–100 μm.

4. Both single and double foil targets are required. In the case of the double foil targets, the two foils are to parallel to each other to within 0.2% with foil-to-foil spacings of 50–400 μm.

5. The second foils normally have thicknesses between 10 μm and 15 μm and may be specified as CH or pure carbon film depending on the specific target request.

NRL has also requested target foils with both rippled and randomly rough surfaces. The rippled surface target foils are to have sine wave functions impressed on the surfaces in only one direction for some targets and in both the "x" and "y" directions for other targets.

Target Mounts. A drawing of the frames on which the target foils are mounted is shown in Fig. 4–1. The frame material is a polycarbonate polymer. The frames are acquired from outside machine shop vendors and have the foil mounting surfaces re-machined in-house to provide surfaces which are co-planar to a few micrometers.

Because of the inherent flexibility of the material of the mounts, it has not been possible for us to clamp the mounts to the table of a milling machine and re-cut the critical surfaces in the normal manner. To prevent residual stresses from distorting the mounts after machining, they are annealed before they are machined, and the machining process is accomplished with the mounts "potted" in a relatively massive metal trough or box. Thus, the final smoothing cut on the critical surfaces is done with the mounts held in a rigid configuration in which no flexing of the mount is permitted. The potting compound is a water soluble material, which has a melting temperature of about 80°C. The potting material is melted in the holding trough, the mounts are inserted, and the assembly is cooled to room temperature. The machining is accomplished and the potting material is melted, poured out, and the remaining material on the mounts is washed away in hot water. This procedure results in target frames on which target foils can be mounted and the foil parameters maintained within the specifications requested by NRL.

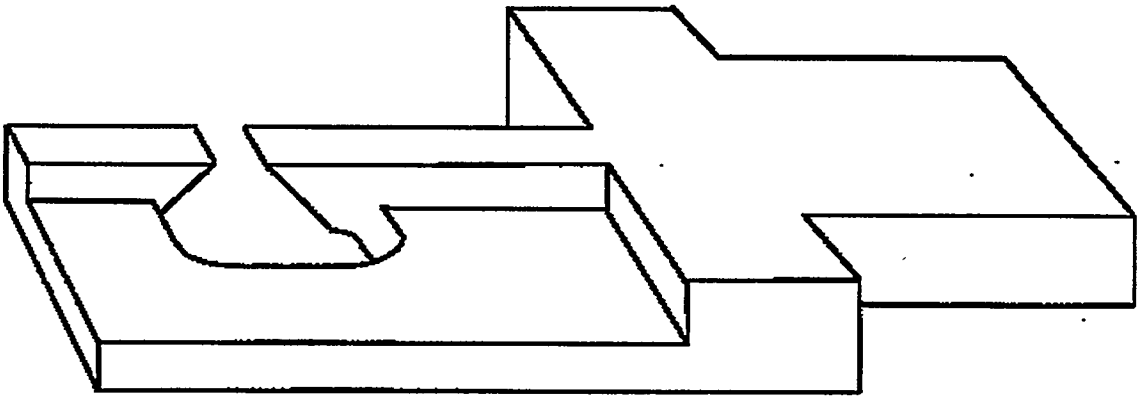

Fig. 4-1. NIKE target mount

Target Film Production. The films from which the target foils are cut are prepared by dissolving polystyrene in toluene and depositing an appropriate quantity of the solution on the surfaces of silicon wafers from which the solvent is allowed to evaporate. The films of polystyrene remaining on the wafer surfaces are dried for several hours and then baked in an oven for 50 hours at a temperature of 100°C. The long heating process completes the removal of any remaining solvent and relieves residual stresses in the film so that strips cut from the film for target foils will remain flat. The thickness of the deposited films is determined by the concentration of the polystyrene in the solution and the volume of the solution deposited on the surface of the silicon wafers.

The thickness profiles and surface morphology of the annealed polystyrene films are determined and recorded together with the film "serial number." The films can be stored on the wafers for later use or can be cut into large sections or targets foils (6 mm x 2.5 mm) for immediate use or for storage.

Target Assembly. In addition to the target mounting frame and the target foils cut from the cast films, cements compatible with the polymers in the films and mounts are necessary to attach the foils to the mounts. For assembling double foil targets, we also require material for spacers to provide accurate separation of the two foils. Figure 4–2 is a schematic diagram of a double foil target showing only the central section of the target frame. The spacers which are currently used in the double foil targets include sections cut from polystyrene films and sections cut from glass, microscope slide, cover slips. The #1 cover slips are 160 μm to 175 μm thick. To obtain larger spacings between the foils than the thickness of the cover slips, more than one section of glass slip are used or sections of cast films are stacked with

cover slip sections. The two most difficult aspects of the assembly procedure are maintaining the foil curvature to be less than 1 μm/mm and keeping the two foils parallel to better than 0.5%. Initially, it was a great achievement for the assemblers to meet both of the difficult target specifications at the rate of a few targets per week. However, as the skills of our talented target assemblers have developed, they can assemble several double foil targets per day which are well within the specifications.

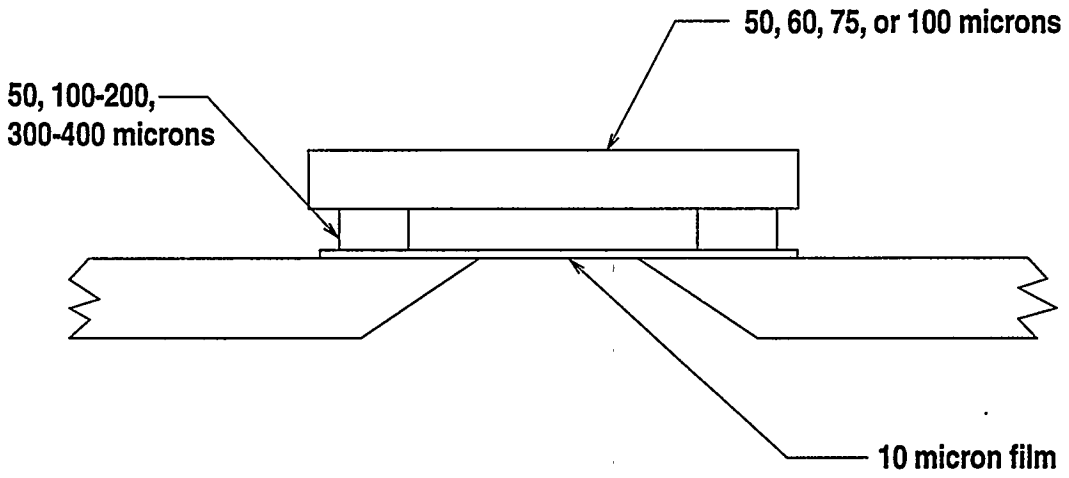

Fig. 4-2. Schematic diagram of a double foil target

4.1.2. TARGET CHARACTERIZATION DEVELOPMENT

One of the most important characteristics of the NIKE laser targets is the surface morphology of the foils. If it is assumed that the material of the foil has a uniform point-to-point density, variations in the thickness of the foil are indicative of variations in the mass per unit area of the foil. This parameter, of course, is extremely important to the acceleration of the foil and its subsequent behavior when irradiated by the NIKE laser pulse. Due to the interaction between the laser pulse and the foil, it is very important that the surface, and, therefore, the thickness characteristics of the foils be available to the NIKE laser project team for the analysis of experimental data resulting from the laser-target interactions.

There are several instruments employing various techniques for the examination of the morphology of surfaces. These include interferometers, atomic force microscopes, various stylus instruments, and other optical microscopes. We have elected to use the Photon Tunneling Microscope (PTM) as the best instrument by which to characterize the surface of

the foils used in the NIKE targets. This instrument has been discussed at length in various publications in recent times, Guerra [Refs. 4–1, 4–2] has provided both theoretical discussions of the PTM instrument and practical aspects of using the PTM for the examination of surfaces with vertical resolutions of tenths of a nanometer and a circular, lateral field of view about 100 μm diameter. The addition of a CCD array camera to the PTM allows us to store and analyze the target surface data directly with the aid of a computer. The computer files can also be sent, electronically, directly to NRL for their use and analysis. Our analysis is currently accomplished by using IDL software. The programs which we use provide Fourier Transforms from line-outs through the PTM image of a surface together with a plot of the z variations of the surface along lines of constant x or constant y in the surface. A Fourier power spectrum plot as a function of spatial wavelength of the surface, as viewed by the PTM, can be provided.

The data files acquired via the CCD array camera and the associated computer may be analyzed immediately, the files may be transferred electronically to NRL, or the files may be stored on an erasable magneto-optical read-write storage disc (230 MB/disc).

For further information please contact C. Hendricks (WJSA).

4.2. MICROENCAPSULATION OF LARGE SHELLS

In FY94 we demonstrated the capability to produce polystyrene shells with target quality diameters, wall thicknesses, sphericities and concentricities via controlled-mass microencapsulation. In order to provide target mandrels meeting the specifications of the Omega Upgrade program (shown in Table 4–1), the goals of this year's (FY95) task were to: (a) limit shell diameters to 850-1000 microns; (b) reduce the levels of vacuoles, dimples, and debris; and (c) make initial deliveries from Soane Technologies to General Atomics for subsequent coating operations. We have been successful in all of these areas.

4.2.1. SHELL DIAMETER ENLARGEMENT

To achieve the specific requirements of the Omega Upgrade, it was first necessary to limit shell diameters to the 850–1000 μm range; the previous production diameter range was 1000–2000 μm (1–2 mm). The diameter of shells produced in our system is primarily dictated by the inner diameter of the glass delivery tube which forms the annular stripper

TABLE 4–1
SHELL SPECIFICATIONS FOR THE OMEGA UPGRADE PROGRAM

Shell diameter	850–1000	μm
Wall thickness	5–15	μm
Concentricity	P1 < 1	μm
Vacuoles > 5 mm	0	Number allowed
3–5 mm	30	
1–3 mm	50	
<1 mm	200	
<1 mm	200	

flow in the triple orifice (refer to FY94 Annual Report for a schematic of the apparatus). Therefore, a decrease in the inner diameter of this tube was needed, which required a redesign of the orifice. The new triple orifice can produce shells of 800–1000 μm diameter; currently diameters of 930 μm are being produced on a regular basis. The redesigned orifice is easier to clean, assemble, and align than the old device.

4.2.2. VACUOLE, DIMPLE, AND DEBRIS REDUCTION

The occurrence of vacuoles, dimples, and debris are intimately related. Vacuoles are thought to be formed by the heterogeneous phase separation of water-rich droplets within the shell wall during solidification. Our past mass transfer modeling work predicted that the organic-rich wall phase "skins" early in the solidification process, as organics diffuse into the outer aqueous phase. This skinning traps the initially equilibrium-level amounts water in the wall, causing the water to supersaturate. Modeling also predicts that sub-micron (~0.5 μm) debris can serve as heterogeneous nucleation sites.

Guided by the insights provided by our modeling effort, vacuole levels have been reduced by two means. The first method was to remove sub-micron particles via filtering. Shell-making solutions are now filtered to as low as 0.02 μm. This has provided modest vacuole reduction. However, shells made from polymer solutions filtered to 0.02 μm showed two to three times as much cracking as those filtered only to 0.1 μm. Since the radius of gyration of the polystyrene (MW = 90,000) is about 100 Å, it is possible that such fine filtering removes the high-molecular weight tail of the distribution, reducing the strength of the shell wall. As a result, filtering is now limited to 0.1 μm.

The second method employed for vacuole abatement was to decrease wall thickness. Thinner walls provide shorter transport distances for water-rich droplets to diffuse to and exit the wall at its outer surface during solidification. In addition, since only vacuoles with diameters smaller than the wall thickness can exist in the wall, the higher-diameter vacuole population can be eliminated by reducing wall thickness. Figure 4–3 shows that vacuole levels are reduced with thinner walls and that acceptable levels can be obtained with wall thicknesses below 10 μm. However, thinner walls result in weaker shells which are more likely to crack or dimple during the solidification or ethanol extraction steps.

For shells of 1000 μm diameter and 10 μm wall thickness, dimpling can occur as newly-solidified shells cool from the solidification temperature back to room temperature and during the ethanol-water extraction processing step. As shown in Fig. 4–4, the theoretical thermal contraction of the aqueous core during the cooling step was found to fall in the same range as the observed dimpling volume, which was calculated from measured dimple diameters and depths. Experiments confirmed that the extent of dimpling is strongly related to the solidification temperature, as shown in Fig. 4–5. When solidifying below 500°C, core fluid contraction upon cooling creates implosion forces which are below the buckling threshold of the shell.

During the ethanol-water extraction step, water diffuses out of the shell core faster than ethanol diffuses into the shell. As a result, a (negative) osmotic pressure drop is created within the shell. As with the solidification cooling step, shells may dimple under the

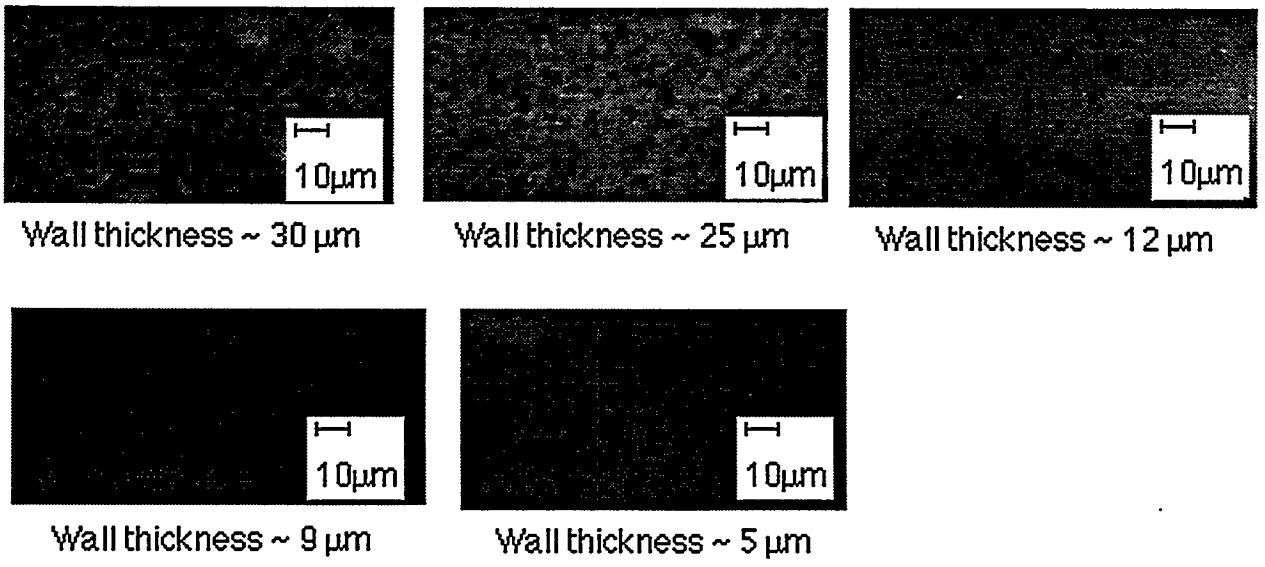

Fig. 4–3. Vacuole level variation with changes in wall thickness for microencapsulated polystyrene shells of 925 μm diameter.

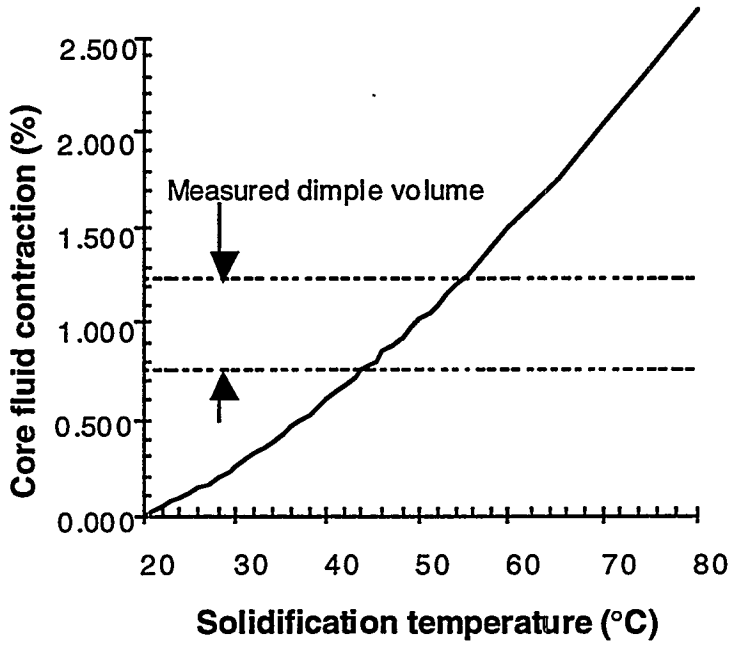

Fig. 4–4. Theoretical core fluid contraction upon cooling from the shell solidification temperature to 20°C.

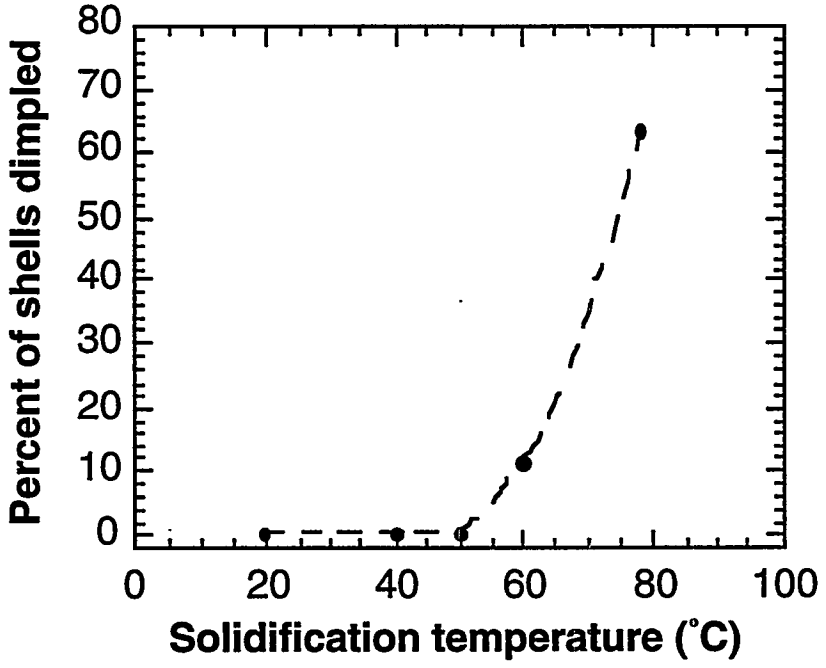

Fig. 4–5. Experimental percent of solidified shells dimpled following cooling from the solidification temperature to 20°C.

implosion forces. Gradual exposure to ethanol consisting of one day in a 50/50 ethanol/water mixture followed by one day in 100% ethanol was found to suppress dimpling.

During the ethanol-water extraction step, water diffuses out of the shell core faster than ethanol diffuses into the shell. As a result, a (negative) osmotic pressure drop is created within the shell. As with the solidification cooling step, shells may dimple under the implosion forces. Gradual exposure to ethanol consisting of one day in a 50/50 ethanol/water mixture followed by one day in 100% ethanol was found to suppress dimpling.

In addition to the advances made in vacuole and dimpling control, environmental debris levels were reduced by constructing and utilizing a HEPA-filtered shell handling area and a filtered shell drying chamber.

4.2.3. PRODUCTION YIELDS AND DELIVERIES

To identify which processing steps are most crucial and to improve over-all yield, the average yields of each processing step were quantified; results are shown in Fig. 4–6. The greatest losses occur at the very first cut in the process in which batches are rejected for unacceptable levels of vacuoles or debris. The debris sizes often exceed a few microns, suggesting that the source is not the shell-making solutions, which are filtered to 0.1 μm. One

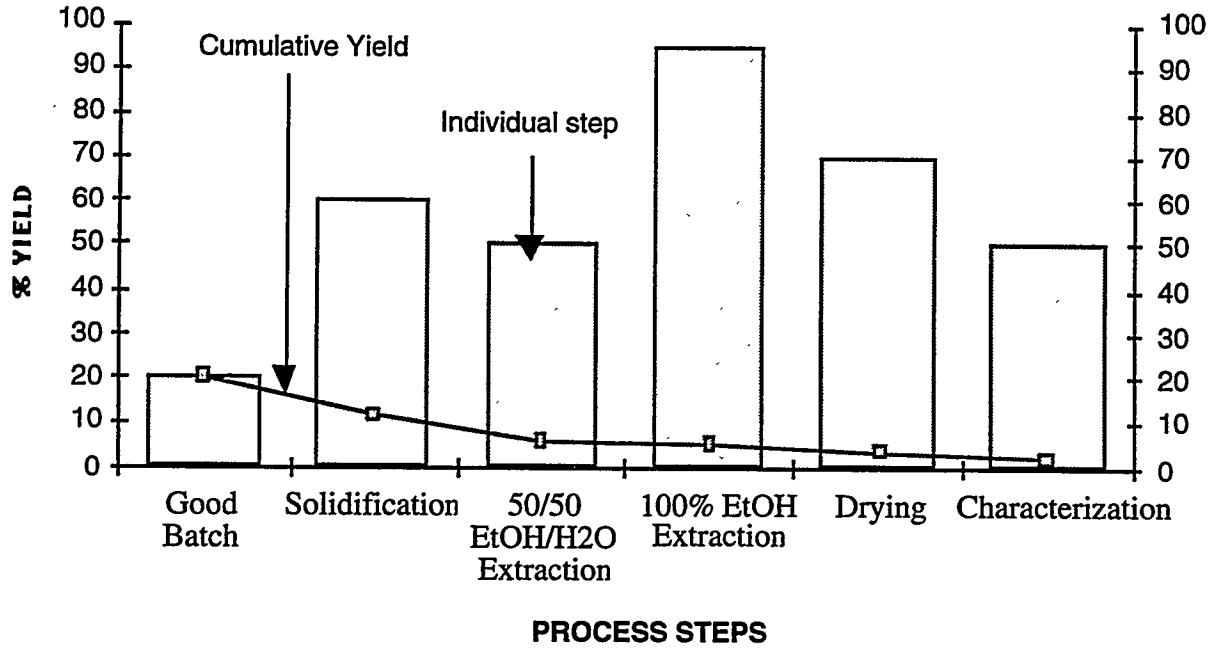

Fig. 4–6. Average yields for individual and cumulative processing steps of the current microencapsulation process. Shells have ~925 micron diameter and ~8 micron wall thickness.

possible source is the sloughing of PVA or PS residue in the triple-orifice or glass delivery tube from previous runs. To counter this, all fluid lines are now being purged extensively prior to each run. Another source could be debris from house air lines which are used to transport organics out of the aqueous solidification bath, during the solidification step.

The next most critical losses occur in the first (50/50) ethanol-water extraction step. Here, shells can crack from osmotic forces if there are weaknesses in the wall. Longer solidification times (e.g., three days, instead of eight hours) seem to improve the extraction survival rates, but may not be advantageous for higher production throughputs. The current overall yield (counting all batches of all shells encapsulated for solidification) is approximately 2%. Currently, with 10 batch attempts per week of 200 encapsulated shells per batch, 40 deliverable shells per week can be produced.

During the last three months of FY95, the five scheduled deliveries to General Atomics were fulfilled for subsequent GDP coating. Examples of the over-all shell quality and interference patterns are shown in Figs. 4–7 and 4–8. The characterization results of these deliveries is summarized in Table 4–2. All specifications for the initial Omega Upgrade mandrel requests were met.

During the last three months of FY95, the five scheduled deliveries to General Atomics were fulfilled. We have achieved our specified goals for polystyrene mandrel production; shell size, vacuole levels, dimpling and debris have been effectively controlled. Our current production capacity stands at about forty target-quality shells per week. Further improvements in yield are underway. According to Wayne Miller of GA, the surface finishes following subsequent GDP coating are within current target specifications. According to Mark Whitman at LLE, our microencapsulated polystyrene shells are currently the best within the ICF community.

4.3. GLASS SHELL PRODUCTION

The 1650°C furnace used to produce glass targets by the previous contractor was installed in the drop tower room as a subtask of the KMS close-out effort. Several runs were made initially to demonstrate that the installation was complete. An attempt was made to make large shells as they were deemed most difficult. The shakedown runs were very successful and several production runs have been made.

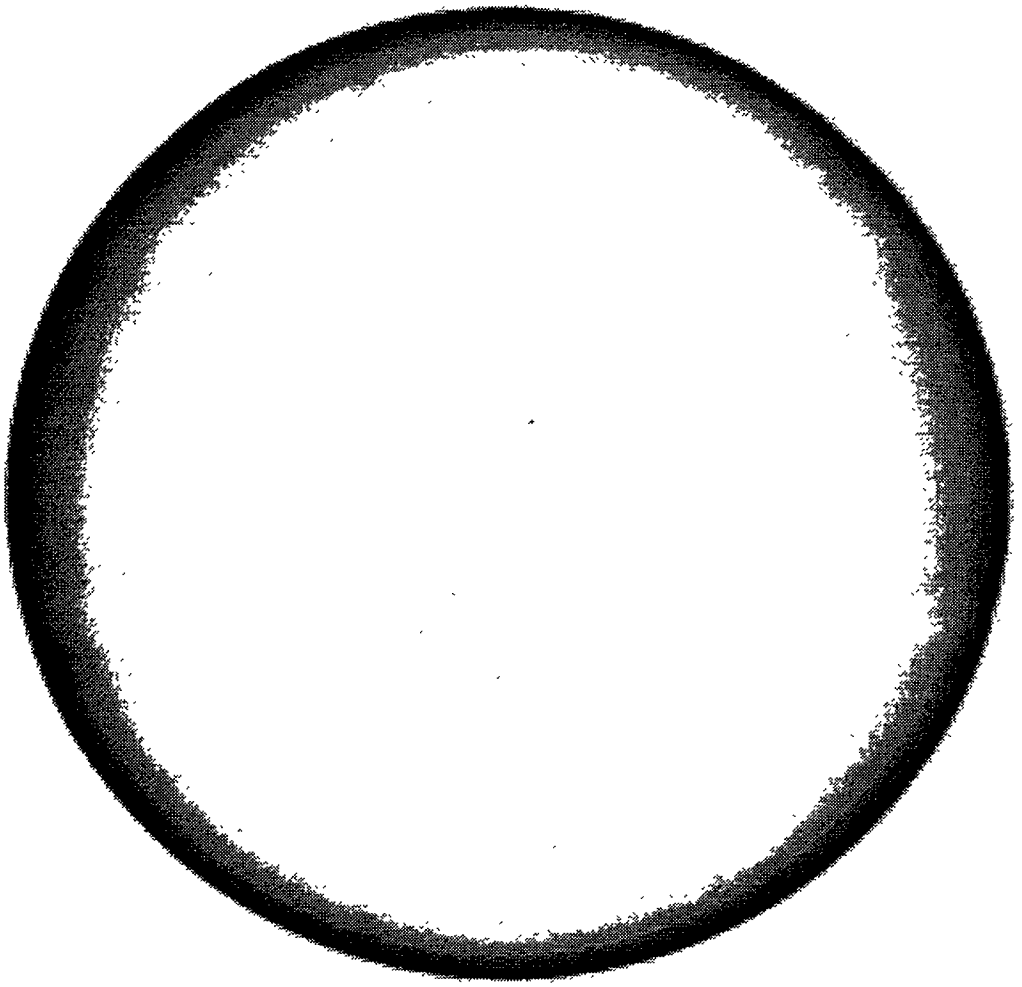

Fig. 4–7. Overview of a shell under 150x magnification

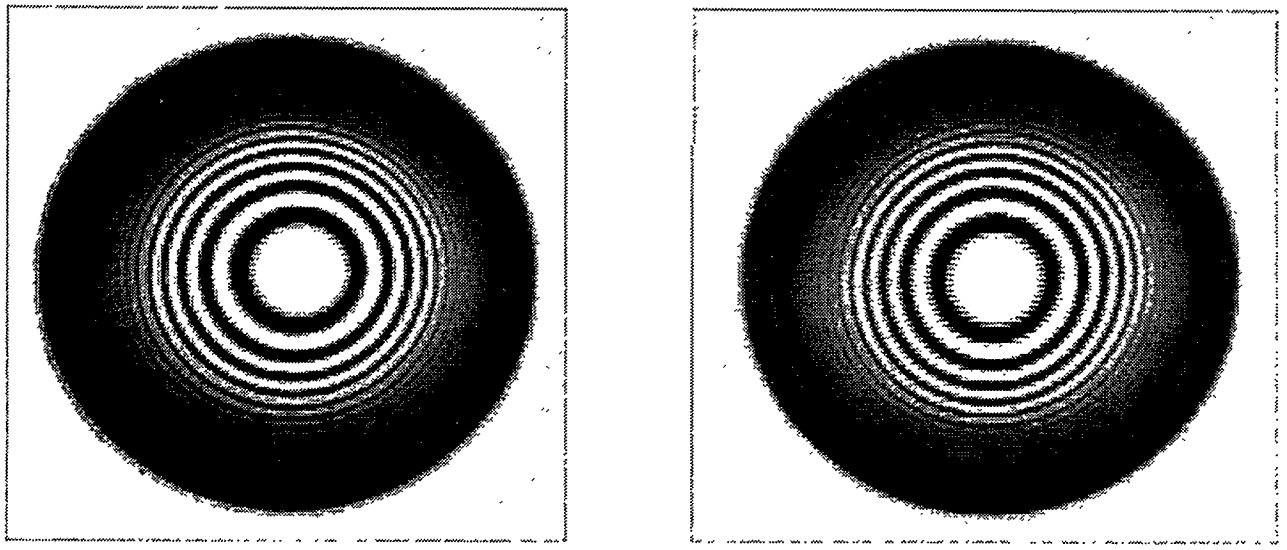

Fig. 4–8. Interference images of some delivered shells

TABLE 4–2
CHARACTERIZATION OF SHELL DELIVERIES MADE TO GENERAL ATOMICS FOR SUBSEQUENT COATING OPERATIONS

Date	No. Delivered/ Requested	Diameter (μm*)	Wall (μm**)	Percent NC†	Vacuole/ Debris
07/31/95	37/10	910	9.0	7 ± 4	Acceptable
08/15/95	21/15	924	8.8	8 ± 4	Acceptable
08/30/95	35/20	922	8.5	4 ± 3	Acceptable
09/15/95	44/40	910	9.0	4 ± 3	Acceptable
09/30/95	82/80	945	8.8	<5	Acceptable

*Diameter ±1%.
**Wall ±10%.
†% non-concentricity = white light fringe center offset/shell o.d./2 x 100.

The furnace atmosphere is very important in blowing large shells. It was found previously that high concentrations of water vapor in the tower increased the yield of large shells. Water vapor is thought to affect the shell blowing process due to its very high permeability through molten glass which decreases the viscosity of molten glass and results in higher pressures inside the shell during the blowing process. Other gases such as oxygen, nitrogen and carbon dioxide have much lower permeability. Gases such as helium will have high rates of diffusion through the shell but do not reduce the glass viscosity and thus are inferior to water vapor.

KMS used a hot water harvester to catch the shells thus providing a water vapor concentration at the bottom of the tower equivalent to the vapor pressure of water at the harvester temperature. The water vapor concentration decreased with distance up the tower due to diffusion. We improved on this by addition of a helium purge. This provided three advantages. Replacing the air in the tower with helium provides an additional high mobility species which can diffuse through the glass and increase the internal gas volume. Addition of a gas purge below the liquid level in the harvester means that there is a net flow of gas up through the furnace. Whereas diffusion results in a steady-state water vapor concentration decreasing linearly from near one atmosphere at the bottom to zero at the top, steady flow provides a constant water vapor concentration throughout the furnace. The helium flow can be pulsed causing the shells to tumble as they fall resulting in improved shell wall uniformity.

The initial implementation of this technique used a beaker of water on a hot plate as the harvester. Helium was pulsed beneath the water level under the furnace tube extension. Although this showed signs of progress there was a great deal of shell breakage due to the violence of the vaporization when helium was injected beneath the water level. Figure 4–9 shows the shell harvester constructed to minimize shell breakage. A stagnant annular region is provided to harvest the shells. Helium pulsing was initially provided by a resistance-capacitance oscillator where the capacitance was provided by a large gas volume and the resistance by the water pressure head. Recently this has been replaced with an electronic timer and a pair of solenoid valves.

The only other significant change in operation from the previous contractor is the use of the operator-independent particle injection system. Previously, frit was injected into the furnace by hand using special scoops. It was found that whereas one operator could use one scoop and get consistent results, another operator using the same scoop would get different

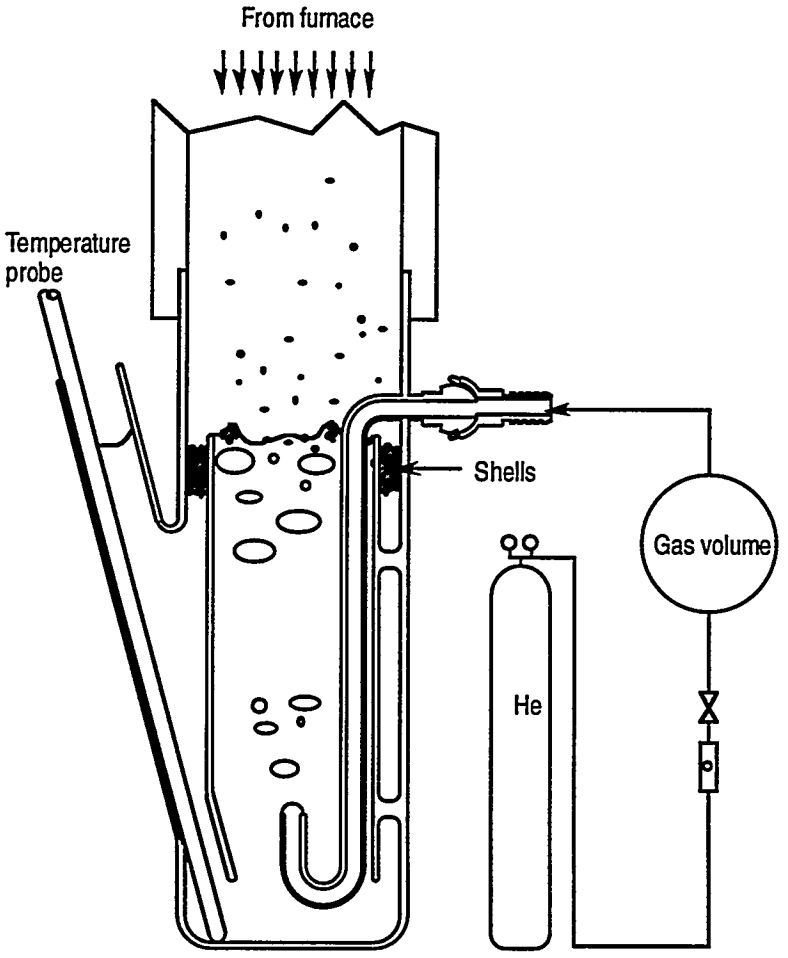

Fig. 4–9. Glass shell harvester

results. The difference was assumed to result from the precise way the scoop was turned over and flicked down the tower.

The only other significant change in operation from the previous contractor is the use of the operator-independent particle injection system. Previously, frit was injected into the furnace by hand using special scoops. It was found that whereas one operator could use one scoop and get consistent results, another operator using the same scoop would get different results. The difference was assumed to result from the precise way the scoop was turned over and flicked down the tower.

We devised a new frit injector (Fig. 4–10) to remove operator dependence. A fixed volume charge of glass precursor is dropped into the top of the furnace on the end of a 1/4 in. diameter stainless steel tube. When the injector stop hits the guide, the charge continues down the furnace. The injector bounces up and is quickly withdrawn before heating significantly. The glass precursor volume is defined by the recess in a socket head cap screw. Many charges can be prepared ahead of time and screwed by hand into the injector as they are used. The precursor is retained in place by a small disk of 2-micron XRF film fixed over can be added to the furnace in a short time reducing the time the shells spend in the harvester the cavity with stopcock grease. The film burns when the charge is injected. Many charges and thus reducing shell breakage. An insulation plug in the top of the furnace which reduces operator exposure to the bright light and high temperature of the furnace also reduces turbulence. Since the injector transports the particles through the high temperature gradient at the top of the furnace the yield is significantly improved.

One area of operation which has not been improved is the glass precursor. Sufficient glass precursor was available from the previous contractor for many runs. We believe that monosized spherical precursor can be made which should improve target uniformity.

These techniques have resulted in the production of larger quantities of large glass shells. Many batches have been made aimed at making shells of over 1200 microns, as shown in Fig. 4–11. Shells of over 1600 microns have been made and there are signs of shells approaching 3000 microns (Fig. 4–12). Spherical precursor could be an aid in making large shells as large frit particles tend to fragment due to thermal expansion.

Before the glass shells can be filled with tritium they must be buckle and then burst tested. Batches of shells are put in a pressure vessel and pressurized to a couple atmospheres

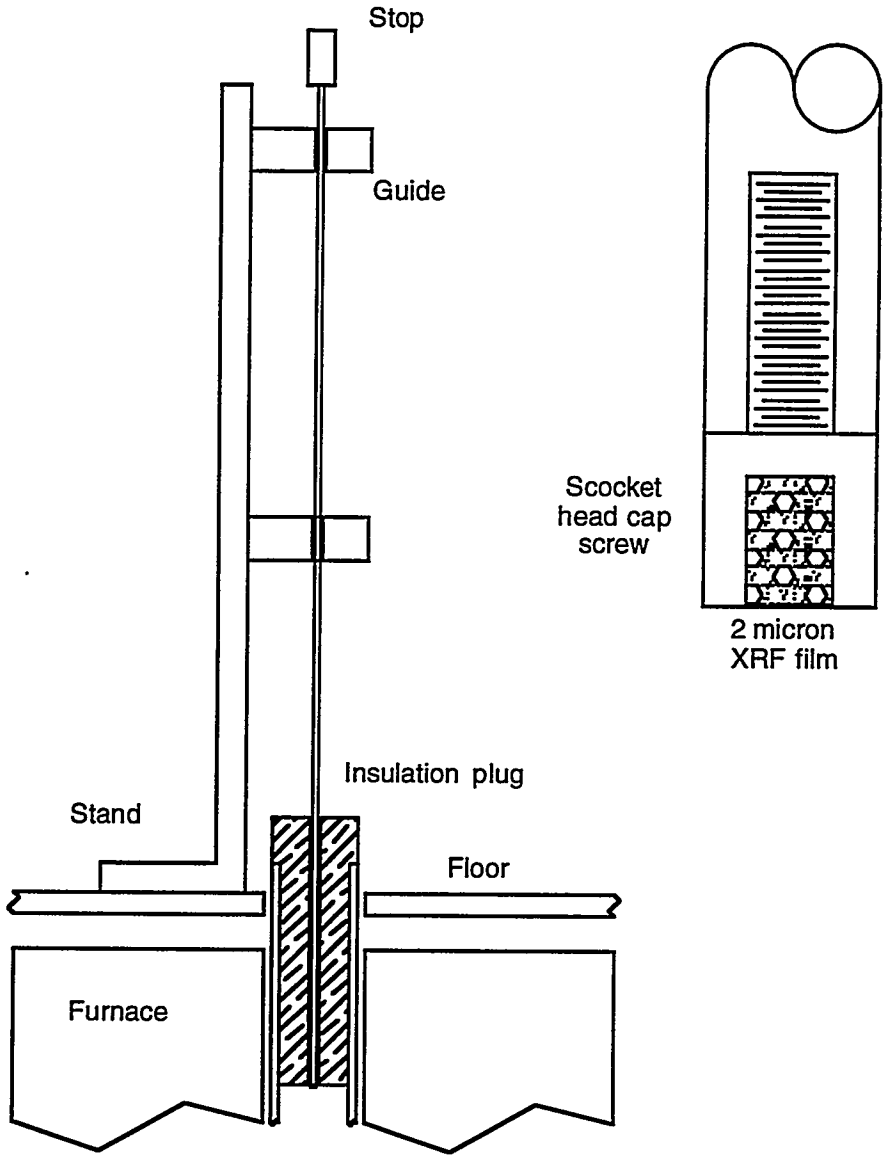

Fig. 4–10. Glass precursor injector

of pressure (Fig. 4–13). Weak shells which could not take the two atmosphere helium pressure step break thus increasing the yield from the time consuming burst pressure step.

Burst testing involves diffusion of helium into shells contained in egg crates, at 350°C, to a final pressure of up to 50 atmospheres. The pressure is increased in two atmosphere steps with sufficient time (6 min) between steps for the helium to diffuse through the glass. After equilibrating at the final pressure a valve is opened to atmosphere allowing the full pressure across the shell wall.

The PAMS process combines several prospective advantages over current drop-tower or microencapsulation processes for producing mandrels with a high degree of wall uniformity and sphericity, a greatly desired property in ICF capsule targets.

1. The shake and toss process or solution droplet generator generally produces shells which are much more concentric and spherical than conventional drop tower shells.

2. Problems with vacuole formation in microencapsulated mandrels are not nearly as critical — the PAMS mandrel is removed in the final product.

3. GDP coatings (and thus mandrels) have no vacuoles.

Our task was to transfer the shake and toss PAMS process capability from LLNL to General Atomics, develop the process toward production (produce PAMS shells, GDP coat the PAMS shells, and then pyrolyze away the PAMS). We were also to supply some PAMS mandrels to LLNL for further pyrolysis studies.

4.4.1. PAMS MANDREL DELIVERIES TO LLNL

PAMS mandrels delivered to LLNL during this task were produced by the Osaka shake and toss method. A total of 585 PAMS shells were delivered between the end of June and the end of September. These shells met the desired specifications. Ten shells were delivered between 1600–2000 μm o.d., 75 shells between 850–1050 μm o.d., 300 shells (from a single batch) 400–600 μm o.d., and 200 shells in the range 430–500 μm o.d. The conditions for shell production were as follows:

1. The PAMS was 88 K MW with polydispersity of 1.04, (from Scientific Polymer Products).

2. Ten to 12 wt. % PAMS density matched solution of either of two solvent systems: benzene and 1,2 dichloroethane, or ethylethylketone (EEK), toluene, and 1,2 dichloroethane.

3. PVA solution concentration was 0.005–0.1 wt. % and filtered to 0.2 micron. Stirring was done with mixers equipped with low shear stir blades.

4. Curing temperatures were 50°–70°C, for 3–5 hours.

Although the delivered shells met the requested specifications, closer scrutiny of the PAMS mandrels showed several undesirable characteristics.

1. A very large fraction (~90%) were cracked.

2. A significant fraction (~50%) of the shells had material on the inside, which is presumed to be PVA.

3. There was a substantial surface debris problem.

4. Many shells had a rather large Δwall.

5. There were shallow pits in the PAMS surface.

These problems, especially Items 2 and 3, have been encountered many times before on microencapsulated mandrels and thus are not surprising. However, considerable progress on reducing the occurrence and severity of these defects in the millimeter sized normal polystyrene microencapsulated has occurred during the past couple of years. Thus we believe that with some additional effort we can fairly quickly overcome these problems with the PAMS method.

In fact, we already have identified some of the causes and are making progress towards solving them. Our analysis has shown the cracking was occurring in the ethanol exchange step, especially at ethanol/water concentrations of 50/50 or greater. The surface pits, roughly 1 μm in diameter and 0.05 μm deep, discovered by AFM measurements, were not anticipated. However, a quick survey of some microencapsulated normal polystyrene shells on hand showed some pits as well, although significantly smaller in size and fewer in number.

4.4.2. PRODUCTION OF PAMS SHELLS BY DROPLET GENERATOR

In contrast to the shake and toss method a droplet generator permits the production of a narrow distribution of PAMS shells in a single size (outer diameter and wall thickness). Secondly, since a dual orifice device places the interior water (W_1) within the growing PAMS/solvent (O_1) sphere, no PVA should enter the formed shell. Thus, the droplet generator has the potential to make PAMS shells which will pyrolyze cleanly to leave no PVA on the interior of the GDP mandrel.

A GA owned droplet generator system, patterned after the system used at ILE in Osaka, was used to perform the work. A PVA stripping fluid was used to knock the growing liquid ball off the orifice. Syringe pumps supplied the O_1 and W_1 down the concentric needles. The exterior needle was made of glass, so the position of the interior needle could be changed and positioned to give a good droplet stream. Operational conditions were typically a PVA stripping fluid (0.1 wt. % PVA, filtered to 0.2 μm) of about 200 cc/min, W_1 of 20 cc/hr, O_1 of 20 cc/hr (12 wt. % PAMS in EEK/toluene/1,2 dichloroethane). The wet solvent/water balls were passed down some 3 ft of tygon into a stirred 1000 ml beaker containing deionized, filtered PVA solution. The filled beaker was then placed in a water bath at 50°–60°C, and stirred for 3–5 hr to cure the mandrel.

Ethanol exchanges, followed by removal of the ethanol under vacuum, resulted in dry shells with dimensions of 1120 μm x 18 μm (o.d. x wall thickness). The average Δwall improved substantially to only 1.9 μm, as opposed to the value of 5 μm in the shake and toss shells. A Δwall <2 μm is probably sufficient to ensure acceptably uniform GDP coatings during the coating step. Unfortunately, like the shake and toss mandrels, these droplet generator mandrels exhibit shallow pits and debris remains to be a problem.

However, to reach even this stage of shell production in the short time we have been working on it has required solving several problems along the way.

1. Agglomeration of the PAMS mandrel during the curing step.

2. A localized thin spot in the shell wall, akin to a "belly button."

3. Ethanol exchanges resulted in low yield of shells, due to extensive cracking.

We had originally tried using fluorobenzene as the O_1 solvent (successfully used in the normal polystyrene system) but upon heating to 60°–70°C to cure the mandrel in a 5 wt. % PVA solution, the shells would suddenly agglomerate approximately 1 hr into the cure. We found we could avoid the agglomeration by using benzene plus 1,2 dichloroethane for the O_1, and by stirring the shells in a "rotobeaker" for a couple days at room temperature. We also found that EEK/toluene/1,2 solution does not agglomerate. The localized thin spots were readily eliminated by stirring the solution rather than letting the shells sit on the bottom of the beaker during curing.

The ethanol exchanges have continued to produce a low yield of shells. Once one reaches beyond a 50/50 mixture of ethanol/water, the majority of the shells crack. Very few

floating shells (where a nucleated bubble is in the interior) are found. This we believe is due to increased osmotic pressure resulting from the ethanol exchange times which are 10–30 times longer than our previous experience with polystyrene shells. Compared to a 500 μm o.d. shell and 5 μm wall, which requires 24 hours to exchange, these shells require 30 days to exchange. We have subsequently gone to smaller increments in increasing the ethanol concentration to minimize the osmotic pressure shocks. We have also ordered higher MW PAMS, which should exhibit greater wall strength.

4.4.3. GDP COATING AND PYROLYSIS OF PAMS SHELLS

PAMS shells (500–1100 μm o.d.) were then coated with 3–20 μm of GDP using the standard GDP process. Pyrolysis work was performed in a vacuum oven. Following LLNL protocol, pyrolysis of the GDP coated shells was performed at 325°C for 1000 minutes, after a short ramp to temperature.

Characterization Results (Shake and Toss). The GDP mandrels, resulting from coating the shake and toss PAMS shells and then pyrolyzing, shrank in o.d. by about 3%–5% during the pyrolysis. A 5 μm thick coating of GDP resulted in a GDP mandrel which on average was ~6% non-concentric (NC), which is larger than desirable. The nonconcentricity of the GDP mandrel is caused by non-uniform GDP coating a PAMS shell with a significant Δwall (the thicker wall prefers to orient down in the coater).

Characterization of the GDP coated PAMS by the sphere-mapper and normal SEM demonstrated that the debris present on the surface of the PAMS resulted in even larger domes in the surface of the GDP. A second flaw in the resulting GDP mandrel results from the pits in the outer surface of the PAMS shells. The inner surface of the GDP mandrels exhibit shallow domes, of the about same dimension as the pits in the original PAMS mandrel.

Characterization Results (Droplet Generator). One of the best batch of droplet generator PAMS shells has been GDP coated, and then pyrolyzed. After the pyrolysis, the GDP layer o.d. shrank in size by 3%, resulting in shells $1065 < \text{o.d.} < 1085$ μm and 5.9 μm wall thickness. The average Δwall was about 1 μm, and non-concentricities ranged from 3.5% to 13.5%. Although these GDP mandrels are still are not as uniform and surface defect-free as is desired, we are getting close.

4.4.4. RESULTS OF LLNL WORK

The supply of PAMS shells to LLNL permitted them to do further work on GDP coating and subsequent pyrolysis studies. These studies showed improved GDP mandrels made from PAMS shells, as compared to PAMS beads. First, earlier work on GDP coated PAMS beads led to minimum GDP mandrel wall thicknesses of about 15 microns. With the PAMS shells, LLNL could make GDP mandrels with wall thicknesses of about 5 microns for 900 micron o.d. shells, and 2 micron for 450 micron o.d. shells. Associated with this result, the nonconcentricity of the GDP mandrels from some of the best PAMS shells decreased to less than 1.4%, which is not perfect but satisfactory. This decrease is apparently due to the lack of bubbles of alpha-methylstyrene vapor, formed from the beads, deforming the GDP coating. The shells provide sufficient volume for the vapor to expand, reducing the deformation. Third, the pyrolysis time was decreased from 2000 minutes for beads, to 500 minutes for the shells. This decreased time results in less darkening of the GDP mandrel. The results suggest that once we finish solving the surface defects (debris/pits), GDP mandrels made via the PAMS process will be state-of-the art for millimeter sized shells.

For further information please contact B. McQuillan (GA).

4.5. REFERENCES

[4–l] Guerra, J. M., Applied Optics **29**, 3741 (1990).

[4–2] Guerra, J. M., Applied Optics **32**, 24 (1993).

5. CRYOGENIC SCIENCE AND TECHNOLOGY DEVELOPMENT

The OMEGA laser at the University of Rochester and the National Ignition Facility will need cryogenic targets. We supported the ICF Labs in developing the science and technology of cryogenic fuel ICF targets.

5.1. CRYOGENIC LAYERING DEVELOPMENT

D. Bittner, J. Burmann, and J. Sater conducted cryogenic layering experiments in collaboration with the LLNL staff. Analytical modeling support was provided by R. Bieri, E. Monsler, and M. Monsler.

5.1.1. JOULE HEATING

An extensive experimental program studying beta-layering in tritiated ICF targets has been under way for several years [Refs. 5–1, 5–2]. Beta-layering is driven by internal heating of the solid due to the beta-decay of tritium. Inhomogeneities in layer thickness cause local temperature variations, which translate into differences in local saturated vapor pressures. This results in material moving from warm to cold spots until an equilibrium isothermal surface is reached. The best estimates to date for a beta-layer give a surface roughness of 2 μm rms inside a cylinder 2 mm in diameter [Ref. 5–3]. This layer does not meet the surface finish target specifications for a direct drive target for Omega Upgrade.

G. Collins of LLNL has been looking at the surface roughness of non-tritiated hydrogen layers [Ref. 5–4]. He finds that by increasing the heat flux through the surface, smoothness is greatly improved. His process differs from beta-layering in that the gas is directly heated, and the gas then heats the solid by conduction. Thicker regions become warmer, and, just as in beta-layering, material moves from warmer areas to cooler regions.

A joint effort between LLNL and WJSA is underway to replicate these results in a shell filled with D-T. We will assist the beta–layering process by accelerating free ions in the gas with a radio frequency (rf) electric field. The free ions are created by collisions of beta-

particles with molecules in the gas. These accelerated ions then heat the rest of the gas by a collisional transfer of energy. Our best estimates to date indicate that it will require an electric field strength on the order of 5 kV/cm to dissipate 1 mW/cm^2 in a D-T capsule. We have made good progress this year. The experimental apparatus and some preliminary work with D_2 are complete. We are currently beginning D-T experiments.

Fill Station. The fill station, shown in Fig. 5–1, is designed to be a source of D-T requiring no external mechanical pumps. It is constructed according to standard tritium practice. There are no elastomers in the vacuum system, and the tubing and valves are all of stainless steel construction.

The heart of the fill station is the palladium (Pd) bed. This bed acts as both a D-T gas source and as a D-T pump. Palladium forms a metal hydride with hydrogen and its isotopes. The hydriding reaction is reversible and can be controlled by adjusting the temperature of the bed. When heated to a temperature on the order of 150°C, hydrogen gas is released from the Pd. When cooled to liquid nitrogen temperatures, the Pd acts as an excellent adsorber of hydrogen. Our bed consists of a stainless steel bottle containing powdered Pd placed in a combination dewar/heater assembly. The bed is located between valves VA and VD in Fig. 5–1. The deuterium (D_2) bottle serves as a source of purge gas. This gas is used to sweep the system free of residual D-T before breaking into the gas lines for maintenance.

The cryopump consists of a charcoal getter placed into a dewar of liquid helium. The pump is capable of adsorbing the ^3He created by the tritium ß decay reaction as well as any other residual gases resulting from tritium handling operations. The D_2 purge gas is also adsorbed onto the charcoal getter. After the pump is filled to capacity or the Pd bed needs to be recharged, we will ship the whole package to a suitable tritium facility in a UC-609 shipping container. The getter will be emptied, the bed recharged, and any waste products disposed of safely.

Cryogenic System. The cryogenic cooling system is shown in Figs. 5–2 and 5–3. Figure 5–2 is a sketch of the sample cell region. The sample cell consists of a short sapphire rod with a cylindrical hole perpendicular to the axis. The hole is sealed with windows on either end. Gas is admitted into the space with a fill line. The cell is cooled by conduction through a weak thermal link to a liquid helium bucket dewar with the minimum temperature achievable on the order of 8 to 9 K.

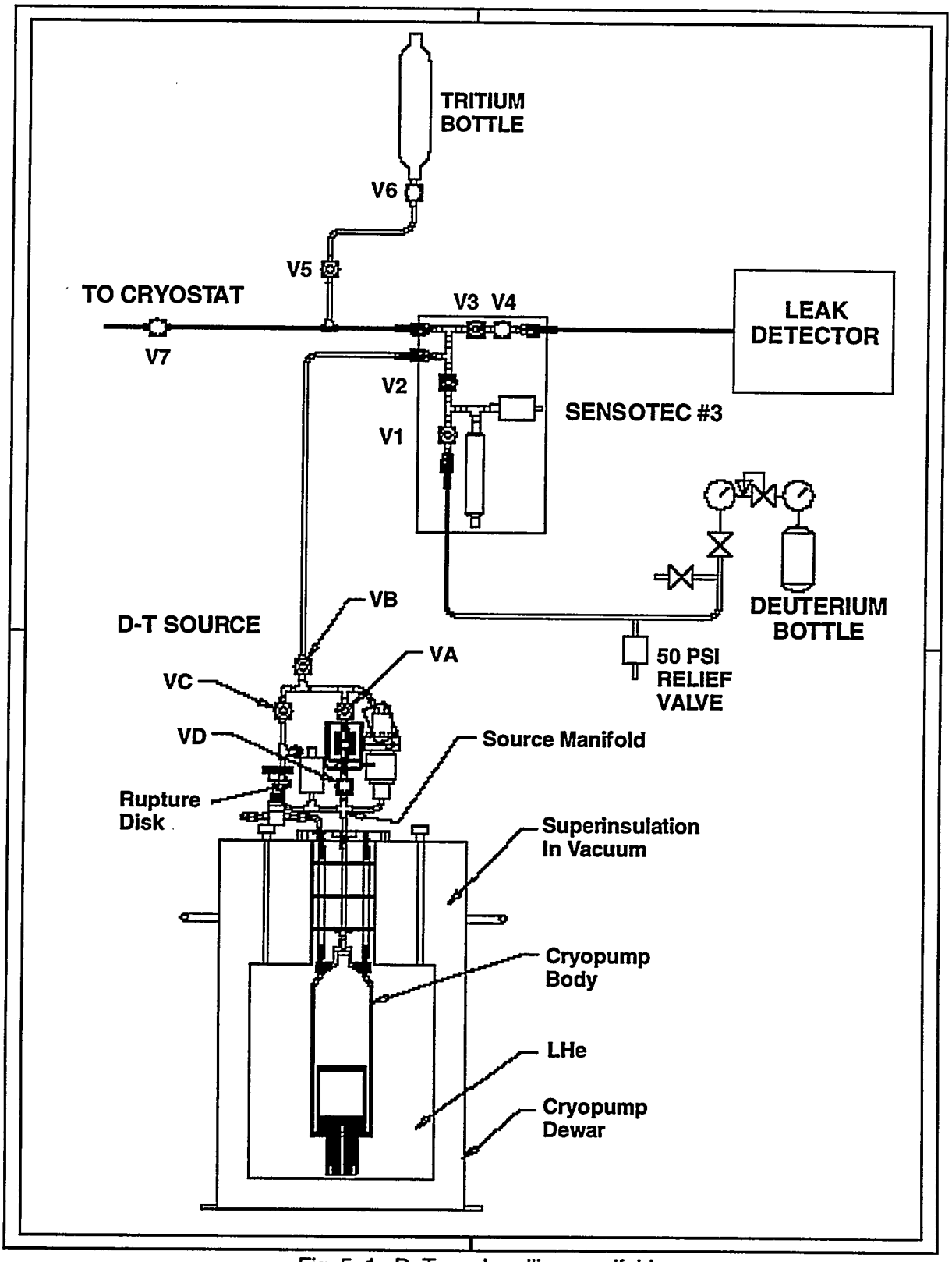

Fig. 5–1. D–T gas handling manifold.

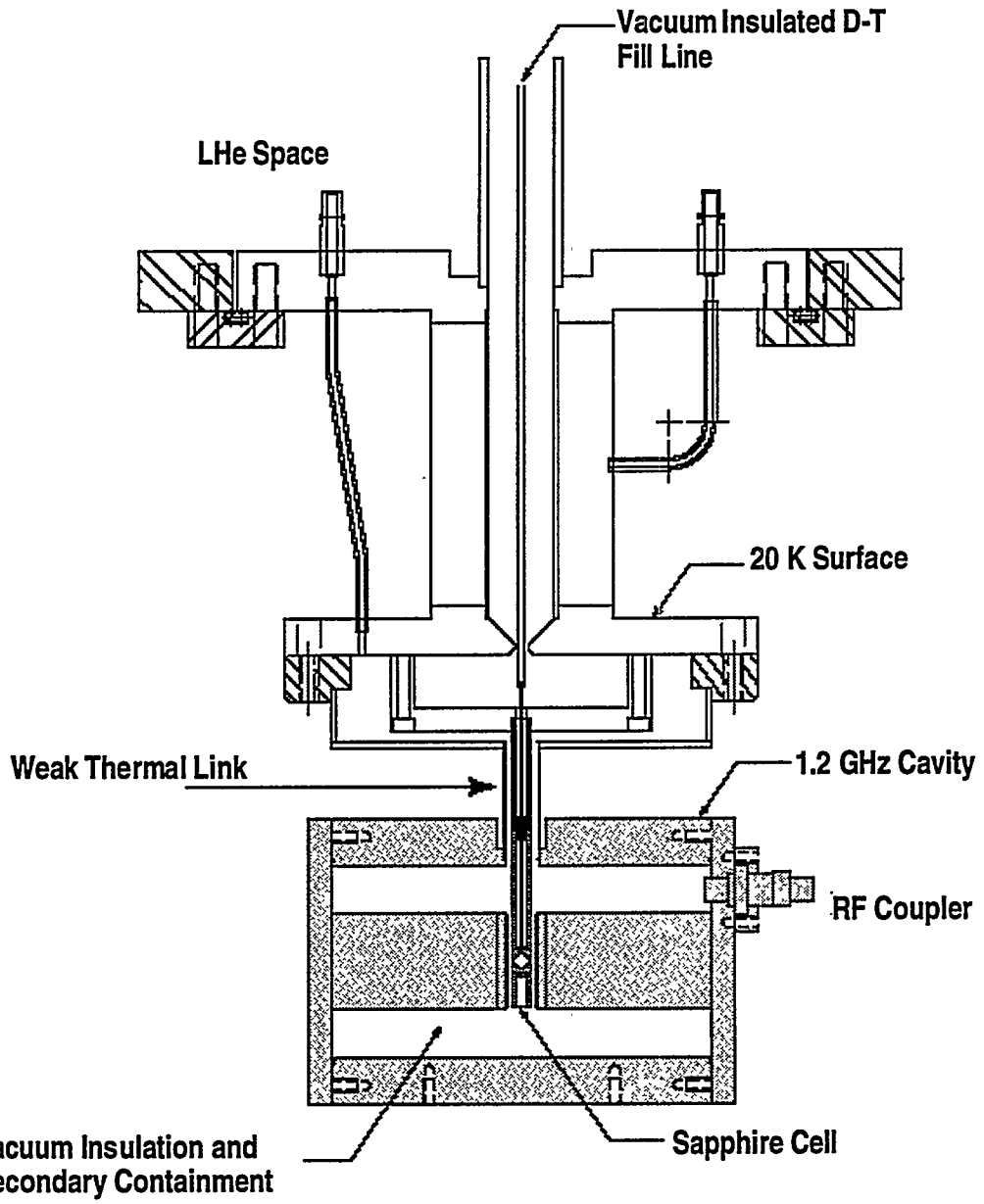

Fig. 5–2. Detail of microwave cavity and sapphire cell.

The 1.2 GHz cavity is a resonant structure used to generate the intense electric fields necessary for this experiment. Tens of watts of microwave power will necessarily be dissipated in this structure to create the desired electric field. In order to keep this large heat load from overheating our sample cell, an auxiliary cooling system, shown in Fig. 5–3, conducts the excess heat away. The cooling power is provided by a CTI 1020 mechanical

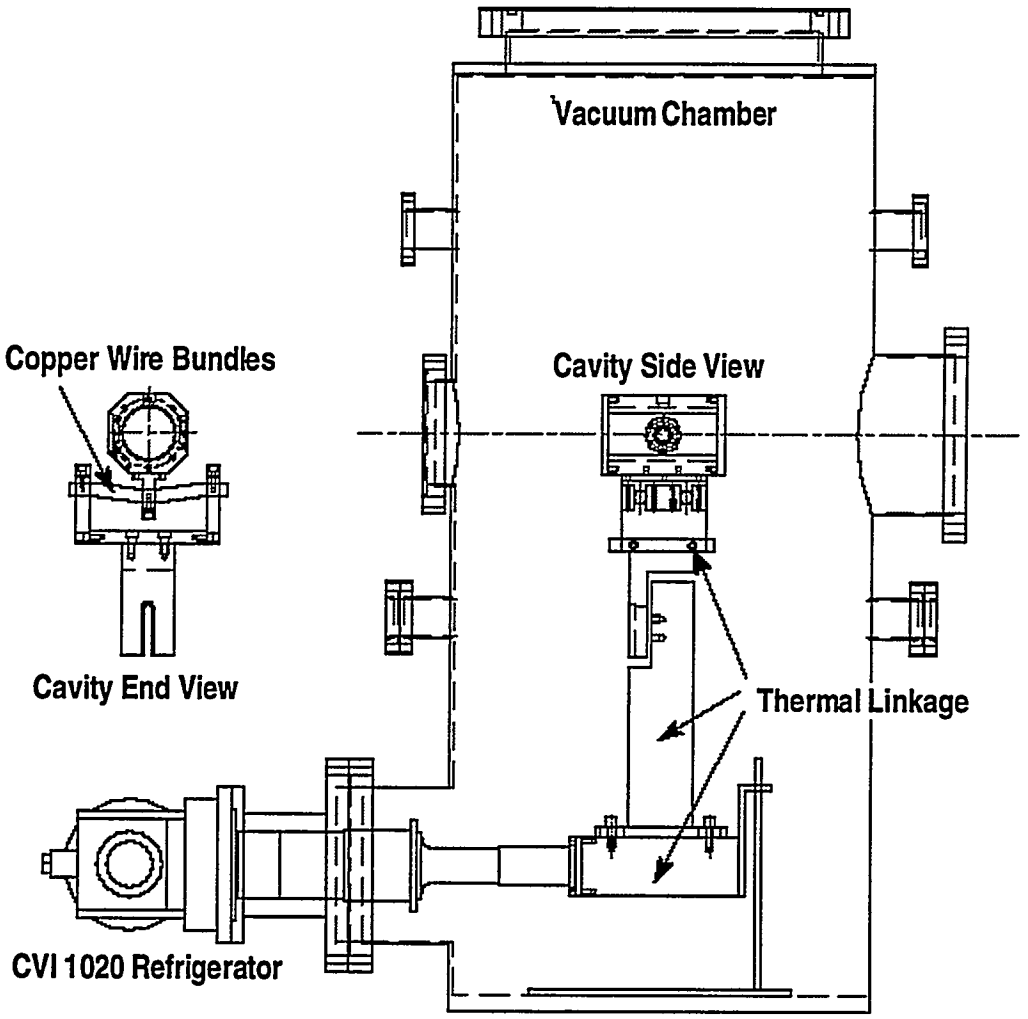

Fig. 5–3. Apparatus for cooling microwave cavity.

refrigerator connected through an oxygen-free high conductivity (OFHC) copper super structure to the microwave cavity. A flexible thermal coupling between the refrigerator and cavity prevents differential thermal contraction of the apparatus from causing damage. Our flexible coupling, shown in the cavity end view, consists of a 0.5 in. thick copper wire bundle made from 0.003 in. o.d. OFHC copper wire strands.

Microwave System. We require an electric field strength of approximately 5 kV/cm for this experiment. In order to avoid space charging and to effectively heat the D-T gas we

must use an alternating field with a frequency above 100 MHz. We chose to work in the 1.1 GHz region for practical reasons:

1. We could use a microwave cavity with reasonably high Q (Q = energy stored/energy loss per cycle). A high Q cavity has a larger field strength for a given power input. Since any power put into the cavity has to be dissipated by our refrigeration system, lower power is desirable.

2. The cavity is of a convenient size, neither too large nor too small.

3. We could borrow a power amplifier in this frequency range.

The microwave cavity is of a reentrant design [Ref. 5–5]. It is a design commonly used in klystrons and other applications where uniform microwave electric fields are desired. We use a loop coupler to couple the microwave power into the cavity. The electric field is most intense and uniform between the two pole pieces where we place our sample. A field map is shown in Fig. 5–4.

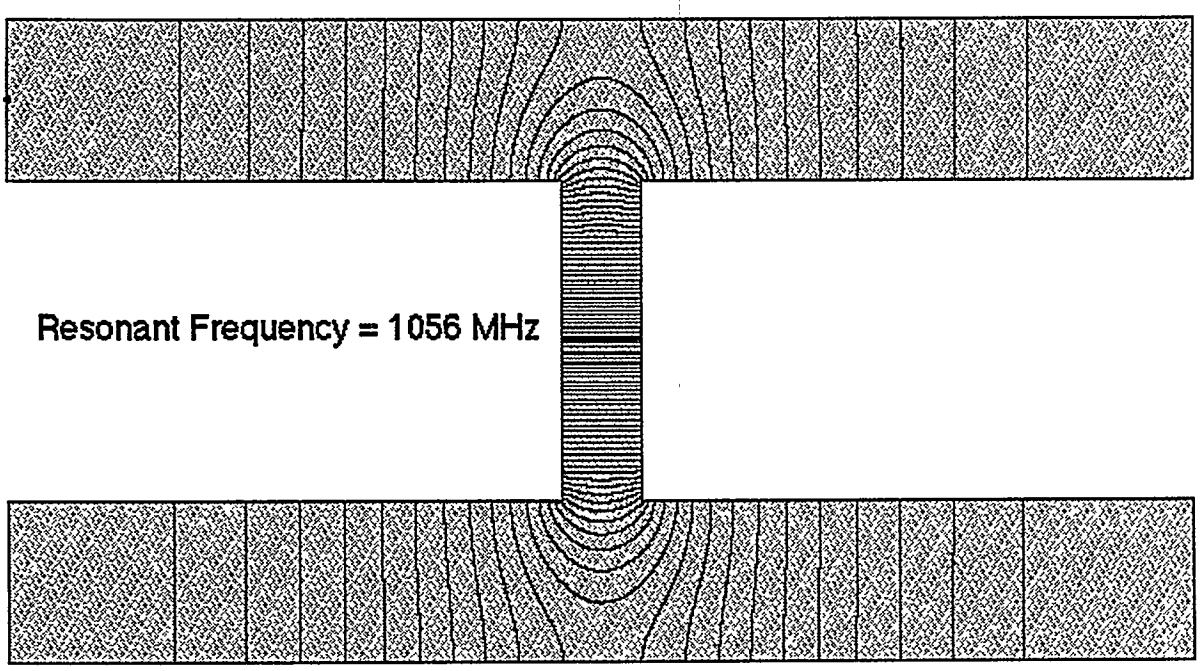

Fig. 5–4. E-field map of microwave cavity.

We have examined this design using a LANL code called Superfish. Models indicate our cavity design should have an unloaded Q of 40,000 at 20 K and require an input power of

approximately 5 W to generate a field of 10 kV/cm between the pole pieces. Our loaded Q was measured to be 7700 at a VSWR of 1.20. This corresponds to an unloaded Q of 14,000 and a required power of 14 W. At this point we attribute the difference between the model and the measurement to our poor knowledge of the cavity wall resistivity at 20 K and that Superfish is a 2-D code and unable to account for the inclusion of windows in our design.

Figure 5–5 is the basic layout of the microwave system electronics. The network analyzer serves as a very accurate and stable frequency source. We will also use its basic measurement capability to determine how well power is being coupled into the resonant microwave cavity by looking at how much reflected power reaches the directional coupler. The directional coupler diverts part of the amplified signal traveling in the forward and reverse directions to the A and B inputs of the network analyzer. By measuring the ratio of transmitted and reflected power, we can determine and optimize the coupling to the cavity.

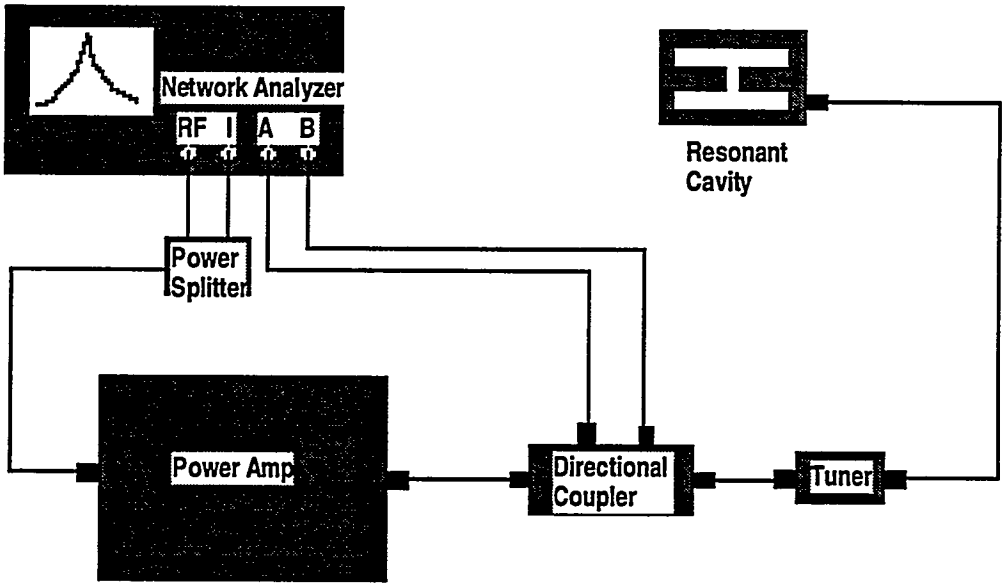

Fig. 5–5. Layout of microwave electronics.

The power splitter returns a portion of the network analyzer output for use as a reference signal with the balance of the signal delivered to the power amplifier stage. We have the capability of amplifying the signal to 100 W. The actual power needed depends on the Q and coupling efficiency of the microwave cavity. With the directional coupler diverting less than 1% of the amplified signal, the major part of the signal is passed to a two stub tuner and from there to the rf cavity.

In the coming year we plan to investigate the possibility of using a superconducting cavity. Superconducting cavities have been reported in the literature to have Qs in the hundreds of thousands. This would substantially reduce the heat load due to the incident microwave power. Our goal is to be able to place a plastic shell filled with D-T in a cavity filled with helium gas. The shell would be cooled by conduction. This requires that the cavity refrigeration must be able to maintain the temperature somewhat below the triple point of D-T.

Modeling. It is necessary to know the amount of attenuation of the electric (E) field inside our sample cell compared to the average field between the two pole pieces of the resonant cavity. We also need to know the distribution of the electric field magnitude within the cell. Since the local heating in the gas varies as E^2, the resulting isotherms in the sample cell will affect the shape of the ice layer. We are addressing these problems using finite element analysis.

Maxwell 3-D is an adaptive finite-element code for solving electrostatic problems. We use it to model the sapphire sample cell and surroundings. The static solution is a very good approximation of the rf field solution. The two poles act as a parallel plate capacitor, which in our model are two plates spaced 7 mm apart and at potentials of +350 and –350 V. The electric field between the two plates is 1000 V/cm without a sapphire cell and ignoring edge effects. The dielectric constant of the sapphire, of the volume inside the cavity and test cell, and of the fused silica window were assigned values of 10, 1, and 3.78, respectively.

The magnitude of the electric field in the smooth cell is shown in Fig. 5–6. The curve labeled "Center of Cell Cylinder" shows the magnitude along the axis of the hole through the sapphire, from the symmetry plane to the window. The other curves are values taken on perpendicular line segments across the circular cross section of the cell. The field strength varies from $5.73–6.06 \times 10^4$ V/m or 57% to 61% of the applied field.

The electric field magnitude along the line segment perpendicular to the plates does not appear to have the left/right symmetry that it should. This asymmetry is most visible in this plot because the field is relatively uniform, and mesh effects become appreciable. If the values along this line are flipped left to right and the difference taken, the amount of asymmetry is found. Since, in reality, the field should be symmetric, the roughly 0.9% variation is clearly a residual error.

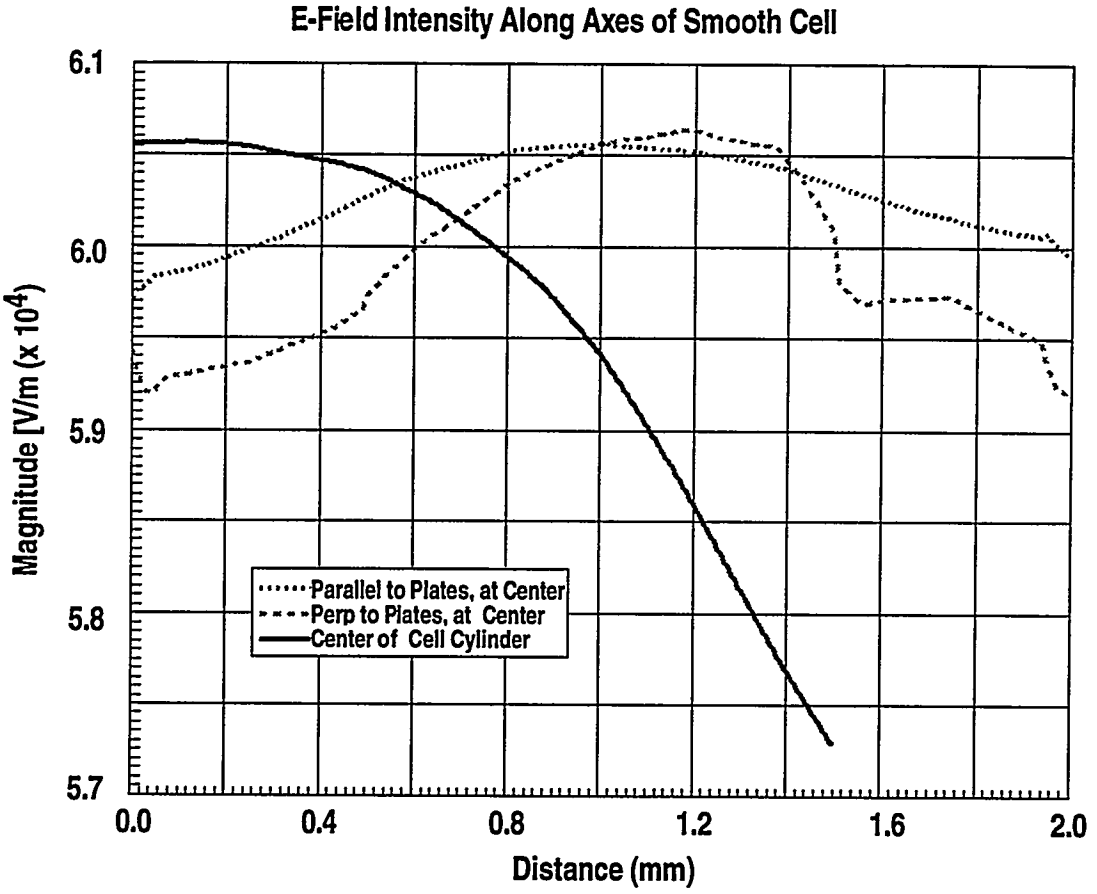

Fig. 5–6. Electric field inside of smooth bore sapphire cell.

Numbers have also been generated on a similar sapphire cell with a ring inserted in the center. This is similar to the inverted torus used in LANL beta-layering experiments. The average attenuation of the electric field is comparable to that in the smooth cell but local variations are more prominent due to edge effects of the insert.

During the coming year we plan on improving the current model and also using electric field power densities to predict the layer shapes in a sapphire cell.

For further information, please contact Dr. J. Sater (WJSA).

5.1.2. IR HEATING

Current cryogenic target designs require a uniform cryogenic deuterium-tritium (DT) fuel layer. There is also a need for nontritiated cryogenic targets, HD or D_2. However, without the beta-decay heat generation no spontaneous solid redistribution will occur. We have been

investigating the possible use of infra-red (IR) radiation to redistribute solid D_2 or HD inside suitable plastic shells by pumping the collision induced vibration-rotation bands characteristic of the hydrogens [Ref. 5-6].

Figure 5-7 is a sketch of the experimental layout. The sample cell consists of a 4 mm sapphire cube containing a 3 mm o.d. cylindrical clear bore hole sealed at each end with a sapphire window. A fill tube is glued into a 381 μm o.d. hole to allow liquid grade HD or D_2 into the cell. The cell is thermally and mechanically attached to the cold tip of a helium flow cryostat. Windows on the vacuum canister and radiation shield permit both visible and IR optical access to the sample cell. The light makes a single pass through the sample cell with either an F-center laser or a black body source used to produce the IR light. We collected and analyzed shadowgraph images of the hydrogen ice profile versus time to determine a redistribution time constant.

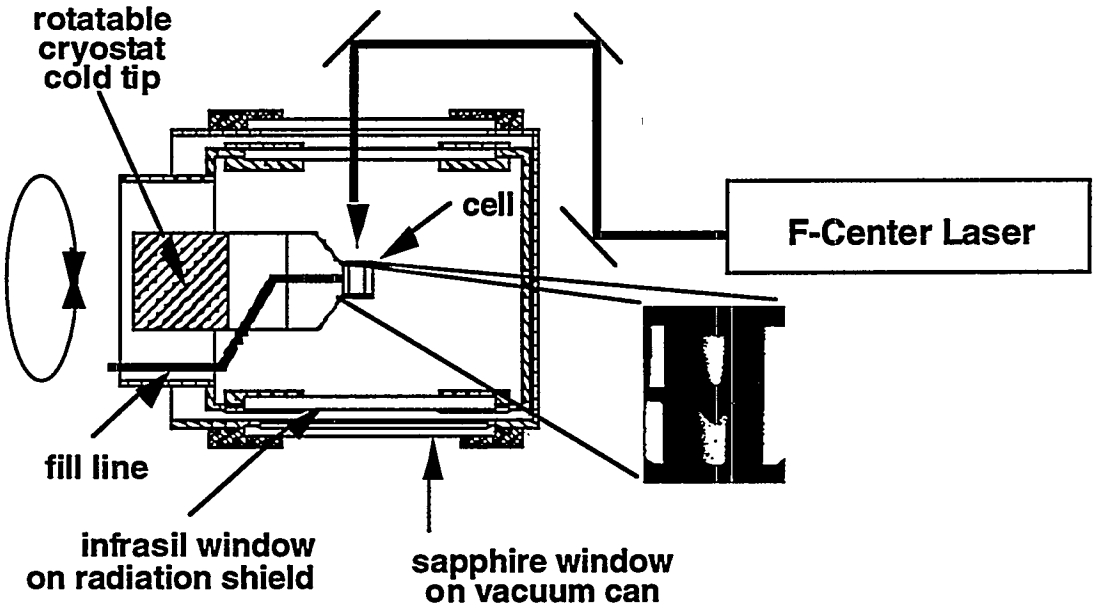

Fig. 5–7. Sketch of experiment layout.

We have observed solid D_2 and HD redistribute inside the sapphire cell. The types of measurements using the laser and an IR lamp were analogous. However, with the laser more power was put into the solid at a significantly narrower bandwidth than with the IR lamp filtered down to 3 mW using a 2.8–3.8 μm bandpass filter. The laser was tuned to wavelengths on and off absorption lines for both D_2 and HD to compare distribution rates. In addition, the laser output power was varied in the range of 2 to 22 mW to examine the effect

of power level on the distribution rate. Figure 5-8 contains images showing the movement of the D_2 solid-vapor interface downward starting at time t = 0, when the laser was turned on. In this case, the laser was set to a wavelength of 3.16 μm, and the experiment was performed at a temperature of 17 K. As can be seen in the images and was typical of all the experiments, with time the top and bottom layer thicknesses became approximately equal.

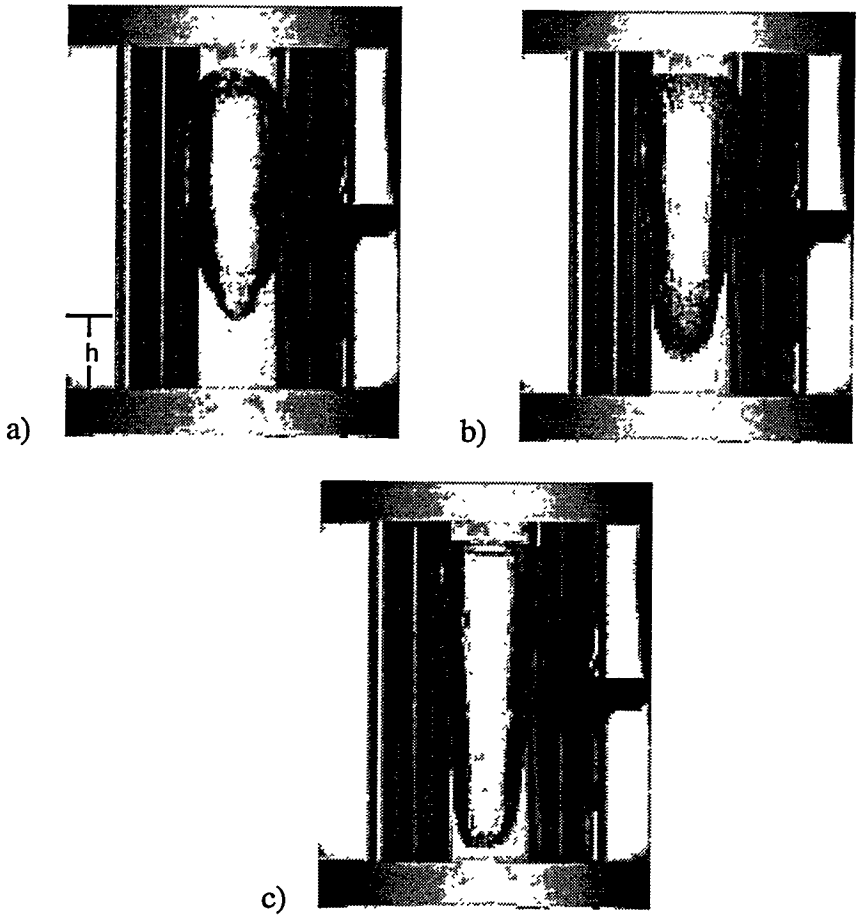

a) t = 0 **b) t = 10 min.** **c) t = 51 min.**

Fig. 5–8. CCD images showing the time development of the D_2 mass redistribution using the F-center laser. "h" denotes the height of the solid-vapor interface above the bottom window.

Figure 5-9 contains example data sets showing the relative height measurements versus time for these experiments. Since the experiments do not start with identical amounts of solid, a reduced height is calculated, which is the distance of the solid-vapor interface from the bottom window scaled to 1 at t = 0 and 0 at the end of the experiment. One can see from the data that the redistribution time using the laser is significantly less than with the IR lamp.

Also, since there is stronger absorption in HD than D_2, the redistribution times seen in HD are noticeably less than that for D_2. An exponential fit to the data from these HD and D_2 experiments using the laser yields time constants of about 3.8 and 29 min., respectively. In comparison, the time constant for the experiment run using the IR lamp and filter was 128 min (~2.1 hr), a larger time constant by about an order of magnitude. For reference, running the experiment with HD and the 2.8–3.8 μm filter yielded a time constant of 24.3 hr. In this case the HD absorption band is outside the bandwidth of this filter.

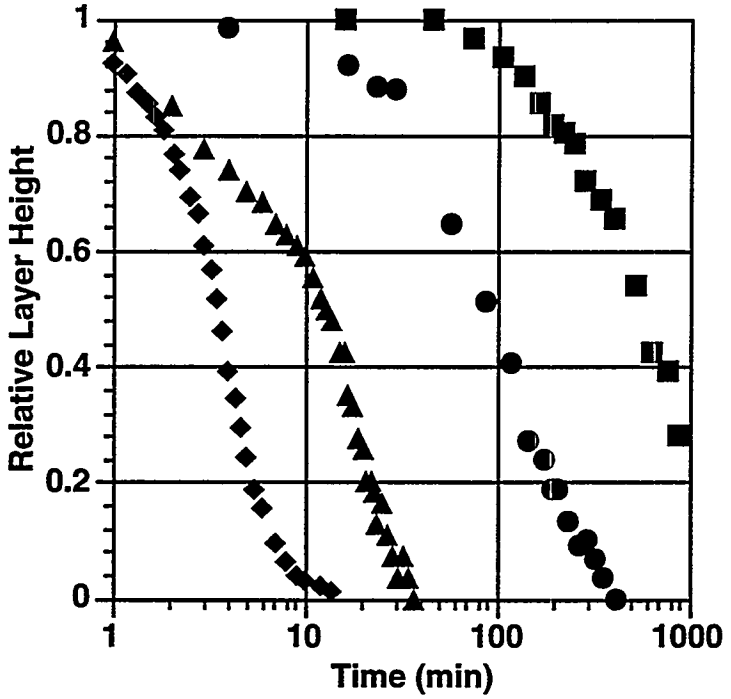

Fig. 5–9. Plot showing relative redistribution for D_2 (H) and HD (F) with the laser, D_2 with the IR lamp (J), and HD with the IR lamp bandpass filtered off its absorption band (B).

Figure 5-10 shows the measured and calculated redistribution time constants versus incident flux for D_2 and HD for the laser experiments. The time constant τ is calculated assuming the HD or D_2 is a weakly absorbing medium; thus, $\tau = l\,\rho/Q$, where l is the latent heat, ρ is the density, and Q is the average heat generation rate from IR absorption.

The IR heating experiment was modeled using COSMOS. Figure 5-11 shows a sample calculation. The cell was modeled as a sapphire cylinder in contact through the cylinder wall with a heat sink at a relative temperature of 0 K. It was assumed that all heat flow went through the heat sink. The IR heating rate was based on the absorption of the light as it

passed through the ice. Heating was assumed to be uniform over volume element regions 100 μm thick with a heating volume assigned based on the light intensity at the center of each 100 μm thick region. For this calculation the incoming light intensity was 100 mW/cm^2, and the D_2 ice absorption value was 3 cm. Thus, in a 100 μm layer, the intensity of light and, hence, the heating vary by 3%. The flat D_2 layer at the cell top is due to uniform heating from the relatively flat incident IR wavefront. The thin D_2 layer on the top and bottom windows has roughly the same thickness. The curved bottom section of D_2 is due to the IR light passing through the D_2 layer near the sides of the cell which gets highly attenuated at the bottom of the cell, resulting in a lower heat generation rate in the bottom corners. With a lower heating rate, a thicker layer can be established while maintaining the inner isothermal surface.

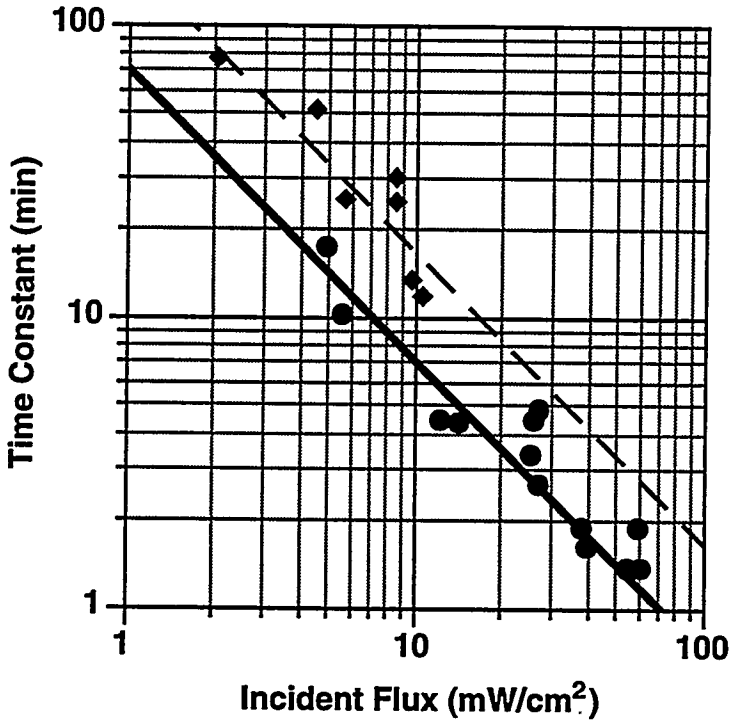

Fig. 5–10. Plot showing the redistribution time constants for HD (J) and D_2 (F) versus incident flux. The solid and dashed lines are calculated fits to the HD and D_2 data, respectively.

5.1.3. THERMAL GRADIENT LAYERING IN CRYOGENIC LIQUID H_2-D_2

We have developed a nonlinear, analytical model to calculate the flow field and forces in a thick liquid layer ICF target. The model calculates the thermal conditions for which the net

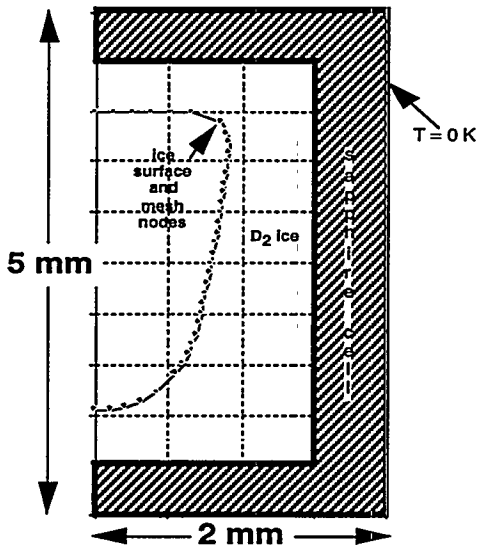

Fig. 5–11. Sketch of half a cylindrical sapphire cell showing calculated ice surface. IR radiation is incident from the top.

force on a spherically-symmetric layer vanishes (i.e., for which all forces balance in steady state). The model works for pure D_2 or H_2-D_2 and for the steady symmetric flows of interest. The model successfully predicts the temperature gradients and heat transfer rates needed to support liquid layers in Omega-Upgrade and NIF capsules, with and without the presence of foam.

For further information, please contact Dr. D. Bittner (WJSA).

The internal flows in these capsules are driven by surface-tension-gradient forces on the liquid surface at the vapor-liquid interface (the bubble). The force per unit area is proportional to $(d\sigma/dT)\ \Delta T_v$, where the first term is the surface-tension-gradient term (derived from experimental data) and the second is the temperature difference across the vapor bubble. The geometry is given in Fig. 5-12.

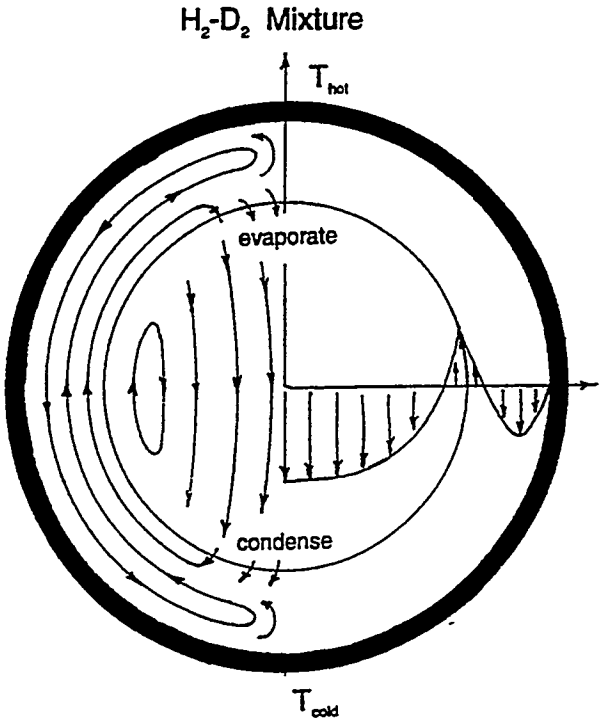

Fig. 5–12. The geometry and flowfield of H_2-D_2 liquid layering using thermal gradients.

In the model, we satisfy the equations of conservation of mass, momentum, and energy with analytical functions for the velocity profiles in the vapor and liquid phases, parameterized by ΔT_V across the vapor bubble. Using an integral form of the momentum equation, we generate an algebraic equation for the net force on the liquid layer as a function of ΔT_V and then solve for the ΔT_V which balances all the forces.

This modeling was undertaken because the previous linearized models are only valid below Reynolds numbers of unity, while the thick liquid layers of interest to Omega-Upgrade and NIF (80–100 μm) have Reynolds numbers in the range of 20–60.

We expended a significant effort trying to calculate the surface-tension-gradient force from first principles, but were not able to get it right. The surface-tension-gradient in multi-component mixtures like H_2-D_2 or D-T must be positive for a positive temperature gradient (i.e., the liquid is pulled upward). Yet calculating $d\sigma/dT$ as a property of the fluid yields a number that is always negative, even accounting carefully for the different liquid and vapor compositions as a function of temperature. Therefore, the surface-tension-gradient is not a local property of the fluid, but is dependent on the diffusion and evaporation/condensation

rates. Until this is unraveled correctly, we consider $d\sigma/dT$ an unknown function of temperature that we derive from previous thin layer experiments done by Kim et al. at the University of Illinois.

We show here results of the model for five cases, all for nominal 50:50 mixtures of H_2-D_2 at 20 K. See Table 5–1 for the dimensions of the capsules, their liquid layer thicknesses, and the foam thicknesses. When foam is used, the idea is to immobilize the majority of the liquid by having a foam contain the outer 60 μm or so of the liquid layer, leaving only a thinner 20 μm layer of free liquid to be supported. Presumably, this can be done with smaller applied temperature gradients. In Table 5–1, Case 1 is the small glass shell containing a thin 6.85 μm layer of H_2-D_2 from which we obtained the $d\sigma/dT$ data. Cases 2 and 3 are nominal Omega-Upgrade polymer capsules of 922 μm diameter with 78 μm liquid layers, with and without foam. Cases 4 and 5 are for larger (2.2 mm) NIF capsules with 80 μm liquid layers, with and without foam.

In calculating the compositions of the vapor and liquid phases in these capsules as a function of temperature, we noted quite different behaviors for different fill conditions. For example, as the temperature is raised from 16 to 30 K in the small capsule with a thin layer,

TABLE 5–1
INPUT PARAMETERS FOR FIVE CASES CALCULATED FOR H_2-D_2 CAPSULES AT 20 K

Parameter	Case 1 "Kim H_2-D_2"	Case 2 "Omega Upgrade"	Case 3 "Omega-U Foam"	Case 4 "NIF"	Case 5 "NIF Foam"
Capsule	Glass	Polymer	Polymer	Polymer	Polymer
Outer radius, μm	300	461	461	1110	1110
Shell thickness, μm	6.25	6	6	160	160
Inner radius, μm	293.75	455	455	950	950
H_2-D_2 Filled Foam					
Outer radius, μm			455		950
Foam thickness, μm	0	0	58	0	60
Inner radius, μm			397		890
Free H_2-D_2 Liquid					
Outer radius, μm	293.75	455	397	950	890
Layer thickness, μm	6.85	78	20	80	20
Inner radius, μm	286.90	377	377	870	870

the layer thins, as evaporation is a larger effect than the swelling of the liquid. For large capsules and thick layers, the opposite is true, and layers thicken with temperature. In all cases, when the forces are in balance on a steady-state liquid layer, the layer is about equally supported by the (upward) surface-tension-gradient force at the interface and the (upward) viscous shear force on the downward-flowing liquid at the wall.

The temperature differences across the vapor bubble needed to drive the dynamics of layering are very small, while the corresponding temperature differences which must be applied across the shell are quite large. For example, in an Omega-Upgrade capsule, the temperature drop across the entire capsule is 0.12 K; across just the polymer shell it is 0.022 K; across a liquid layer it is 0.038 K; and across the vapor bubble it is just 64 μK.

We summarize the findings of the study in terms of the operating characteristics that an experimentalist would use in thermal layering. We would seek to apply a given temperature difference across the capsule and control the heat transfer rate through the capsule. The calculated values are plotted in Fig. 5–13 for the Omega-Upgrade capsules and Fig. 5–14 for the NIF capsules.

For further information, please contact Dr. M. Monsler (WJSA).

5.1.4. THERMAL PROFILE ANALYSIS

We have analyzed temperature profiles in several experimental scenarios. Figure 5–15 shows the boundary conditions for a NIF scale hohlraum at 0 K with a D-T-filled NIF scale shell. Calculations show that there is nearly a 1 mK asymmetry in the inner ice temperature due to the isothermal hohlraum which is larger than the ~0.8 mK drop across the D-T ice layer. In a second geometry, Fig. 5-16, a spherical isothermal boundary at 3.75 mm with a 100 μm uniform D_2 layer inside a NIF scale shell is used. Here the shell and D_2 are heated by IR light with a 10% asymmetric IR intensity profile, $I = I_0 [1 + 0.1 \sin(\phi)]$, where I_0 is fixed to generate the same average heat generation rate in D_2 as D-T. Calculations yield a 6 mK temperature asymmetry on the inner solid D_2 layer. There is also about a 0.5 K increase in the shell temperature. Therefore, to produce a heat generation rate ten times the D-T value, there would be a ~6 K temperature drop across the conduction gas. Finally, using the boundary conditions shown in Fig. 5–15, calculations were performed to determine the temperature asymmetry for a 100 μm thick D_2 layer with the 10% asymmetric IR intensity

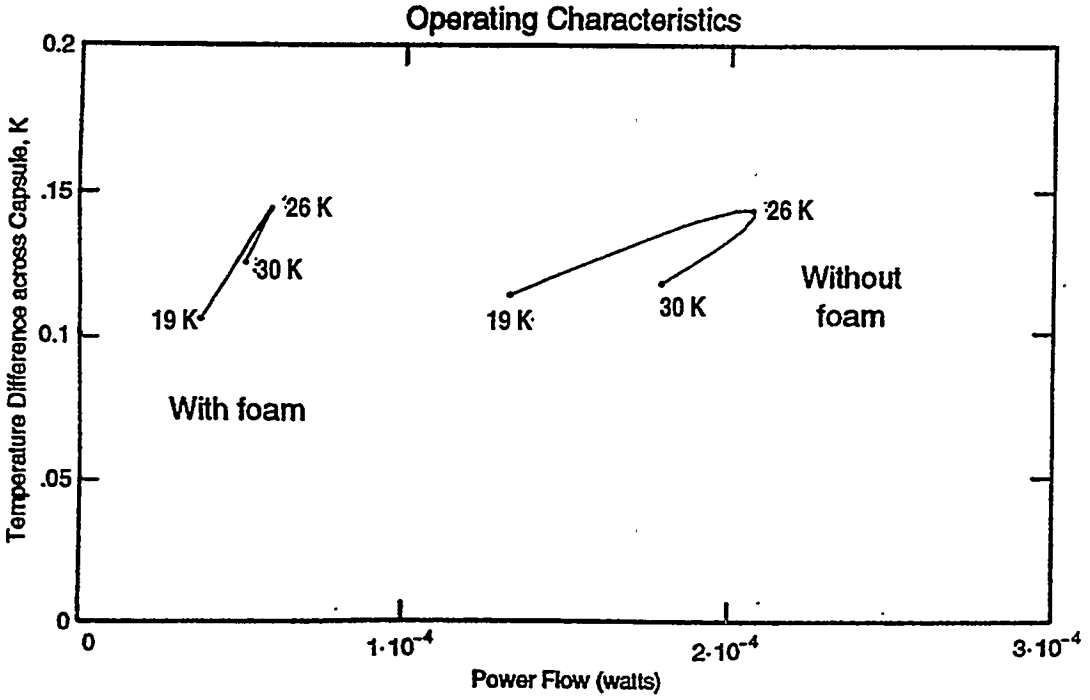

Fig. 5–13. The operating characteristics for Omega-Upgrade capsules, with and without foam (Cases 2 and 3).

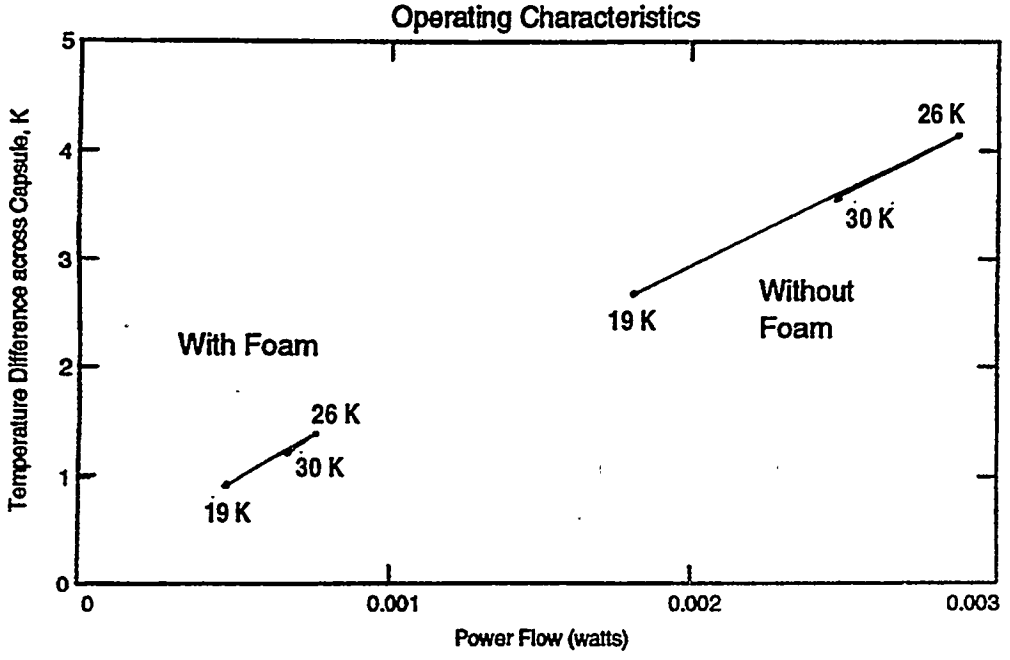

Fig. 5–14. The operating characteristics for NIF capsules with and without foam (Cases 4 and 5).

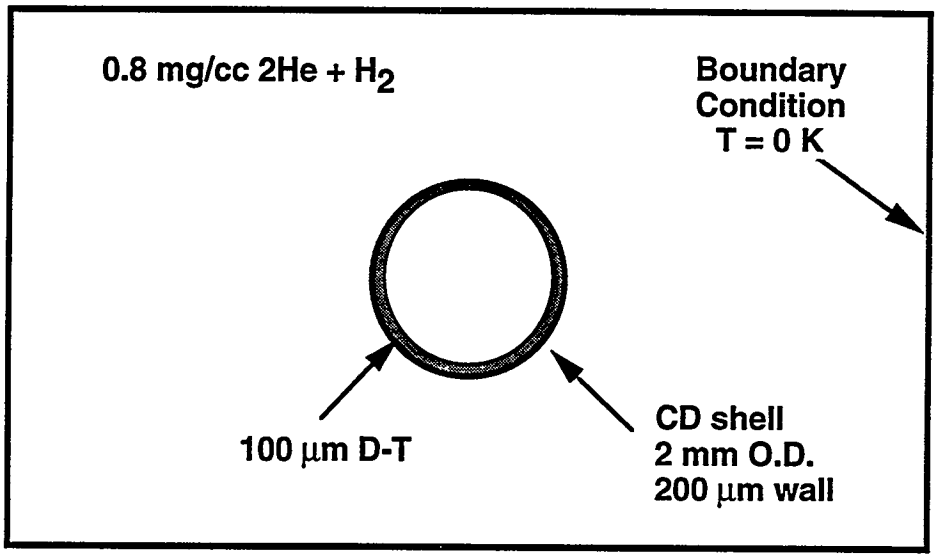

Fig. 5–15. Schematic diagram for a NIF scale hohlraum (9.5 mm x 5.5 mm o.d.).

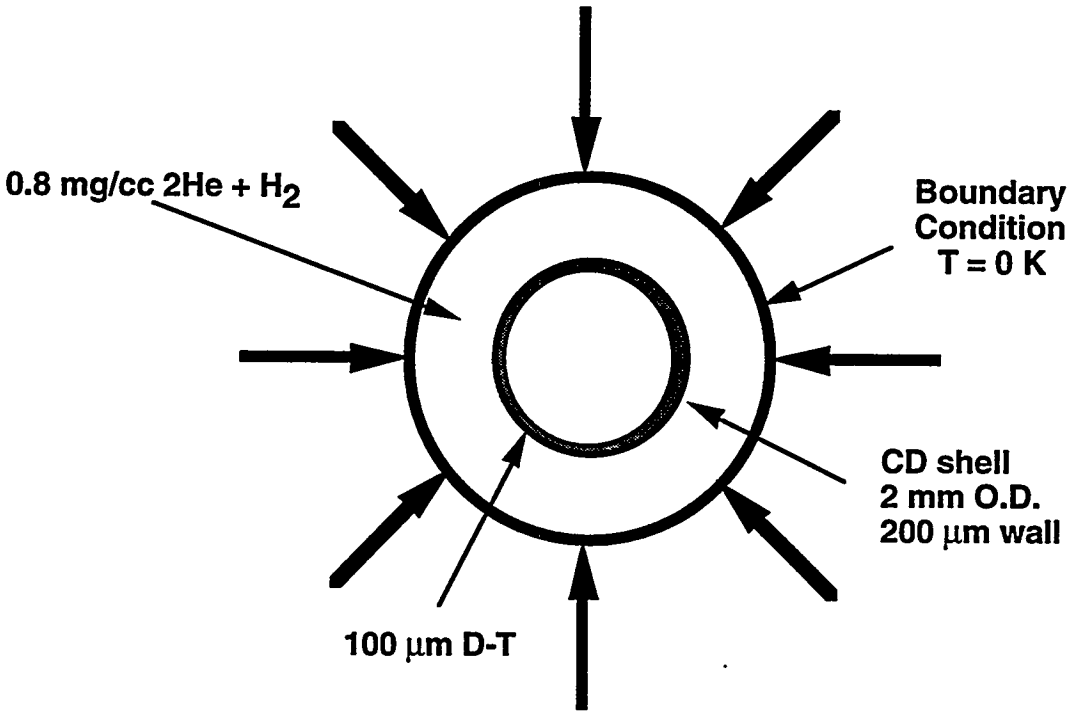

Fig. 5–16. Schematic diagram showing a spherical isothermal boundary at 3.75 mm with a uniform D_2 layer inside a NIF scale shell.

profile as in the previous calculation. Results showed that the temperature asymmetry is roughly the same as that produced by the isothermal hohlraum. These values strongly

depend on the absorption in the plastic for which we use the conservative estimate of 16% absorption across the shell wall.

A series of models was created to examine the effect of changes in the hohlraum geometry on the isotherms within a spherical beta-layered target. Dimensions and aspect ratios were varied, and the resultant temperature variations were calculated. For a first set of runs, the cylinder diameter was set equal to the cylinder height (D = H) and again the temperature variations on the inner surface of a 100 μm layer inside a 2 mm diameter capsule are studied as a function of cylinder radius. Calculations were performed for three different diameters: 10, 20, and 40 mm. The corresponding temperature variations were about 50, 20, and 10 μK, respectively. By scaling to larger hohlraums, the temperature variations decreased as one would expect. However, these temperature variations can also be reduced by slightly changing the aspect ratio of the hohlraum. In a cylinder, D = H, a centered capsule is not equidistant from the wall everywhere, with the distance uniform and closest at the midplane of the capsule. Therefore, for a capsule placed at the cylinder center, the midplane of the capsule will be slightly cooler than the poles. Calculations were performed for a capsule in a cylinder with H = 10 mm and D = 11 mm. The temperature variation for the this case is about 10 μK, while, as noted above, the temperature variation for D = H = 10 mm case is about 50 μK. Using an isothermal shroud with D = 1.1 H allows a 11 mm diameter shroud to give the same ice uniformity as that for a 40 mm diameter shroud with D = H. By using a hohlraum with a diameter slightly larger than its height, the thermal variations on the ice surface should be reduced.

For further information, please contact Dr. D. Bittner (WJSA).

5.2. BETA-LAYERING EXPERIMENTS AT LANL

Solid D-T layering experiments were performed in both hemispherical and toroidal geometries.

5.2.1. 1 MILLIMETER TOROIDAL GEOMETRY

Solid D-T layering experiments have been performed in 1 mm toroidal geometry in order to provide data relevant to the requirements of the Omega Upgrade system at the University of Rochester Laboratory for Laser Energetics. This cell design includes a 1 mm internal diameter toroidal bore and low thermal conductivity windows to prevent solid D-T buildup

on the windows with resulting distortion of the layer image. In addition, the front window was heated with an integral thin film heater to ensure a solid-free optical path if necessary. Images of the empty 1 mm torus and a 100 μm D-T solid layer inside the torus are shown in Fig. 5–17. The effects of internal light scattering within the cell and "light piping" by scattering within the D–T layer of this cell design can be seen in these two images. As will be shown later, these side effects have been eliminated in the current 2 mm torus cell design.

Empty 1 mm Toroid Cell and 100 μm D-T Layer inside Torus

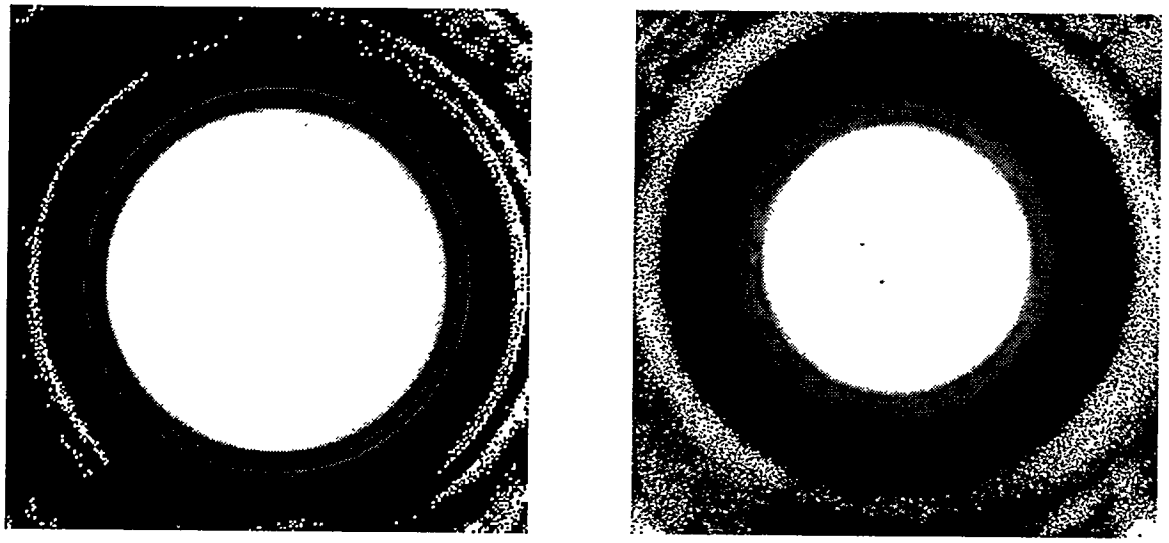

Empty 1 mm Torus

D-T Layer Inside 1 mm Torus
290 min after 19-15 K transition

Fig. 5-17. Images of the empty 1 mm toroidal D-T cell and a D-T solid layer inside the torus 290 minutes after a 19–15 K temperature transition. The light rings seen in the empty torus are due to internal reflections from the cell wall and windows, creating problems for the accurate determination of the layer edge. Notice the complex structure in the image of the D-T layer, due to light scattering and light piping, which makes the determination of surface roughness non-trivial.

The image of the D-T layer shows that light piping, and light scattering within the cell produce an image with many light and dark features that makes edge detection tricky at best. However, some of this data has been analyzed for equilibrated and temperature stepped surface roughness, and the results are shown in Figs. 5–18 and 5–19. In Fig. 5–18 we can see that this 110 μm toroid layer has a slightly better surface of about 1.2 μm than was observed in the previous re-entrant type cell. At modes above P10, the surface roughness drops below

1 μm for the torus. Later data have shown that this geometry can produce D-T layers with surface roughness below 1 μm rms.

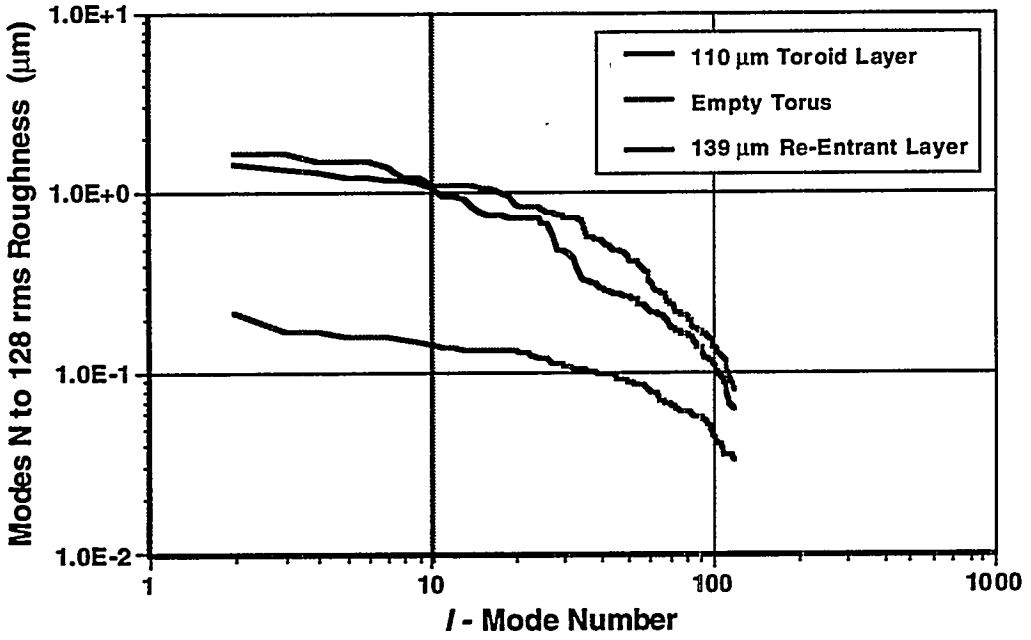

Fig. 5-18. Comparison of the mode indexed (mode N to 256) surface roughness for D-T solid layers inside the 1 mm torus and the 2 mm re-entrant D-T cells, along with the empty torus. As expected, due to length scaling, the toroid layer is slightly smoother than the re-entrant layer. Additionally the re-entrant layer was viewed through D-T solid on the front window, producing distortions in the solid layer image.

Figure 5–19 shows some of the results of several temperature stepping experiments that were performed to study the effect of abrupt temperature increments and decrements on the layer surface roughness. The graph shows an initial improvement in surface roughness followed by a slow degradation in the D-T layer as helium builds up and impacts the layer surface. This effect has been observed in virtually all D-T solid layers, and is worse for thicker layers (degradation occurs more rapidly). In all cases of temperature incrementing or decrementing, the effects of temperature stepping seems to be transient on a time scale of minutes to tens of minutes.

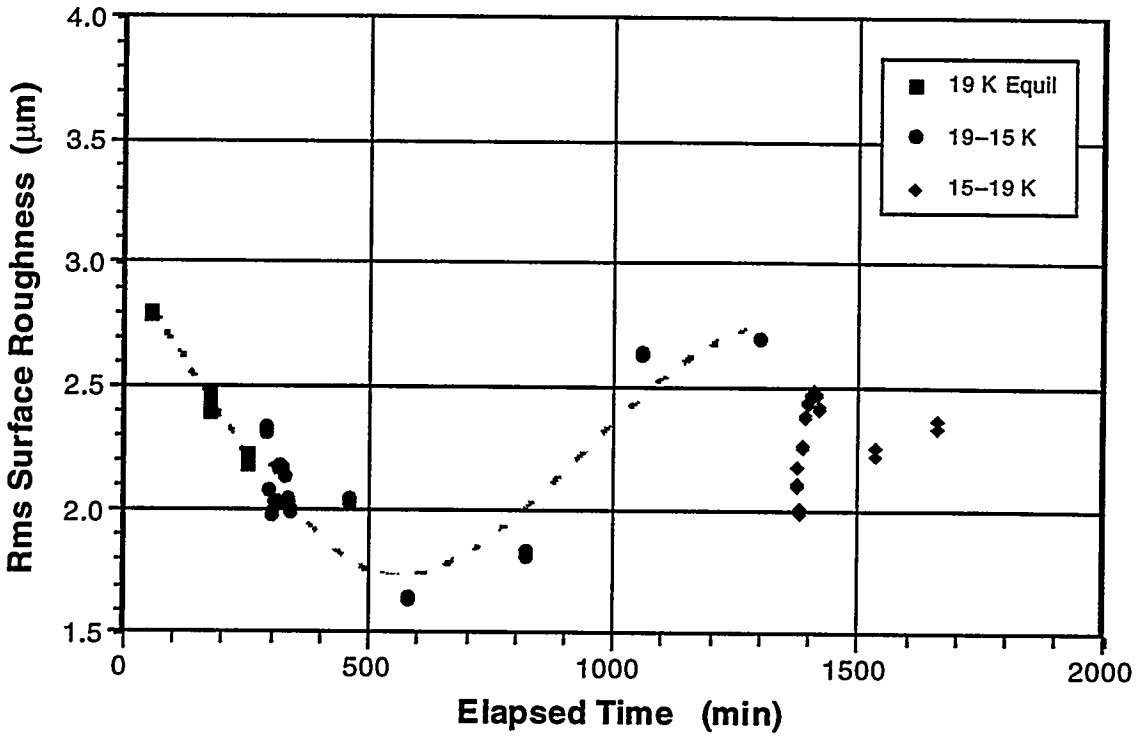

Fig. 5–19. Data from the 1 mm torus temperature stepping experiments, in which an equilibrated 19 K D-T layer was subjected to a 4 K temperature decrement, followed by a 4 K temperature increment. Surface roughness effects due to temperature transitions are transient on the order of minutes to tens of minutes, and there is a long term roughening or layer degradation due to the helium buildup in the solid layer which impacts the surface on a several hundred minute time scale.

5.2.2. 2 mm HEMISPHERICAL GEOMETRY

The 2 mm hemi was designed to permit studies of D-T solid layering in spherical geometry without the imaging distortions that are inherent in full spherical cells. This cell is NIF (National Ignition Facility) size and includes a low conductivity front window to prevent solid D-T buildup obscuring the optical path and distorting the image of the layer edge of interest. This window was only partially successful in preventing solid from distorting the layer image, since a small amount of solid did wrap onto the window in the region of the layer edge. Additionally, the cell contained low mode defects which imprinted on the layer, making the measurement of layer surface roughness very difficult and inconclusive. Figure 5–20 is a series of images of several layers observed in the 2 mm hemi at various temperatures. The possible distorting effect of D-T solid wrapping around the window near the layer edge can be in most of these images. Figure 5–21 shows the results of the analysis of the 18.5 K layer at times of 150, 240, and 285 minutes into the run. This graph clearly

shows the effect of cell structural imprinting of at least modes P2 and P3 on the layer surface itself. At modes above P3, imprinting becomes less apparent and the surface roughness for this layer is close to 1.6 μm rms.

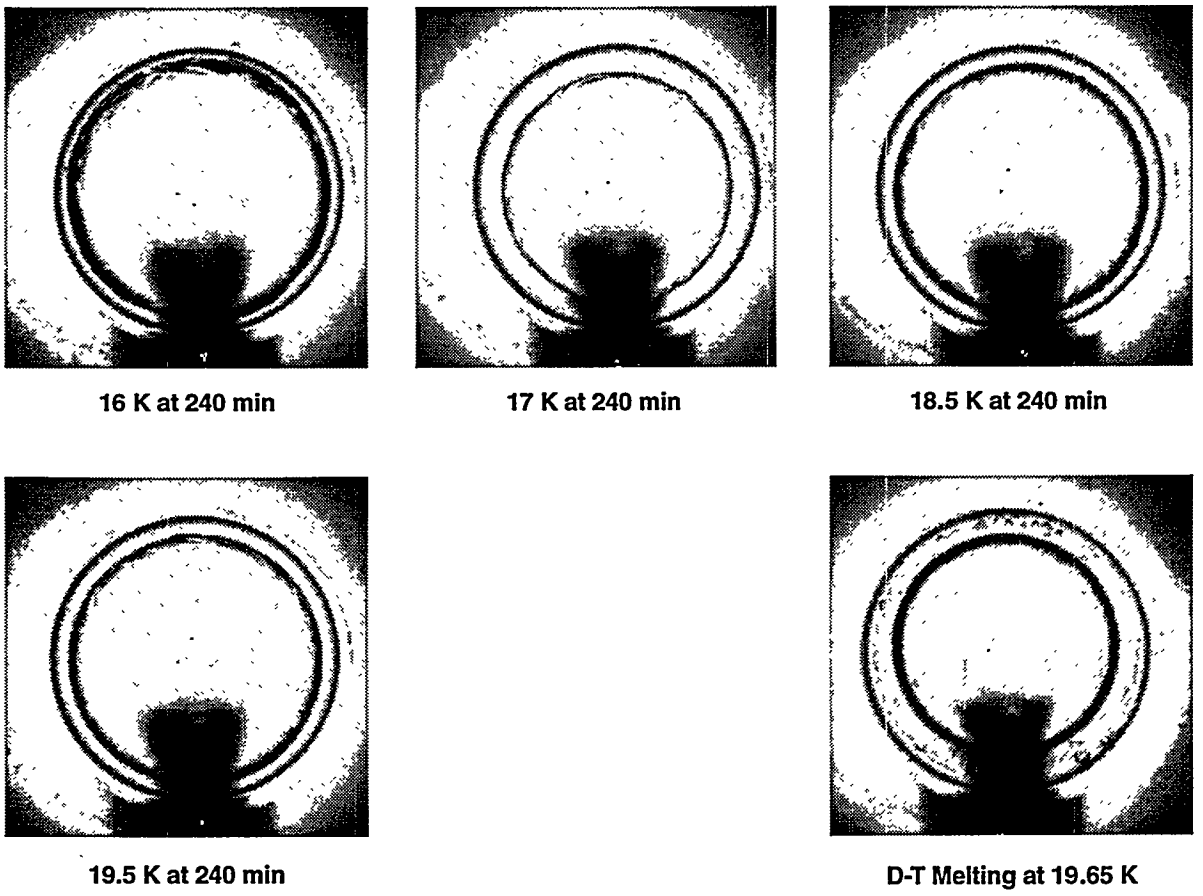

Fig. 5–20. A series of images of D-T solid layers inside the 2 mm hemi at several temperatures and thickness. The D-T solid is seen wrapping onto the window near the layer edge, possibly creating distortions in the layer image, and is at least creating ambiguous and inconclusive data.

5.2.3. 2 MILLIMETER TOROIDAL GEOMETRY

The lessons learned with the 1 mm torus and 2 mm hemi experiments were applied to the design of the 2 mm torus, which included an integral axial heating element to permit studies of layer smoothing with external heating mechanisms. This cell has virtually eliminated the light piping and light scattering effects observed in the 1 mm torus, and prevents D-T solid wrapping onto the front window in the region where this solid could distort the image of the

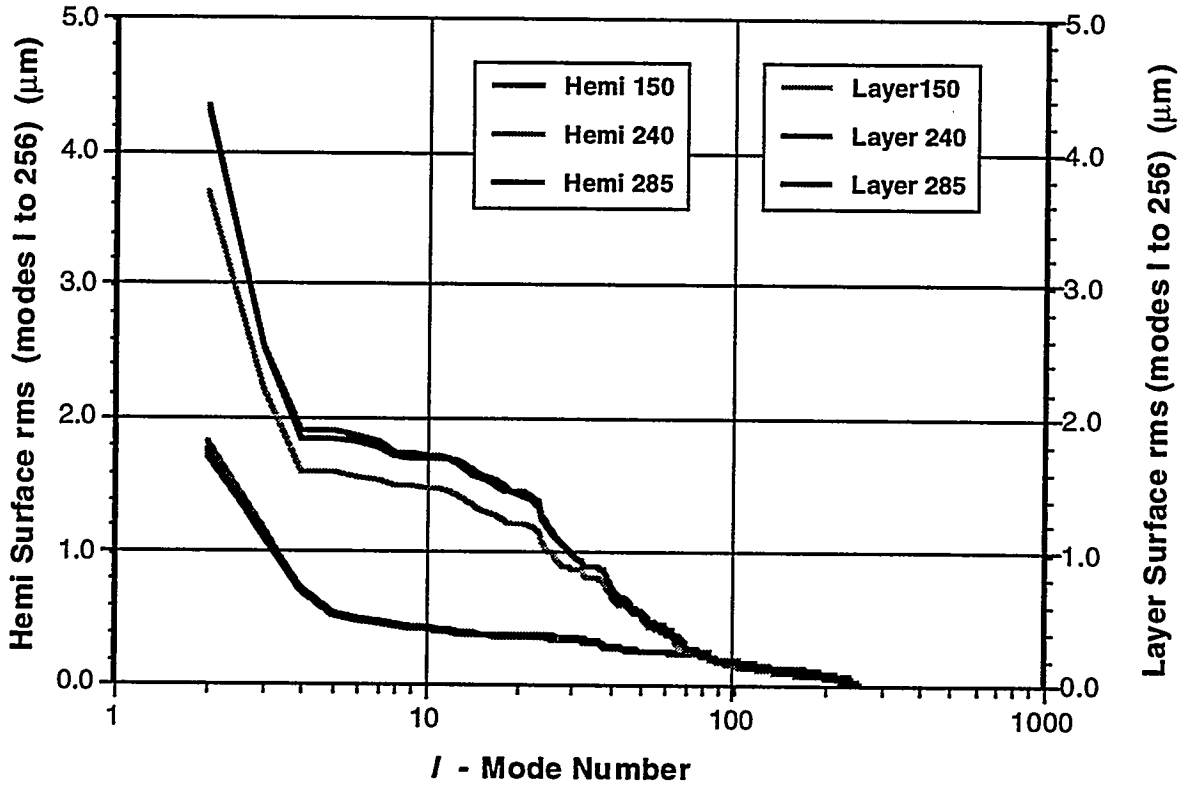

Fig. 5–21. Mode indexed surface roughness for a D-T solid layer inside the 2 mm hemi at 18.5 K; at 150 min, 240 min, and 285 min into the equilibration. The large P2 and P3 l modes observed in the hemi surface can be seen as imprinting on the D-T solid layer, producing a rougher surface than may actually exist. The large P2 is the likely result of off-axis misalignment of the cell and optical train, which can now be nulled with pitch and yaw adjustment of the optical system. The P3 is likely the result of the machining process.

layer edge of interest, as seen in the 2 mm hemi. Additionally, a new illumination system allows precise focusing of the illumination beam so that there is very little internal light scattering and only the layer edge region of interest is illuminated.

Figure 5–22 shows images of the empty torus and a heater smoothed 37 μm D-T solid layer inside the torus. Comparison of these images with Fig. 5–17 clearly shows a significant reduction in internal light scattering and light piping over the 1 mm torus. In fact both effects have been reduced to insignificance by the design of the 2 mm torus, permitting a superb and unprecedented view of the layer surface of interest. This cell also permitted, for the first time, studies of the surface roughness inherent in native beta-layering (no external heating), as well as surface roughness attainable using varying levels of external heating.

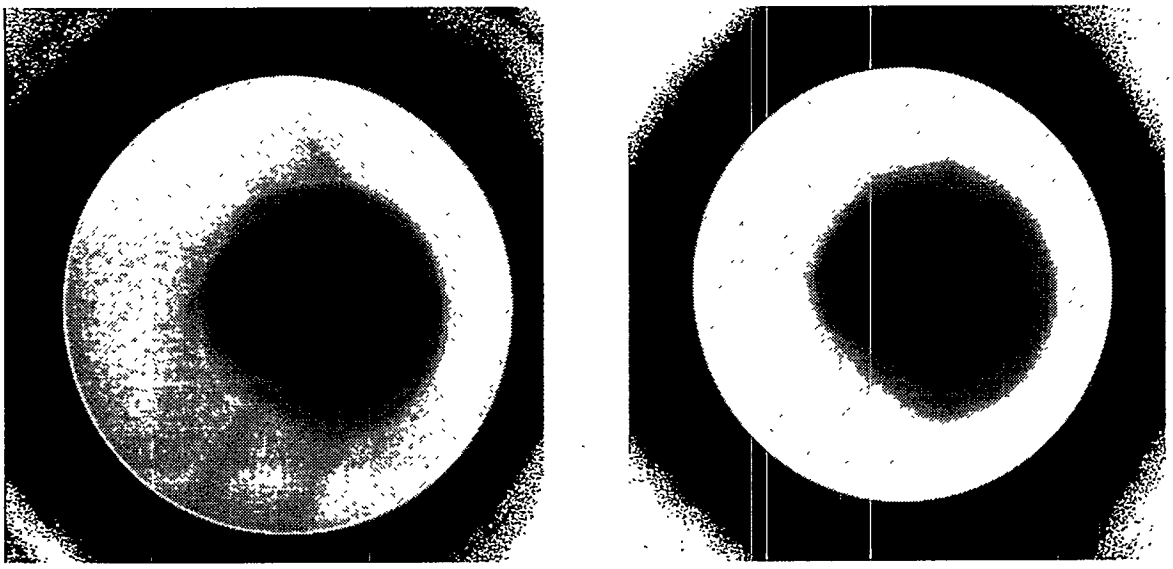

Empty 2 mm Torus with Central Heater

37 μm D-T Solid Layer inside 2 mm Torus at 1125 μW Heater Power

Fig. 5-22. Images of the empty 2 mm torus and a 37 μm heat assisted D-T solid layer inside the torus. Comparison of these images with those of Fig. 5–17, clearly shows the significant improvement in image quality (D-T layer edge view) that is obtained with the design modifications implemented in the 2 mm torus. Internal light scattering and light piping have been virtually eliminated with this new cell and focused illumination system, significantly improving edge detection accuracy and surface roughness measurement resolution.

Figure 5–23 shows data comparing surface roughness evolution for two 19.0 K layers at 80 and 130 μm thickness, and a 19.5 K D-T solid layer at 150 μm thickness. This graph appears to show that layers equilibrated at the same temperature are rougher and degrade faster (^{3}He buildup) when thicker, and that D-T solid layers are smoother and degrade more slowly when equilibrated at temperatures nearer the triple point. Figure 5–24 is a comparison of mode indexed [Σ (mode N to 256)] surface roughness for native and heat enhanced beta-layers, and again shows the improvement in surface finish that results from additional heating, no matter what the source. Notice that in all cases shown on this graph, the total surface roughness is below 1 μm rms.

The data shown in Fig. 5–25 track the evolution of a 19.65 K native layer, followed by a 19.65–18 K temperature decrement. These are compared with a layer equilibrated at 19.5 K with heat added at the end of the equilibration. These data show several interesting phenomena, including the apparent fact that the 19.65 K layer was very near the D-T triple point and may have been softening, which limited the attainable surface roughness to only

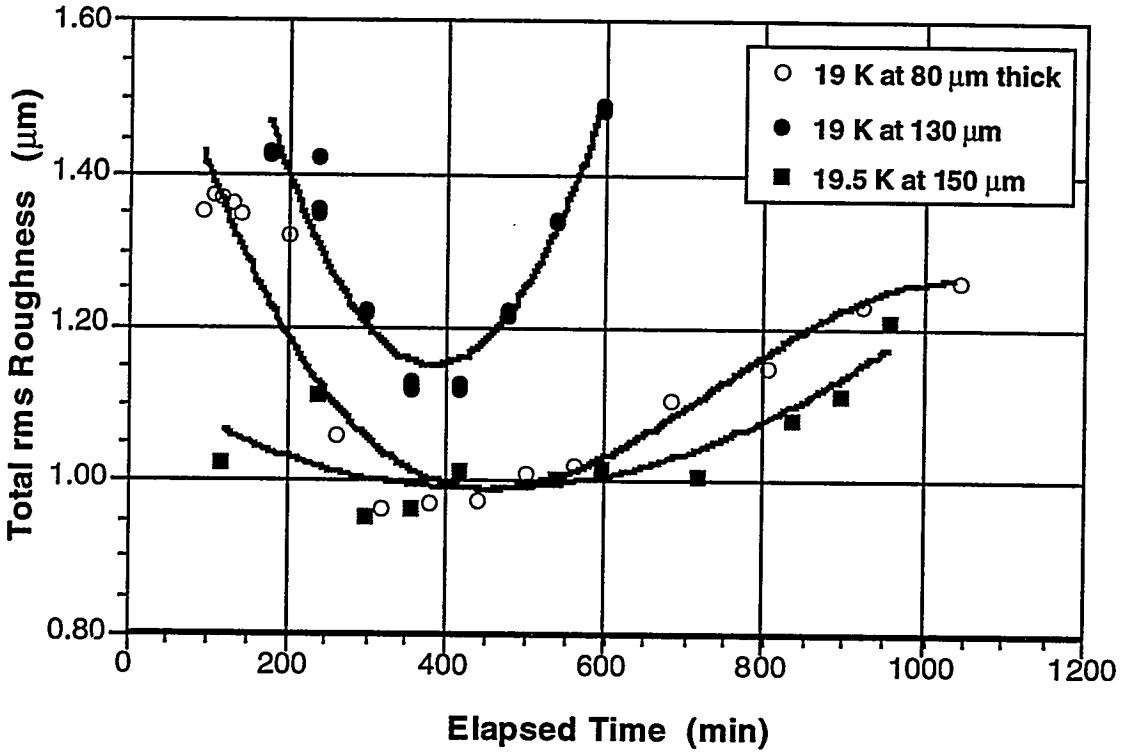

Fig. 5–23. Native beta-layering D-T solid surface roughness evolution inside the 2 mm torus at 19.0 and 19.5 K equilibration temperatures. This graph shows the interesting results that thinner layers become smoother and degrade more slowly than thicker layers (19 K data), and that warmer layers may become smoother and degrade more slowly than colder layers (19 K and 19.5 K data). This degradation phenomenon is not unexpected when one considers the impact of helium buildup inside the layer and its subsequent impact on the solid surface — it is also expected that the impact is greater with thicker layers.

about 1.35 μm rms. Additionally, the temperature decrement of 1.65 K shows a small transient roughening followed by a significant improvement in surface roughness to less than 1 μm rms. Finally, the 1125 μw heat-assisted solid layer shows that it is possible to produce solid D-T layers with a surface roughness of about 0.25 μm rms, which in this case is near that of the empty cell (0.2 μm).

Much of the data already generated for the current set of 2 mm torus experiments is still being reduced and analyzed, and there are more experiments being planned, but the initial results seem clear. Beta-layering can produce solid D-T layers with surface roughness of less than 1 μm rms, and with external heating can produce solid layers at least as smooth as 0.25 μm rms. Future experiments should confirm what we have observed thus far, as well as define the parameter space to which surface roughness is mapped (time, temperature, cell geometry).

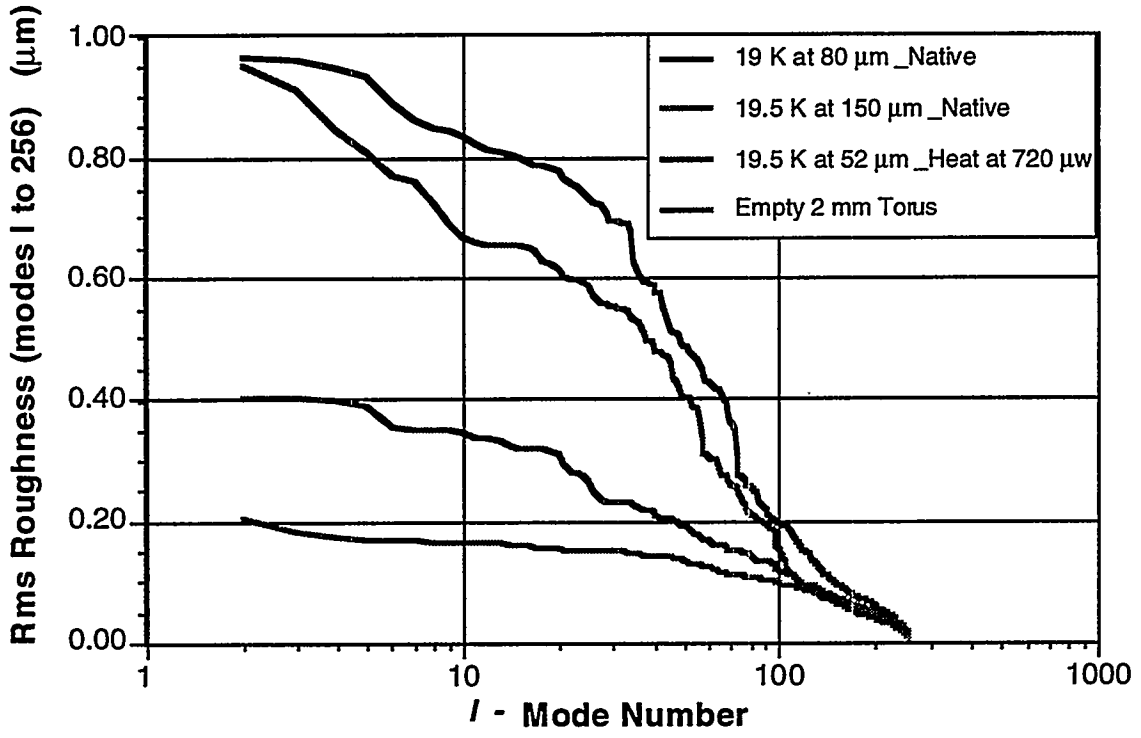

Fig. 5–24. A comparison of mode indexed surface roughness for native, and heat-assisted beta-layered D-T solid inside the 2 mm torus. This graph seems to show that the competition between thickness and temperature mechanisms (19 K and 80 μm vs. 19.5 K and 150 μm is close only at very low modes, and that warmer layers (internal or external heating) do in fact produce smoother D-T solid surfaces.

For further information, please contact J. Sheliak (GA).

5.3. FOAM SHELL DEVELOPMENT

This task is a joint task with LLNL. Contributors include George Overturf III, Stephan Letts, Gerry Wilemski, and Robert Cook (LLNL); Diana Schroen-Carey, Michael McClellan (WJSA); Stephen Lambert (STI); and Richard Stephens (GA). This report is by necessity brief and emphasizes the contributions of the contract personnel. For a more complete reporting of the foam shell subtask see the LLNL technical memo, TAT 95-068, entitled *Resorcinol-Formaldehyde Foam Shell Progress Report*, which is expected to be distributed about November 1, 1995.

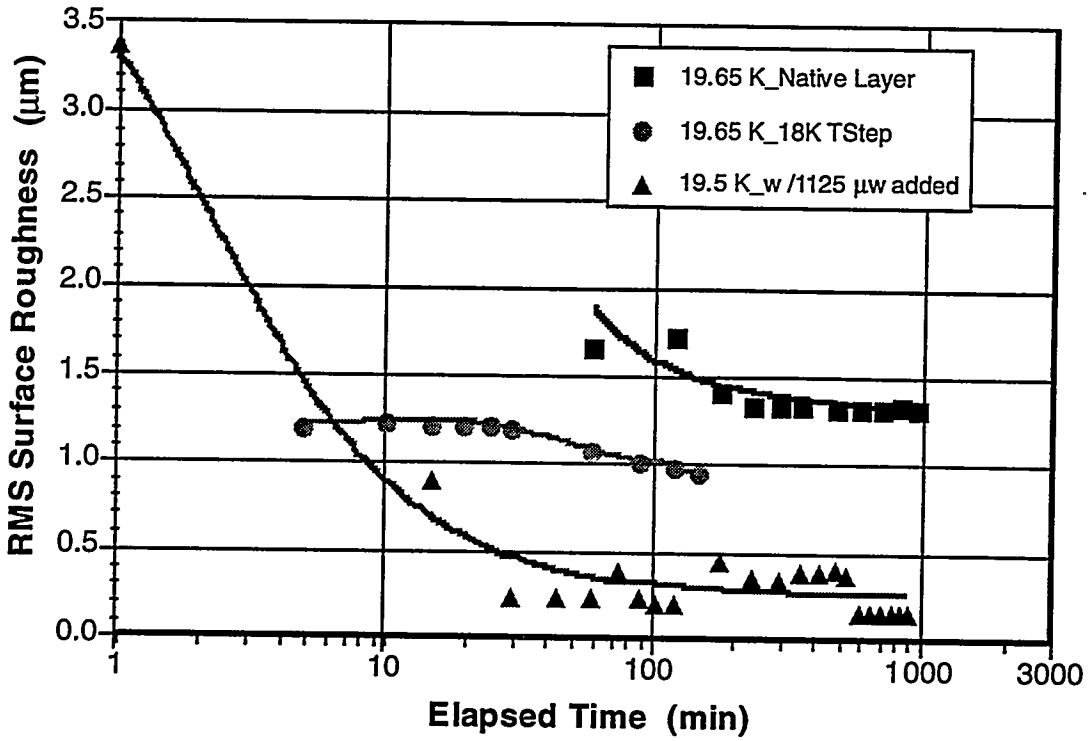

Fig. 5–25. This data shows the results of a 1.65 K temperature decrement on an equilibrated 19.65 K D-T solid layer inside the 2 mm torus, and the impact of 1125 MW of added power to an aged 19.5 K D-T solid layer. The colder 18 K layer shows an unexpected surface roughness improvement , and is the probable result of the 19.65 K layer being very near the D-T triple point and consequently quite soft and perhaps sagging (the 19.65 K layer is much rougher than expected for this reason). The curve for the 1125 MW heat-assisted layering shows the potential of improving an old or very rough solid layer with external heating.

This task had the stated goal "the production of 1 to 2 mm diameter, 50 mg/cc, low Z foam shells with 90 to 100 μm walls and a 5 to 10 μm full density overcoat to be used in cryogenic liquid layering experiments." The anticipated future goal is the production of such shells for the Omega Upgrade facility and NIF facility. There were three subtasks: 1) based upon aerogel technology, develop a microencapsulation process capable of producing an overcoated foam shell; 2) evaluate methacrylate foams, such as those reported by ILE, with emphasis on determining optical properties; 3) calculate limits of foam properties such as cell size and cell wall thickness required to permit optical diagnosis of a 1% P1 uniformity defect.

5.3.1. AEROGEL FOAM SHELL PRODUCTION

An aerogel is a solid formed from a low concentration gel by replacing the liquid with a gas, with little change in volume, so that the solid is highly porous. Resorcinol-formaldehyde

(RF) aerogels had been developed at LLNL by Pekala, et. al. [Ref. 5–7]. The goal was to determine if RF had the potential of producing microencapsulated shells approaching the required size and quality, and if said shells could be overcoated.

RF foam chemistry is a two step process. Resorcinol combines with formaldehyde under basic conditions to form nanometer-sized beads as shown in Fig. 5–26. These beads then link in acidic conditions via methylene ether bridges to form the gel network. In shell production, it is critical that these steps be precisely timed to produce the gel very shortly after the droplet generator creates the microencapsulated preform. After gelling, the shells are exchanged into isopropanol, to remove the exterior and interior phase, and super-critically dried using liquid CO_2.

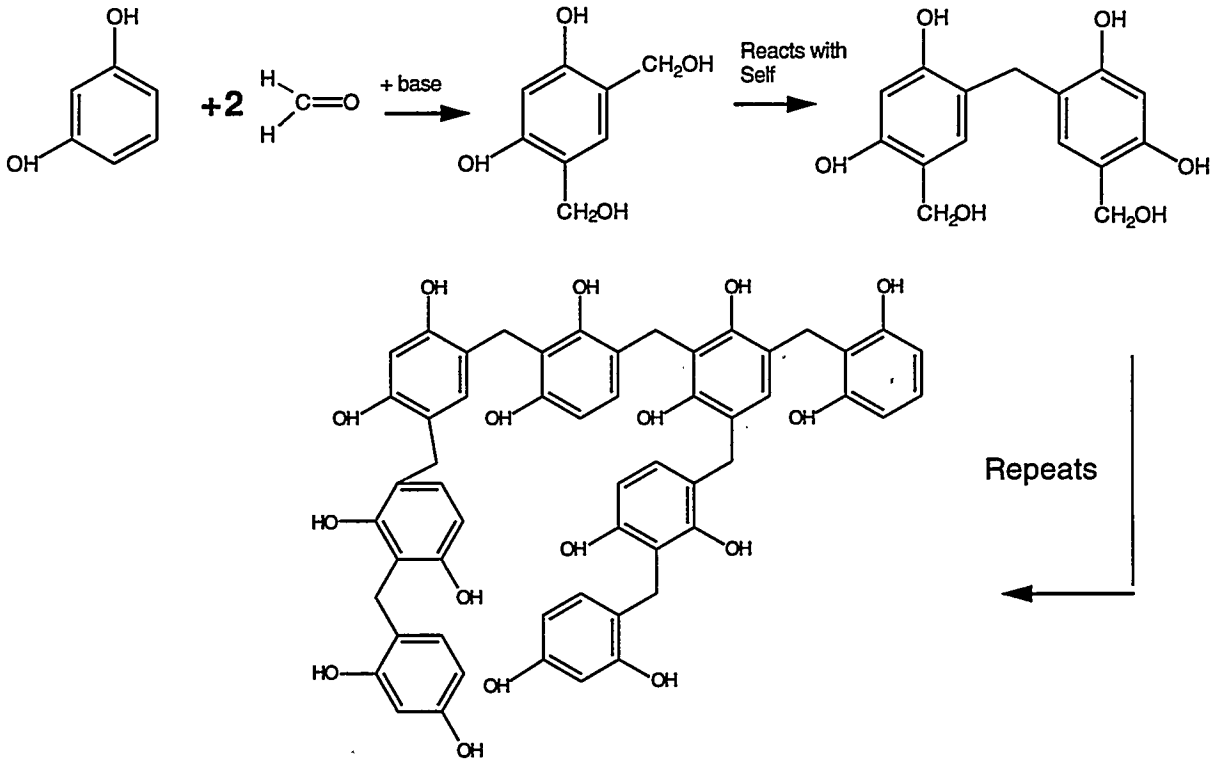

Fig. 5–26. Reaction of resorcinol and formaldehyde under basic conditions that results in bead growth.

The effort began by developing the techniques required to establish an oil/water/oil (O/W/O) system including the identification of appropriate solvents and surfactants. This was followed by an investigation into curing protocols as initial results were unsatisfactory: (1) RF preforms prepared in mineral oil and cured for 1.5–2 hours at 70°C typically collapsed, deformed or dimpled when exchanged directly into isopropanol; (2) cured RF

shells noticeably swelled (i.e., increased in wall thickness and diameter) when in ispropanol (Fig. 5–27); (3) upon supercritical-CO_2 drying, shells shrank in volume 30%–70%.

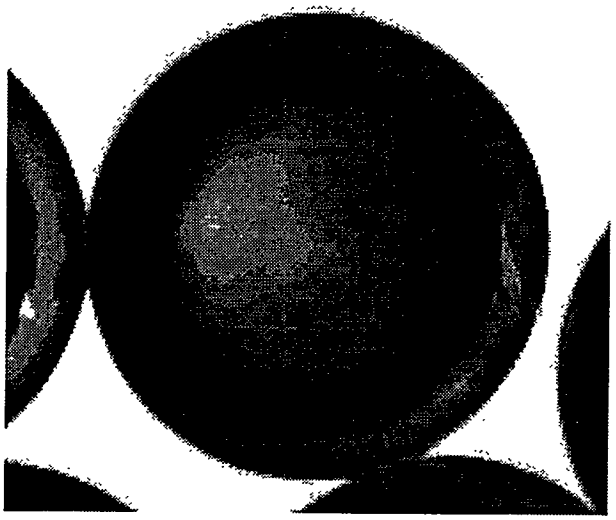

(a)

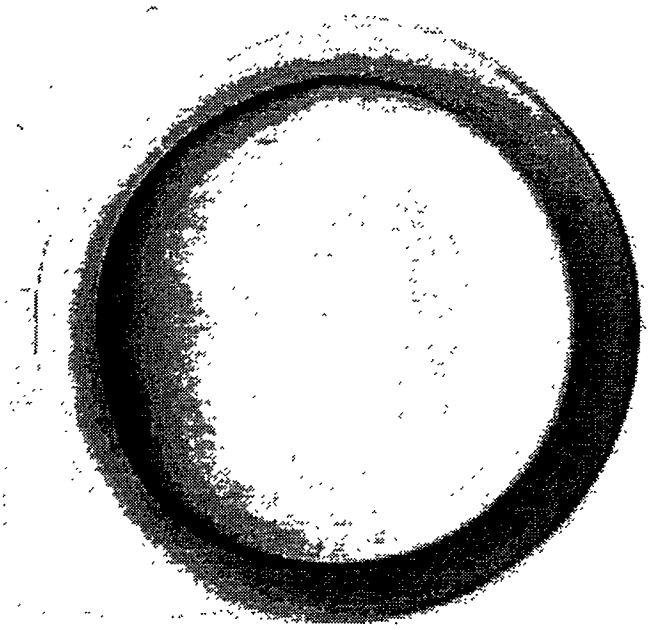

(b)

Fig. 5–27. (a) R/F shell cured for 2 hours in mineral oil + carbon tetrachloride. (b) Swollen R/F shell in isopropyl alcohol (IPA). Both pictures are at the same magnification (18X).

These observations suggested that the material was insufficiently crosslinked. Of the three observations, swelling in isopropanol was deemed the most useful diagnostic. Consequently, we measured the degree of swelling in bulk RF gels in isopropanol as a function of cure time (at 70°C) and formulation variables such as resorcinol-to-catalyst ratio (R/C) and formaldehyde-to-resorcinol ratio (F/R). R/C is the ratio of resorcinol concentration to catalyst concentration or, more accurately, base concentration during bead formation. This ratio controls bead size by determining the number of initial resorcinol anions. The F/R ratio determines the functionality of the substituted resorcinol, to a maximum of three. Figure 5–28 shows the degree of swelling for RF foam with a formulation density of 50 mg/cc. Negligible swelling was obtained with an R/C ratio of 100, an F/R ratio of 3 and a cure time of 29 hours. This result clearly indicates that swelling can be minimized only if the RF shell preforms are cured longer than 2 hours.

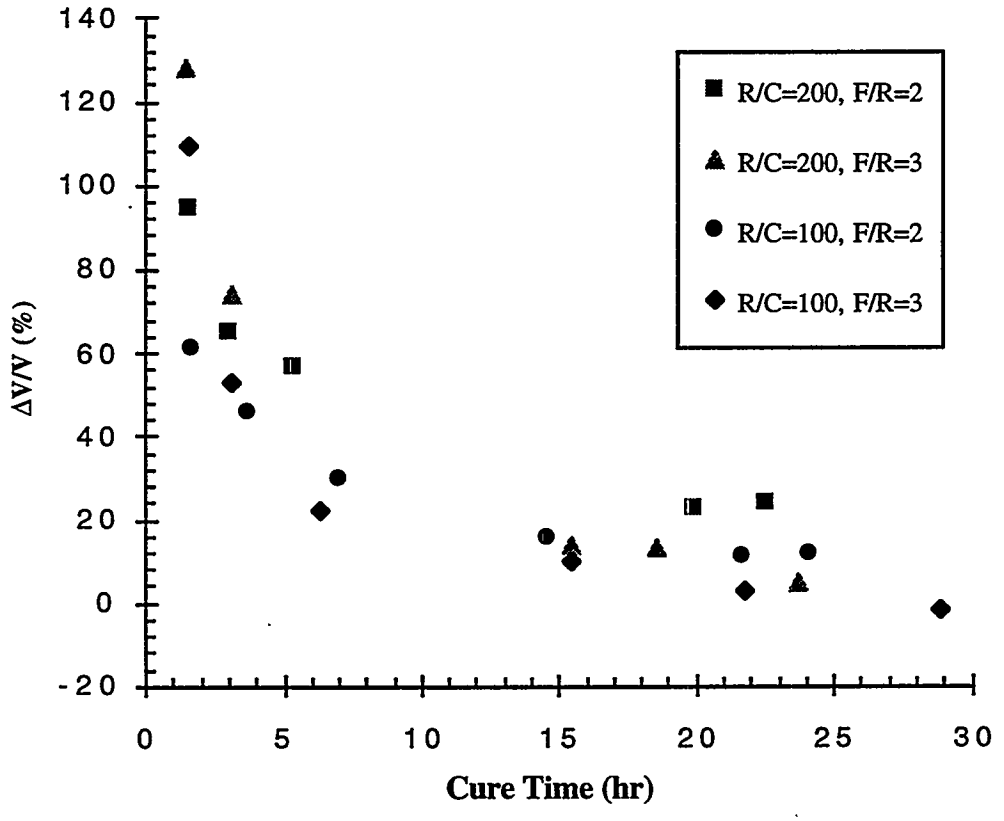

Fig. 5–28. Degree of swelling of R/F gels in IPA as a function of cure time at 70°C, F/R and R/C (theoretical foam density = 50 mg/cc).

Extended cure times are easily obtained for bulk samples cured in vials, but for shell preforms, extended cure times are plagued by dehydration of the preform by the oil phase. This was overcome by adding copious amounts of water after 1.5–2 hours of conventional curing, covering the beaker and heating to 70°C for an additional 18–22 hours. The resulting shells are durable, have exhibited limited swelling in isopropanol, and limited shrinkage after drying (60 to 65 mg/cc in dry foam for a formulation density of 50 mg/cc.)

For further information, please contact S. Lambert (STI).

Interfacial Overcoating. The quality of the extended cure RF foam shells is quite high, as is shown in Fig. 5–29, but to be a useful capsule the shell needs a barrier overcoat to contain the fuel, and for NIF designs a full density ablator layer at least 150 μm thick. The specifications for the overcoat are conformity to the foam shell, optical transparency, uniformity of thickness to 1%, and surface finish of 500 Å rms or better. We realize the difficulty of this task and have allocated significant time and manpower. We expect that a fully optimized overcoated shell will not be available until early 1998. In the near-term, prototype overcoated RF foam shells are being produced by GDP coating, but this technique may not be able to produce target quality surface finish. The reason is an unfortunate synergism between the GDP coating and the dry RF foam. The growth mechanism of GDP coating amplifies surface flaws and drying the delicate RF foam tends cause flaws by handling damage and acquisition of debris.

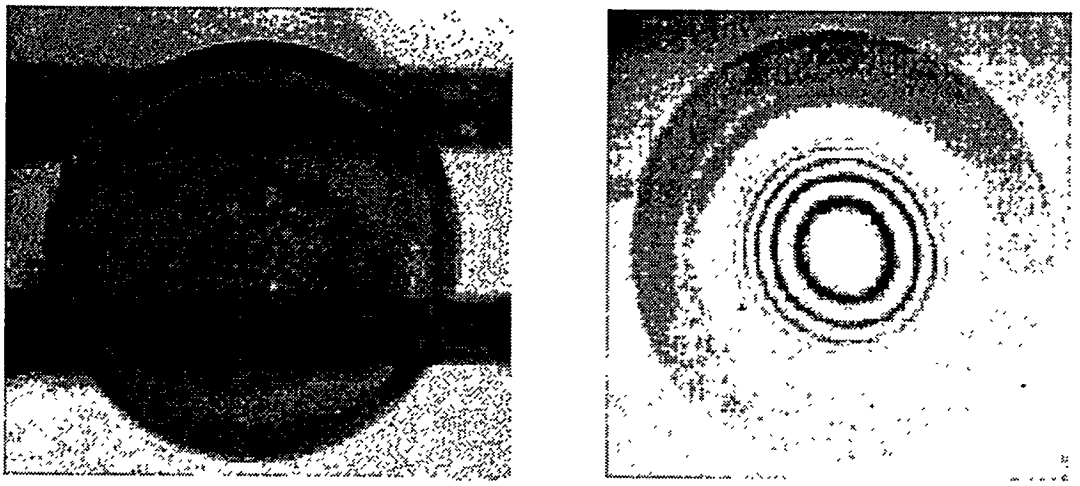

Fig. 5–29. (a) A micrograph of a dried RF shell in transmitted light. The ruler in the background has 1 mm spacings. (b) An interferogram of a dried RF shell. Note the clarity of the fringe.

We are evaluating an alternative coating process, interfacial polymerization. This technique builds a polymer layer at the interface of two immersible solutions. Since it is a wet chemistry technique, it has several appealing qualities. The foam does not have to be dried before overcoating, and the reaction occurs at an interface whose surface energy is lowest when the interface is spherical. Thus the coating will be conformal without replicating surface flaws. Interfacial polymerization is capable of overcoating large batches of shells, thousands per batch, and coating rates are fast, a micron a minute is common.

There are also disadvantages with this technique. First, the internal solution must be chemically compatible with the RF foam. Second, the coating must survive and permit the CO_2 drying of the internal RF foam. Third, it may be difficult to obtain thick walls since one of the reactants must be totally contained within the interior phase. Fourth, we have an unresolved concern about the swelling and deswelling demonstrated by the RF foam shell in various solvents. It is difficult to imagine that an overcoating could match this property, but we have not processed a sufficient number of overcoated shells to evaluate the severity of this problem.

Two interfacial chemistries have been tried: isocyanates reacted with amines, and acid chloride reacted with polymers containing pendant hydroxy groups. The isocyanate-amine reaction was chosen because of its wide usage in industry. It has the reputation of easily producing robust overcoats and is supported by a wealth of technical and patent literature. Isocyanates react with amines to produce polyureas by the following reaction:

$$\mathbf{RNCO + R'NH2 \longrightarrow \quad RNHCONHR'}$$

Monofunctional monomers are indicated, but the actual monomers were difunctional and trifunctional. The isocyanates used were Mondur MR, Mondur ML and Mondur 1437, all derivatives of diphenylmethane diisocyanate, MDI.

The three isocyanates were chosen for their ability to express the range of properties that can be expected from polyureas. The primary differences depend upon the functionality and presence (or lack) of a prepolymer. (For example, Mondur 1437 contains a urethane prepolymer which gives it excellent flexibility.) The amines were also multifunctional, ethylene diamine, 1,6-hexane diamine, and tris(2-aminoethyl)amine $[(H_2NCH_2CH_2)_3N]$. The combination of three isocyanates and three amines provided nine combinations for evaluation.

Due to the chemical sensitivity of the RF foam, we were not able to reproducibly use the aqueous amine solutions as the interior phase. However, the RF foam shells produced by the

extended cure were physically stable enough to place the organic isocyanate phase within the shell. Placing these isocyanate shells in the aqueous amine exterior solution easily produced overcoats, but there was always an opaque layer produced with the clear polyurea layer. IR analysis indicated the opaque layer was the product of isocyanate and water. Procedures were developed to minimize the by-product, but never eliminate it. Another unresolved problem was the degradation of the coating surfaces during the CO_2 drying. The more highly crosslinked systems exchanged into pure ethanol survived best, but damage was still obvious.

The other interfacial polymerization was developed at the University of Osaka (ILE) [Ref. 5–8] for overcoating methacylate foam shells. Isophthaloyl dichloride is reacted with a polymer containing many pendant hydroxy groups, such as poly(vinyl alcohol) (PVA), hydroxyethyl cellulose (HEC), and poly(vinylphenol) (PVP).

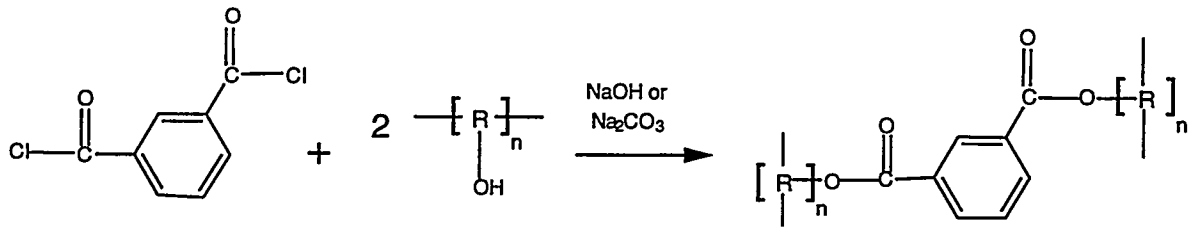

The aqueous solution containing the polymer also must contain a base, and thus risks reaction with the foam when used as the internal phase. However, the organic acid chloride solution does work well as the interior phase, if the shells are not prone to swelling and deswelling. Of the three polymers listed, the PVP based overcoat is the most acceptable. The PVP coating is transparent and there are literature reports of this process producing sub-micron surface finish as shown in Fig. 5–30. There are still disadvantages. The organic solution does cause some shrinkage; there is some evidence of non-uniformity in the coating thickness; there is a tendency for the shells to agglomerate during the coating process; and there is no evidence that a 150 μm coating can be produced. Nevertheless, the results to date are encouraging for this system.

Acknowledgment. We would like to thank Dr. Curt Thies of Washington University, St. Louis, Missouri for his assistance in the interfacial polymerization section of this task.

For further information, please contact D. Schroen-Carey (WJSA).

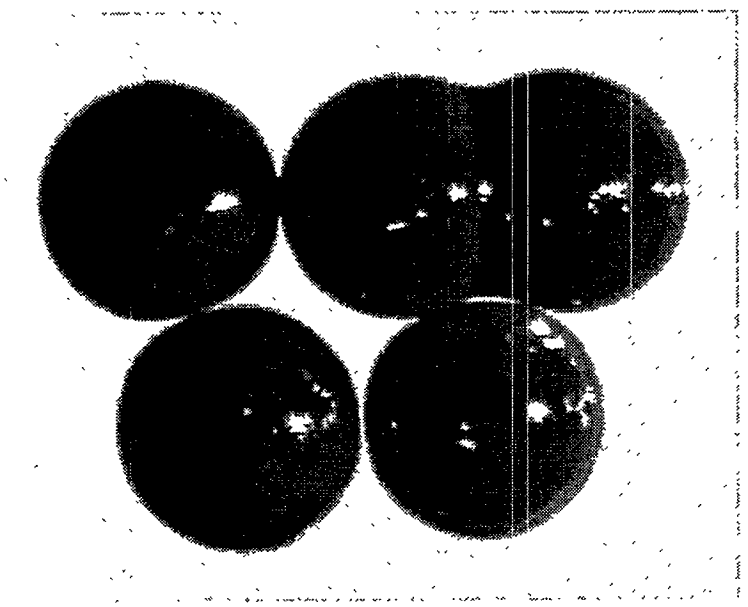

Fig. 5–30. RF Shells overcoated by the PVP-acid chloride technique. The two shells in the upper right hand corner agglomerated together during coating.

5.3.2. METHACRYLATE FOAM SHELL EVALUATION

The objective of this subtask was to pursue the methacrylate foam technology, as developed by researchers at ILE [Ref. 5–9], and to determine its relative worth as compared to RF foam technology. It was anticipated that either this subtask or the Aerogel Foam Shell subtask would be deemed inferior and terminated at some point within the year. Due to the success of the aerogel subtask and the many technical challenges of this subtask, the methacrylate foam subtask was canceled June 29, 1995 (LLNL Report TAT 95-050). This is not to say, however, that this task was unsuccessful. We were able to duplicate the improved optical properties that had devalued the previous methacrylate work. The new formulation based upon ethylene glycol dimethacrylate (EGDM) produced foam beads with densities approaching 60 mg/cc and of improved optical transmission. Shells of EGDM were produced by droplet generator and overcoated by interfacial polymerization. Unfortunately, the final product had optical properties still inferior to RF, and many processing challenges needed to be solved. Given the limited resources available, it was deemed prudent to abandon the methacrylate chemistry.

For further information, please contact S. Lambert (STI).

5.3.3. LIMITATIONS TO CHARACTERIZATION OF FOAM SHELLS

The scattering and refraction of light passing through foam interferes with the characterization of shells containing thick foam layers. The optical properties of foam shells were modeled to clarify the connection between foam structure and light scattering, and to determine the limitations this scattering placed on the characterization of shell geometry. An algorithm was developed which related the edge blurring from refraction by foam density fluctuations to the coherent light dephasing. With this one could predict, from the fuzziness of sharp edges viewed through foam layers, the contrast of the fringes that would be present (Fig. 5–31). Because of the low density of the foam, layer non-uniformities do not shift fringes very much, and image analysis will be necessary to measure their location with sufficient accuracy. It was demonstrated that radial averaging techniques allow one to detect fringe offsets with the required accuracy. A more comprehensive report was issued on this analysis, "Light Scattering Limitations to Interferometric Characterization of Foam Shells," GA–A21981.

For further information, please contact R. Stephens (GA).

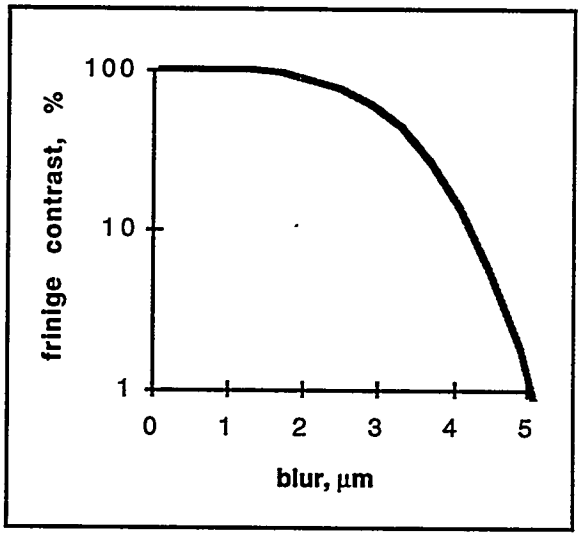

Fig. 5-31. The relationship between edge blur and fringe contrast for the baseline foam shell 1 mm o.d., with a 10 μm thick overcoating on a 90 μm thick, 5% dense, foam layer.

5.4. REFERENCES

[5–1] J.K. Hoffer and L.R. Foreman, Phys Rev Lett. **60,** 1310 (1988).

[5–2] J.T. Larsen, J. Vac. Sci. Technology **7**, 1150 (1989).

[5–3] J.K. Hoffer, et al., Plasma Physics and Controlled Nuclear Fusion Research **3**, 443 (1992).

[5–4] G.W. Collins, et al., "Solid Hydrogen Surfaces," ICF Annual Report **3**, p. 81, Lawrence Livermore National Laboratory, Livermore, California, UCRL-LR-105820-93 (1993).

[5–5] We would like to acknowledge the many useful discussions with Sam Letzring of UR/LLE. It was his suggestion that we use a reentrant cavity design. I would also like to thank him for the loan of several pieces of microwave equipment, including a high power microwave source.

[5–6] G.W. Collins, et al., "Infra-Red Redistribution of D_2 and HD Layers for ICF," to be published.

[5–7] R.W. Pekala, C.T. Alviso, and J.D. LeMay, "Organic Aerogels: A New Type of Ultrastructured Polymer," *Chemical Processing of Advanced Materials*, L.L. Hench and J.K. West, eds., John Wiley and Sons, Inc., New York, 1992. pp. 671–683.

[5–8] M. Takagi, M. Ishihara, T. Norimatsu, T. Yamanaka, Y. Izawa, and S. Nakai, "Development of Foam Shell with Plastic Ablator for Cryogenic Laser Fusion Target," J. Vac. Sci. Technol. A **11**, 2837 (1993).

[5–9] M. Takagi, T. Norimatsu, Y. Izawa, and S. Nakai, "Development of Low Density, Low Atomic Number Foam Shell with Gas Barrier for Laser Fusion Target," Mat. Res. Soc. Symp. Proc. **372**, 199 (1995).

6. OMEGA UPGRADE CRYOGENIC TARGET SYSTEM ENGINEERING

The upgrade of the OMEGA laser at the University of Rochester's Laboratory for Laser Energetics to 30 kJ (351 nm) was completed in April 1995. This upgraded facility has an experimental program that ultimately requires millimeter-size ICF target capsules filled with D–T fuel, maintained at cryogenic temperatures. The ICF capsules are to be filled with D–T fuel, cooled to cryogenic temperature to freeze the fuel, and layered on the inner surface to a thickness of ~100 μm. This dictates that empty capsules be filled to densities (at room temperature) as high as 0.16 gm/cc, equivalent to a pressure of 1100 atm. To achieve high density fills, D–T gas is permeated through the shell wall.

GA has been assigned the task to design, develop, and fabricate a cryogenic target handling system for OMEGA. This system will fill target capsules with up to 1100 atm of D–T gas, cool the capsules to cryogenic temperature (~20 K) to condense the fuel, and transport the filed cryogenic capsules to the OMEGA target chamber. There they will be "layered" to form a uniform shell of D–T ice inside the capsule, characterized carefully and thoroughly and then inserted into the OMEGA target chamber and kept under precisely controlled cryogenic condensations until shot by the OMEGA laser.

GA's D_2 fill station is being modified to serve as the prototype for the UR/LLE D_2 or D–T capsule filling station. The fill station uses a nitrogen gas actuated syringe pump to reach 150 atm pressures (at room temperature). A high pressure gas intensifier is used as a second stage, and increases the working pressure to 1100 atm pressures. After the room temperature permeation fill is complete, the capsules must be cooled below the triple point of D_2, reducing the internal pressure to a few atm to prevent the capsules from bursting. The excess fuel (outside the target) is pumped away and a cold transfer cryostat is used to remove the targets from the permeation system. This requirement for a cryogenic component to the permeation station led to the designing and construction of cryogenic subsystems.

Task activities for FY95 saw the completion of all major subsystems of the high pressure D_2 fill system. All non-cryogenic components were tested and passed all required specifications. The cryogenic components of the fill system have been manufactured but testing is

behind schedule due in part to late delivery of the components by the manufactures. Further detail of all major subsystems will be given in the following sections.

6.1. CONTROL SYSTEM

The control system for the entire OMEGA Upgrade facility is currently using LabVIEW software running on both Macintoshes and PCs. The LabVIEW control program for the permeation cryostat is called ICEPACC, and is an acronym for Inertial Confinement Engineering Permeation Cryostat Controller (ICEPACC). ICEPACC serves as a human-factored graphical user interface to various instruments, controllers, and indicators, and provides manual, automatic, and semi-automatic control of pressure, temperature, and complex positioning equipment. There is also dual stereo-vision feedback from four CCD cameras whose digitized images can be viewed at real-time and on-screen within ICEPACC. The computers use industry standard RS-232 and RS-485 serial communication protocols to communicate with external hardware. In addition, a Scion 4-channel video frame grabber is used for video acquisition, and digital and analog I/O.

ICEPACC performs positioning control for placement and removal of the target racks. These tasks are accomplished using a tri-axis Bellows Manipulator, which is equipped with a stepper motor and an optical encoder for each axis. The motors accept commands from ICEPACC through a dedicated controller, while encoder positions are fed back to ICEPACC via the encoder displays. Visual feedback from the cameras is used to determine distances between objects, i.e., the target rack and the permeation cell, and ICEPACC processes this information for positioning control.

Pressure control is currently done in two stages. The first stage uses two "stepper" valves to step the pressure from vacuum to about 2200 psia. The second stage uses a stepper motor to drive an intensifier that ramps the pressure from 2200 to 22,050 psia. Feedback is accomplished using a Paroscientific pressure transducer, whose output is fed back to ICEPACC.

Temperature control is accomplished by using feedback from numerous four-conductor silicon diode temperature sensors whose outputs are read by two Conductus LTC-20 temperature controllers and two Scientific Instruments 9350 temperature indicators. ICEPACC reads these temperatures, processes them, and then sends control commands to the

LTC-20 controllers. The controllers then adjust output current to temperature control heaters as necessary.

For further information, please contact W. Wier (GA).

6.2. GAS INTENSIFIER

Activities for FY95 included the repair and modification of the high pressure intensifier. After purchase, the intensifier developed a slight leak in the rear packing seal. Packing replacement only temporarily alleviated this problem. Closer inspection of the gas intensifier piston indicated that the leakage actually occurred due to minute pores in the chrome plating on the piston. The chrome plated stainless steel intensifier piston was replaced with a polished tungsten carbide piston. Additionally, teflon and Vespel packing rings were used for sealing the intensifier. Since the intensifier would ultimately be used for tritium handling, elimination of the teflon packing was mandatory. The packing was replaced with a pure Vespel seal ring. The intensifier is effectively leak free (<1 psig pressure drop) at 20,000 psia for a duration of three days and 500 cycles.

Pressure control requirements for the high pressure fill system are dictated by the yield strength of the target. Fill system design requirements were specified to allow for target fills in 5 atm steps to prevent shell breakage. The target fill process takes place over two separate pressure ramps. The first stage is a low pressure ramp from 0 to 150 atm (similar to the pressure is available from the UR/LLE D–T fill system). Two pneumatically actuated valves in series, with a small dead volume (0.072 cc), were added to the fill system. Pressure control from 0 to 150 atm, in 5 atm steps, was achieved by cycling the valves to step pressure. From 150 to 1500 atm, 5 atm pressure resolution was achieved using the gas intensifier. The stepper motor of the intensifier is controlled through a computer interface to adjust the pressure to the required value.

Additionally, we have assessed the amount of tritium which will be adsorbed on the (interior) surfaces of the high-pressure fill station being designed for UR/LLE. The analysis shows that total tritium adsorption will be less than 0.01 Ci on an annual basis. With gold coating on the interior surfaces of the tubing, permeation cell and cryovalves, tritium adsorption is reduced to less than 1 nCi.

For further information, please contact R. Mangano (GA).

6.3. CRYOGENIC VALVES

High pressure cryogenic valves were designed to isolate the permeation cell during cool down (Fig. 6–1). To ensure consistent leak-free sealing at high pressures, a packing-less design was employed. A stainless steel diaphragm was used instead of conventional packing. The design, construction, and acceptance testing of the high pressure cryogenic valves was completed in FY95. The design (Tech Spec 5-0101-01TS/NC) was completed in FY94, but modifications were required due to material failure during prototype testing.

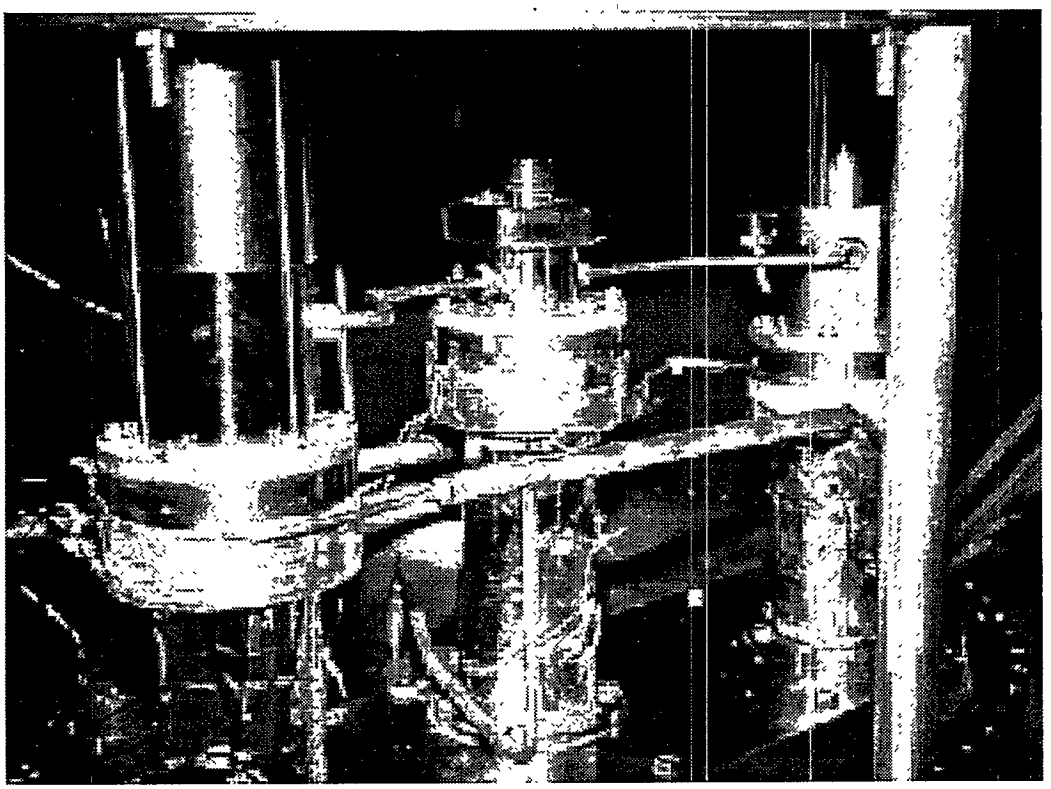

Fig. 6–1. Cryogenic valves and permeation cell (with cap off).

Since these valves are a prototype for the D–T fill system, the valves must be constructed of a tritium compatible material with the ability to withstand the stresses induced during high pressure fills. Suitable materials for such a purpose are: stainless steel (austenetic) and beryllium-copper (BeCu) alloys. To reduce thermal gradients through the valve during cooldown, BeCu was the material of choice. BeCu (C17510) alloy was selected, but in early testing failed based due to poor surface hardness (R_B = 90, Yield = 85 ksi)) which resulted in gauling on the valve seat. We changed alloys to BeCu (C17200), based on high strength (~185 ksi) and hardness (R_C = 50), although elongation = 3%. Testing showed this to be far

too brittle to use for the range of pressures and temperatures specified. To overcome this problem, the BeCu (C17200) was selected in an underage hardened ("half-hard") condition. Properties for this alloy are: Yield = 125 ksi, Elongation = 13%, Hardness $R_C = 25$.

The valves are actuated by a hydraulic hand pump located at the top of the permeation cryostat. A manual actuation system was chosen for the prototype for simplicity. Hydraulic pressure of 80 atm is required to close valves with valves pressurized to 1500 atm. Concentric tubes pass through the top head of the permeation cryostat to the valves (located in the cryostat). To minimize heat load to the permeation cryostat, the valves are actuated through G-10CR tubes. Heat load from the tubes was calculated at ~0.5 W per valve, assuming conduction through both the G-10CR tubes and 60 mTorr of helium gas. Additionally, minimum dead volume is required to achieve required capsule fill pressures without exceeding the UR/LLE site license restriction of 1 gram of tritium. Baseline calculations indicated that each valve could contain no more than 0.5 cc dead volume. Measured valve dead volume of each cryogenic valve is 0.16 cc.

The high pressure cryogenic valves were tested for leak rate across the ports (with valve closed) and leak rate through the valve to the environment (with valve open). Each valve was hydrostatic tested (with the valve open) to a pressure of 25,500 psig, and leak rate to the environment measured below 2.0×10^{-10} std atm-cc/s (the detectable limit of the Balzers HT160 leak detector). The design specification required a leak rate no greater than 1.0×10^{-8} std atm-cc/s. Pressure was then reduced to 22,100 psig, and the leak rate was measured across the closed valve seat. The two valves were nearly identical, with leak rate of $\sim 1.0 \times 10^{-7}$ std atm-cc/sc at room temperature (maximum pressure). The design specification is 1.0×10^{-4} std atm-cc/s. The valves were then cooled to 20 K, and pressure was subsequently reduced to simulate a closed volume. The leak rate decreased with decreasing temperature (and pressure) to a minimum of $\sim 3.0 \times 10^{-4}$ std atm-cc/s at 20 K. The valves were opened at 20 K, and leak rate to the environment still measured below 2.0×10^{-10} std atm-cc/s.

For further information, please contact R. Mangano (GA).

6.4. PRESSURE TRANSDUCERS

Experiments are currently being conducted on a prototype cryogenic pressure transducer manufactured for us by Paroscientific and modified by GA. The transducer is a high-accuracy (0.01% FS), high-pressure (20,000 psia) gauge. A silicon diode temperature sensor

was mounted to the pressure transducer internal circuit board to determine component temperatures. Thus far, the gauge has been tested to LN_2 temperatures and survived, except drift and hysteresis were observed in the output signal between cooldown and warm-up. The circuit diagram was reviewed to determine if a circuit element is causing this anomaly, or if this is a physical effect due to expansion/contraction differences between dissimilar materials.

Two different gauges with different mechanical system designs (Bellows and Bourdon tube) were tested to determine if the gauge failed due to failure in a mechanical component. Additionally, the electronics of the pressure transducer were replaced with electronics proven to operate at low temperatures (GaAs JFETS). Neither approach reduced the hysteresis. Paroscientific has mounted a bare quartz crystal oscillator in a vacuum can for low temperature testing to determine if the crystal is the source of the anomaly. This testing will be started in early FY96.

For further information, please contact R. Mangano (GA).

6.5. PERMEATION CELL

The permeation cell is the pressure vessel used to house the ICF targets during a fill cycle and is shown in Fig. 6–2. A key requirement to the design was tritium compatibility of the permeation cell material, combined with the ability to withstand the stresses induced during high pressure fills. Additionally, it requires good thermal conduction during cooldown. Material selection for the permeation cell design was an underage-hardened BeCu (C17200) based on high strength (Yield = 125 ksi, Elongation = 13%, Hardness $R_C = 25$) and superior thermal properties to typical high strength steels. To ensure consistent leak free sealing at high pressures, replaceable ring seals were included in the design. The seal rings are manufactured from annealed BeCu to ensure against damage to the cell or cap.

The permeation cell was tested with two types of seal rings: 1) a BeCu seal coated with copper (~0.0007 in. thickness) and 2) a BeCu seal coated with gold (~0.0007 in. thickness). Both types of seal rings passed the leak rate tests at pressure (maximum of 22,100 psig at room temperature) with leak rates registering below 1.0×10^{-9} std atm-cc/s (design specification required a leak rate no greater than 1.0×10^{-8} std atm-cc/s). The permeation cell was cooled to 20 K, and pressure was subsequently reduced to simulate an isobaric

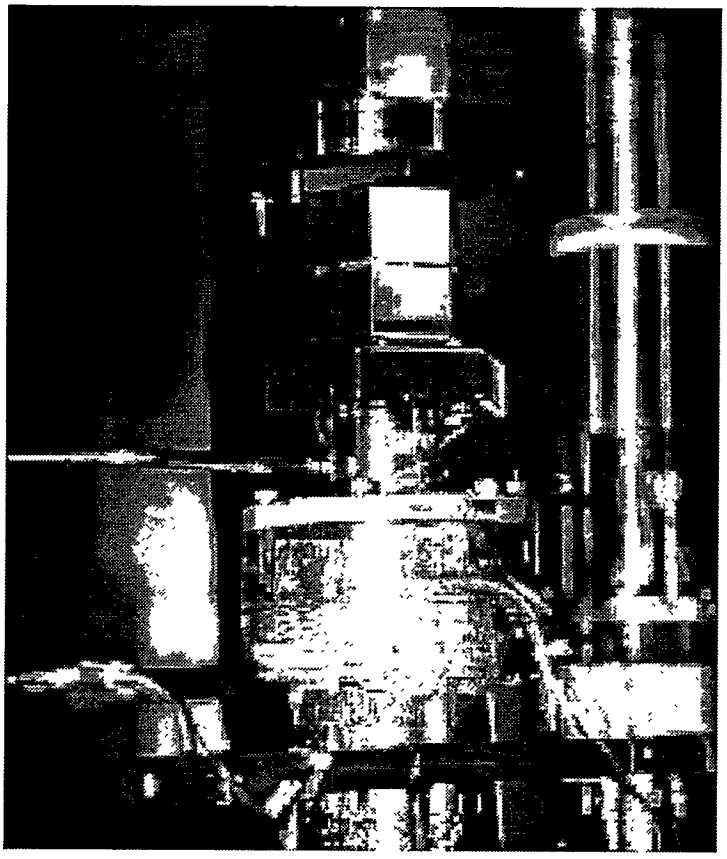

Fig. 6–2. Permeation cell (with cap on).

process. The leak rate remained below the design specification throughout the temperature range. The gold seal ring performed marginally better than the copper coated seal ring, although upon disassembly, we found that part of the gold coating had been stripped from the seal ring and was deposited on the permeation cell cap. If we can't determine a better method of etching the BeCu seal ring surface for gold contact, we will use the copper-coated seal ring. Also, the permeation cell was hydrostatically tested to 27,560 psig and passed.

For further information, please contact R. Mangano (GA).

6.6. CRYOGENIC WRENCH

The function of the cryogenic wrench is to seat the permeation cell cap on the permeation cell, then torque the cell closed to the required load to prevent leakage during pressurization. Once a pressurization cycle is complete and the cell has been cooled, the cryowrench is used to untorque the permeation cell cap and remove the cap to allow access to the targets. The

cryowrench was designed to apply 200 ft-lbs of torque/countertorque to the permeation cell and apply no net torque to the permeation cryostat.

The cryogenic wrench was designed, constructed, and tested in FY95. The cryowrench consists of concentric tubes to apply torque (to permeation cell cap) and countertorque (to permeation cell body) with no net torque transferred to permeation cryostat. Calibration and demonstration testing of the cryowrench was performed.

Temperature sensor and vacuum pressure gauges were installed on the cryowrench for monitoring. Vacuum tests were performed to demonstrate that the cryowrench/bellows manipulator system is leak tight to 10^{-7} Torr. The cryowrench was calibrated using a dummy load cell to determine the torque exerted by the wrench. We then cross-checked the torque load using the surrogate permeation cell. Lastly, we ran a cryogenic test in which we tightened the surrogate permeation cell cap to 120 ft-lbs at room temperature, then cooled the cell and cryowrench to LN_2 temperature. At temperature, we removed (untorqued) the cap, demonstrating a successful cycle. With the permeation cell mounted in the permeation cryostat, the cryowrench was successfully tested on the permeation cell to torque the cell closed, disconnect, reconnect, then open the cell remotely using visual feedback. The wrench successfully torqued the cell to 190 ft-lbs with no net torque applied to the cryostat.

Final testing for FY96 will involve torquing the permeation cell closed, disconnecting, reconnecting, then opening the cell remotely using visual feedback, all at 20 K.

For further information, please contact R. Mangano (GA).

6.7. PERMEATION CRYOSTAT

The permeation cryostat contains the permeation cell, the cryogenic valves, and the shroud manipulator. The permeation cryostat is used to cool the targets after they have been permeation filled with fuel gas in the permeation cell. The cryogenic valves seal the cell from its inlet and outlet lines. This allows the cell to be cooled in a constant volume of nearly exact temperature uniformity. The cryogenic wrench is inserted into the permeation cryostat to seal the cell. The wrench removes the permeation cell cap when the cell has been cooled down to a temperature that condenses the fuel. The cold transfer cryostat is inserted into the permeation cryostat to retrieve the targets from the cell and transport them cold (fuel condensed) to the insertion system. The shroud manipulator removes and replaces the inner

and outer shrouds of the cold transfer cryostat so that the targets may be picked up and placed inside the inner shroud of the cold transfer cryostat.

The permeation cryostat is shown in Fig. 6–3. General Atomics supplied a technical specification to Applied Engineering Technologies Limited, who designed and built it. General Atomics installed the permeation cell, cryogenic valves and shroud manipulator. It is cooled by secondary cooling loops that pass through a liquid nitrogen pot, the first and second stages of a Balzers UCH 130 Gifford-McMahon cryocooler, and counter-flow heat exchangers. No liquid helium was used, based on earlier discussion with personnel from the University of Rochester's Laboratory for Laser Energetics. The cryostat operates between three states:

State 1: the cryostat at room temperature

State 2: the inner vessel of the cryostat cold, the permeation cell and cryogenic valves at room temperature, and the inner vessel evacuated

State 3: the inner vessel, the cell, the valves cold and the inner vessel containing an amount of helium gas used for thermally linking the targets to the cryostat.

Targets are permeated in State 2 and condensed and retrieved in State 3. The secondary cooling loops can switch between eight gas flow configurations: five for cooling, two for warming, and one for purging. Multiple flow patterns are used to optimize the cooling of the system; each flow pattern being of better efficiency in its own temperature regime.

The permeation cryostat's performance was tested as delivered using surrogates for the permeation cell, cryogenic valves, and shroud manipulator. Attempting the transition, State 1 to State 2, took 20 hours to achieve a temperature of 24.6 K. Attempting the transition, State 2 to State 3, took 12 hours to achieve a temperature of 26 K (50 mTorr helium in inner vessel). With the cryogenic wrench inserted into the cryostat, the State 3 operation mode achieved a 25.6 K average inner vessel temperature and cooled the wrench to 30.6 K (6 mTorr helium in inner vessel). These results are not quite as good as we had hoped, which was to achieve 20 K in about 4 hours. To put these results into perspective, however, a target filled to 1100 bar at 300 K would experience 10 bar at 30.8 K. Thus, the permeation cryostat should have sufficient performance to permit a successful demonstration of cold target transfer.

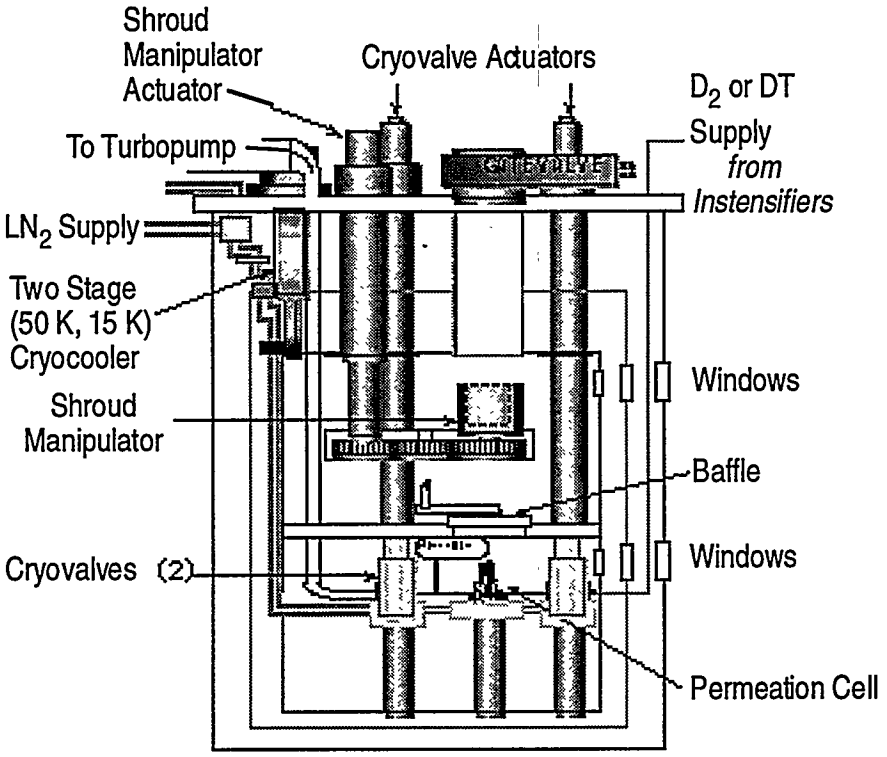

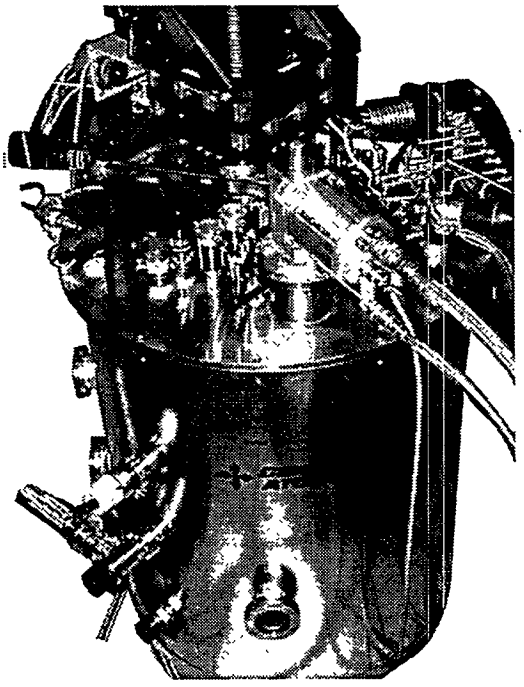

Fig. 6–3. The Permeation Cryostat. It is 44 in. tall by 32 in. in diameter. The bottom of cold transfer cryostat is visible on top of the permeation cryostat.

The cryocooler has a capacity of 15 watts of cooling at 20 K. We have examined the permeation cryostat and find that by making minor changes we could reduce heat leak into the cryostat by 2 to 3-1/2 watts. These changes have been implemented and should create lower base temperatures. This will increase the margin for successful cold target transfer.

At four targets per cool down (State 2 to State 3), a transition time of 12 hours will not be sufficient for a target throughput of four targets per day delivered to the target tank center. The filling, transfer, layering, characterization, and insertion into the target tank center will more than exceed the remaining twelve hours. Therefore, the cool down time should be brought down to three hours. There are a number of options to improve performance: Multiple cryocoolers can be used, liquid nitrogen can be used to cool the thermal shield directly and to initially cool the permeation cell and valves directly, liquid helium with a re-liquifier could be employed in place of the cryocooler. These and other options will be evaluated for implementation in FY96.

For further information, please contact Dr. Neil Alexander (GA).

6.8. SHROUD MANIPULATOR

The shroud manipulator is used to remove and re-attached the inner and outer shrouds of the cold transfer cryostat. This is done before and after the cold transfer cryostat picks up the target rack, respectively. The manipulator is located in the inner vessel of the permeation cryostat, upper chamber. The inner vessel is split into two chambers by the baffle plate. There are a pair of nested sockets at the end of each arm of the manipulator. These apply torque and counter torque to seal the shrouds to the cold transfer cryostat without rotating the body of the cryostat or applying net torque to it. The shroud manipulator can apply 50 ft lbs torque to seal the shrouds' resealable cryogenic vacuum seals.

The shroud manipulator is show in Fig. 6–4 installed on the test stand. On the test stand, the manipulator has removed the shrouds from the cold transfer cryostat. Its gear train has been operated at room temperature and in liquid nitrogen. Initially, the bushings galled after a few tens of turns while hanging in the test stand. These original bushings were made of bearing bronze, C54400. The off-axis moment of the manipulator puts a high pressure on the bushings of its drive shafts. The drive shaft bushings were replaced with bushings with a composite structure, Garlock DU bushings which have a stainless steel body coated to a thickness of 0.010 in. with a sintered bronze filled with lead and PTFE (teflon). The

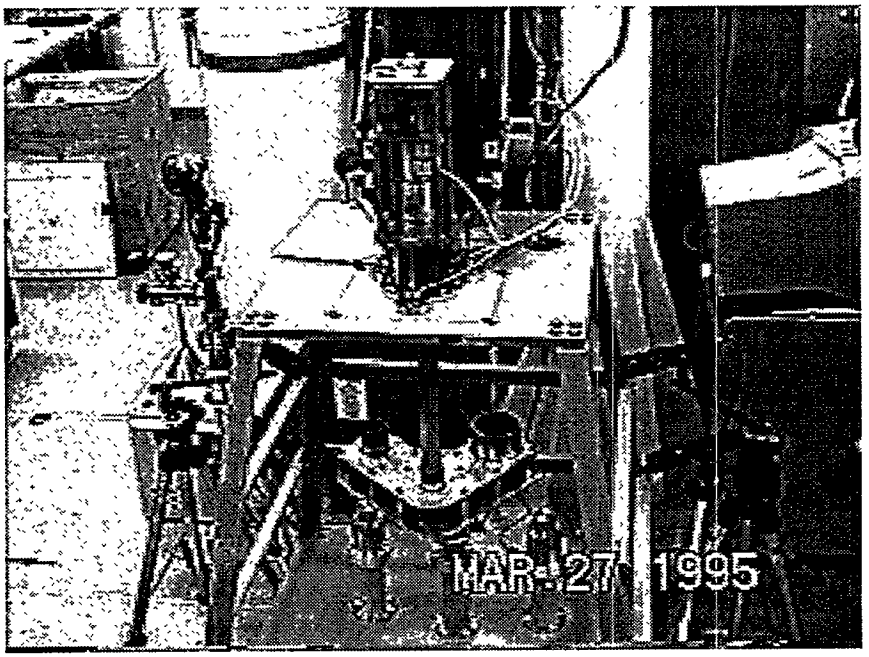

Fig. 6–4. The shroud manipulator hanging inside the test stand.

remainder of the bushings were replaced with a sintered bronze filled to 3% by weight with molybdenum disulfide. With the new bushings installed we have not suffered any galling. The shroud manipulator is now installed in the permeation cryostat where it will be tested at cryogenic operating temperatures.

For further information, please contact Dr. Neil Alexander (GA).

6.9. COLD TRANSFER CRYOSTAT

The cold transfer cryostat is used to pick up a rack of four filled and mounted targets and transport them to the layering and insertion apparatus. Targets are mounted on extremely low thermal conductivity fibers. To maintain a cooling link to the targets, the targets are placed inside the inner shroud, which is filled with helium gas. Cryogenically resealable vacuum seals are used on the shrouds. The inner seal prevents the helium from leaking into the insulating vacuum space between the shrouds. The outer seal prevents helium from leaking into the insulating vacuum space between the shrouds when the cold transfer cryostat is first introduced into a helium gas filled permeation or layering cryostat. The multiple vacuum spaces minimize heat load. The shroud manipulator in the permeation cryostat

removes and re-installs the shrouds onto the cold transfer cryostat (Fig. 6–5) when it picks up the target rack from the permeation cell.

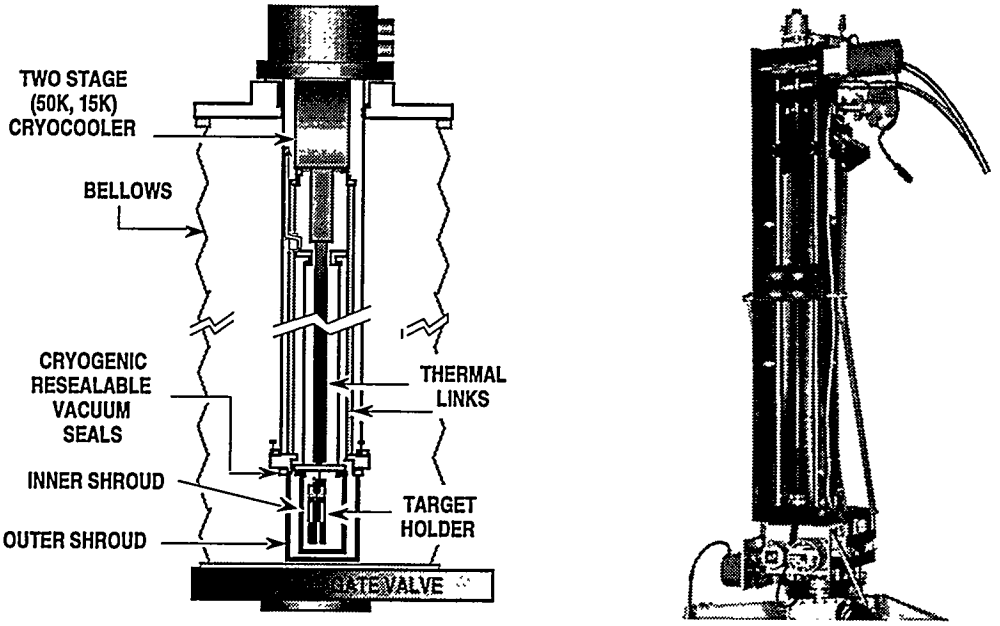

Fig. 6–5. The cold transfer cryostat

The cold transfer cryostat is built around an APD DE-204-6.5 cryocooler with a base temperature of 6.5 K. Heat is removed from the inner shroud and the thermal shield by conduction. The lowest observed temperature on the inner shroud is 6.9 K. Without helium gas in the inner shroud, the shroud cools to 30 K in 5 hours and 20 K in 8 hours. Helium in the inner shroud will decrease cooling time by providing an additional conductive link.

The cold transfer cryostat has been operated to pick-up and set down the target rack into the permeation cell in the permeation cryostat. This was done using only the controls, data, and video images displayed on the console of the monitoring computer.

Tests were also performed on the cold transfer cryostat to determine the effect of injecting helium into various of its spaces. The inner and outer shrouds were installed and the leak rates measured. For one atmosphere of helium gas pressure across the seal the leak rates were 1.1×10^{-7} and 2.1×10^{-7} std atm cc/s, respectively. The outer bellows vacuum space was filled to 0.5 Torr with helium. In two hours, the inner shroud temperature rose from 8.4 K to 12.2 K. The inter-shroud space was not pumped during this or the following test. In this test the bellows was evacuated of helium gas and then the inner shroud was filled to

130 Torr with helium gas. In two hours, the inner shroud temperature rose from 9.6 K to 16.0 K. The first test represents the process when the cold transfer cryostat first enters the permeation cryostat. The second test represents the process when the cold transfer cryostat is moving from the permeation cryostat to the layering and insertion cryostat. In both cases, the anticipated pressure of use is 0.05 Torr. The actual time is anticipated to be less than 30 minutes. Since the inner shroud temperature never went above 30.8 K (which corresponds to 10 bar internal target pressure, Section 6.6), over these extremes of operating parameters, this demonstrates that the cold transfer cryostat is operating well within the required parameters.

Two more tests need to be carried out on the cold transfer cryostat before it is ready to demonstrate cold transfer of filled targets. The first is testing the thermal load the cold transfer cryostat places on the permeation cryostat when inserted. The second test is to practice removing and re-installing the shrouds using the shroud manipulation while inside of the permeation cryostat.

For further information, please contact Dr. Neil Alexander (GA).

6.10. MOBILE POWER CART

The mobile power cart (Figs. 6–6 and 6–7) is used to provide electrical power and structural support to the cold transfer cryostat as filled targets are transported from the fill station (LLE Room 157a) to the cryogenic target positioning system (*La Cave*). The cold transfer cryostat includes a helium gas expander which provides cooling to maintain the targets at approximately 18 K. Compressed helium gas is supplied to the expander by a compressor on the mobile power cart. While being transported, power is supplied to the compressor by a battery powered inverted. An inverted is used to convert the battery bank voltage of 24 V dc to the 220 V ac required by the compressor. The compressor is water cooled and hence a water/air heat exchanger (cool-pa) is used to cool the water. The mobile power cart also contains an instrumentation rack for vacuum and temperature readouts and a controller for position control of the cold transfer cryostat.

System assembly and shakedown were successfully completed. A test plan was written, approved and released (GA Document #5-0103). Acceptance tests were conducted from January 1995 to March 1995. The mobile power cart successfully passed all tests. The

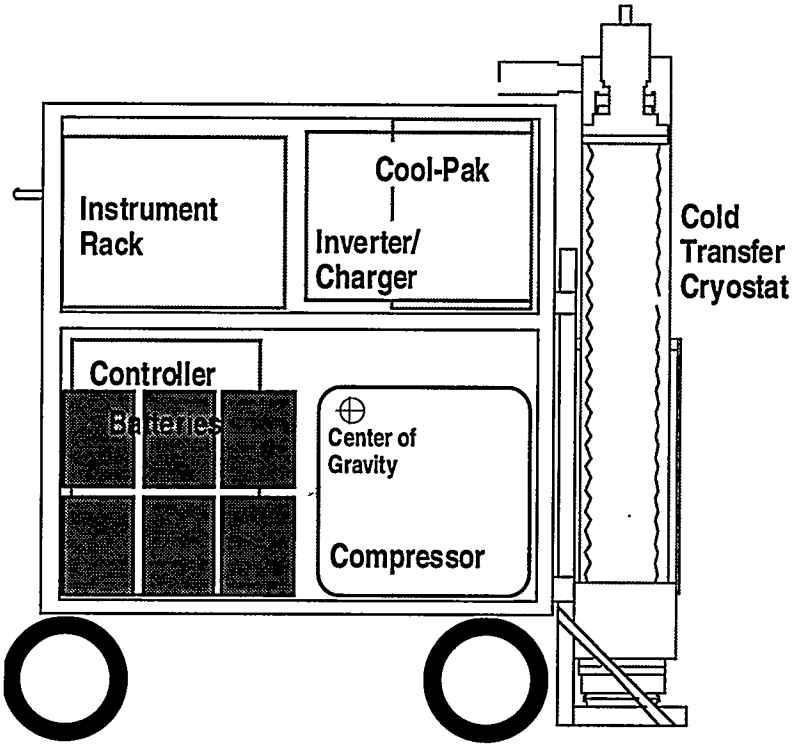

Fig. 6–6. Sketch of mobile power cart

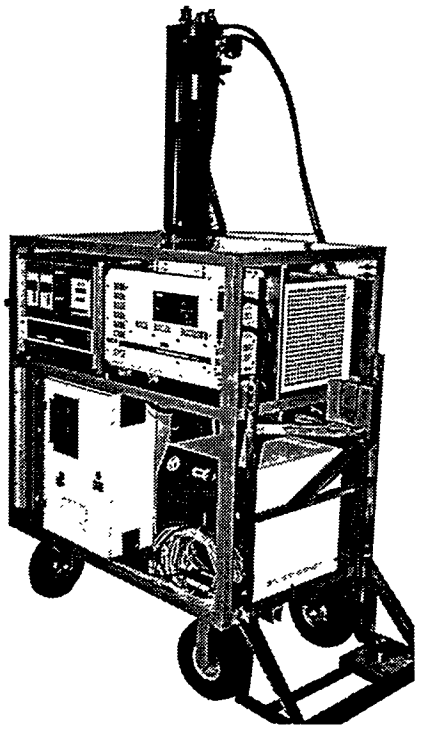

Fig. 6–7. Photograph of mobile power cart

battery bank powered the compressor and other cart components for over 40 minutes. The actual journey time from Room 157a to La Cave has been measured to be less than 5 minutes. The cart was successfully moved by one person, however it is heavy (1200 lbs) and an electrically powered cart may be purchased in the future.

6.11. CRYOGENIC TARGET POSITIONING SYSTEM

We continued to develop two concepts for inserting and positioning a cryogenic target in the OMEGA Upgrade facility. Both the cryogenic elevator and the moving cryostat appear to be viable techniques for beta layered solid D–T targets. Further resolution was made of several design requirements and the operating envelope was expanded slightly which improved the viability of both concepts

6.11.1. DESIGN BASIS

Shroud Withdrawal Time. A major design driver is the requirement that the cryogenic shroud be withdrawn far enough that the shroud is not damaged excessively by the x-rays and fast enough that the target is not heated excessively. The University of Rochester has stipulated that the shroud must be withdrawn at least 20 cm at shot time. Our original calculations indicated that the target could be exposed to the room temperature environment of the target chamber for no more than 20 ms. We have made new estimates of the time permitted for shroud withdrawal. Both the acceptable temperature rise of the target and the heat flux to the target have been investigated. The time permitted for shroud withdrawal has increased significantly from early estimates.

The radiant heat flux from room temperature to a typical target at 18 K was modeled. Assuming a 10 micron thick polystyrene shell with a 100 micron D–T layer, the effective emissivity is 0.02. Most of the adsorption is in the polystyrene shell. These results were confirmed by experimental measurements at Syracuse University on polystyrene shells where the measured emissivity ranged from 0.02 to 0.03. Using 0.05 as the emissivity for the target, this permits a twenty fold increase in the shroud withdrawal time.

The allowable temperature change after layering was calculated using a finite element model in spherical geometry. We found that ±0.35 K is a reasonable temperature limit for layered targets. Initial calculations, using a flat plate model, gave ±0.2 K as the permitted temperature change. Use of ±0.35 K permits a 75% increases the shroud withdrawal time. The temperature change limit is based on not exceeding 2/3 of the elastic limits of the layer

during temperature transients. During final shroud withdrawal only temperature increases are possible so there is no reason to arbitrarily exclude the plastic flow regime and larger temperature variations may be allowed. Recent experiments at LLNL indicate that the D–T may survive 6 K temperature excursions without obvious effect on the surface. The real limit may turn out to be the uncertainty in temperature of the void volume, and thus D–T pressure, upon heating.

Together, these results indicate that a significantly longer time may be available for shroud withdrawal. Conservatively we can assume 100 ms for shroud withdrawal instead of 20 ms. This will significantly decrease the complexity of the CTPS. Rather than first slowly remove the majority of the shroud mass and then quickly remove the last low mass shroud we now assume that a single shroud assembly will be removed at a moderate rate.

Layering Interruption. LLNL performed experiments on the effect of heat flux through a hydrogen layer on surface roughness and found that layers formed under heat flux remain smooth for only a few minutes after removal of heat flux. Discussions between GA and LANL came to a similar estimate for beta layered targets. If these estimates are correct, and there seems no basis for doubting them, the CTPS will need continuous layering capability until a few minutes before shot time. Characterization capability at tank center will also be very desirable.

6.11.2. CRYOGENIC ELEVATOR

Layout of the cryogenic elevator continued through mid-year. The emphasis was on the problem of maintaining the target at a uniform temperature while transporting the target from the layering module to the center of the target tank. The primary problem was to maintain constant temperature in the region where the shroud from above met the elevator from below.

The elevator carriage is assumed to be cable or wire driven so as to have the transfer from the layering system to the elevator occur low within *La Cave*. If a floor penetration is permitted, other options are available.

The key design area of the elevator concept was viewed to be the thermal gradients in the vicinity of the shroud lower pylon interface. A finite element model was constructed of the room temperature O-ring seal region. One of the main advantages of the cryogenic elevator is that all seals can be warm, as opposed to at cryogenic temperatures. This design has the O-ring seal only a few centimeters away from a cryogenic structure. A finite element model

of this area has confirmed that despite these large temperature gradients, the O-ring seal can be maintained at room temperature.

An uncertainty that remains for the moving elevator concept is layer uniformity. A layering sphere can be incorporated in the shroud assembly but the layer would undergo some degradation during transport from the layering apparatus. If the transit time is short (a few minutes) and there is sufficient time (1-1/2 hours) after the target reaches the shroud layering sphere for the layer to heal the results should be acceptable.

6.11.3. MOVING CRYOSTAT

Although the cryogenic elevator concept appears feasible, the moving cryostat appears to be more flexible and better able to accommodate possible future changes in layering techniques. At mid-year a decision was made, in conjunction with LLE, that the moving cryostat would be selected if the key design concern, the parting joint between the shroud assembly and the cryostat base, could be successfully resolved and experimentally demonstrated.

The moving cryostat, Fig. 6–8, is now designed such that layering takes place completely within the cryostat. Several moving cryostats will be used so that several targets can be layered at the same time. What was the layering and characterization module becomes a transfer station where the target rack from the fill system cold transfer cryostat is unloaded and the targets stored until use. An alternative, still being investigated, is the elimination of the fill station cold transfer cryostat: the moving cryostat would then perform the additional function of transferring the target from the tritium laboratory.

The transfer station is not as simple as it appears. Within this cryostat there must be several manipulators to disassemble the target rack, place the targets in a storage rack, remove and replace the shroud assembly of the moving cryostat and position the target in the moving cryostat. The low head room in *La Cave* presents a real challenge. Even using the full height through the floor penetration beneath the target tank, it will be difficult to position the fill system cold transfer cryostat above, and the moving cryostat beneath the transfer module if the target transfers are confined to a horizontal plane within the transfer module.

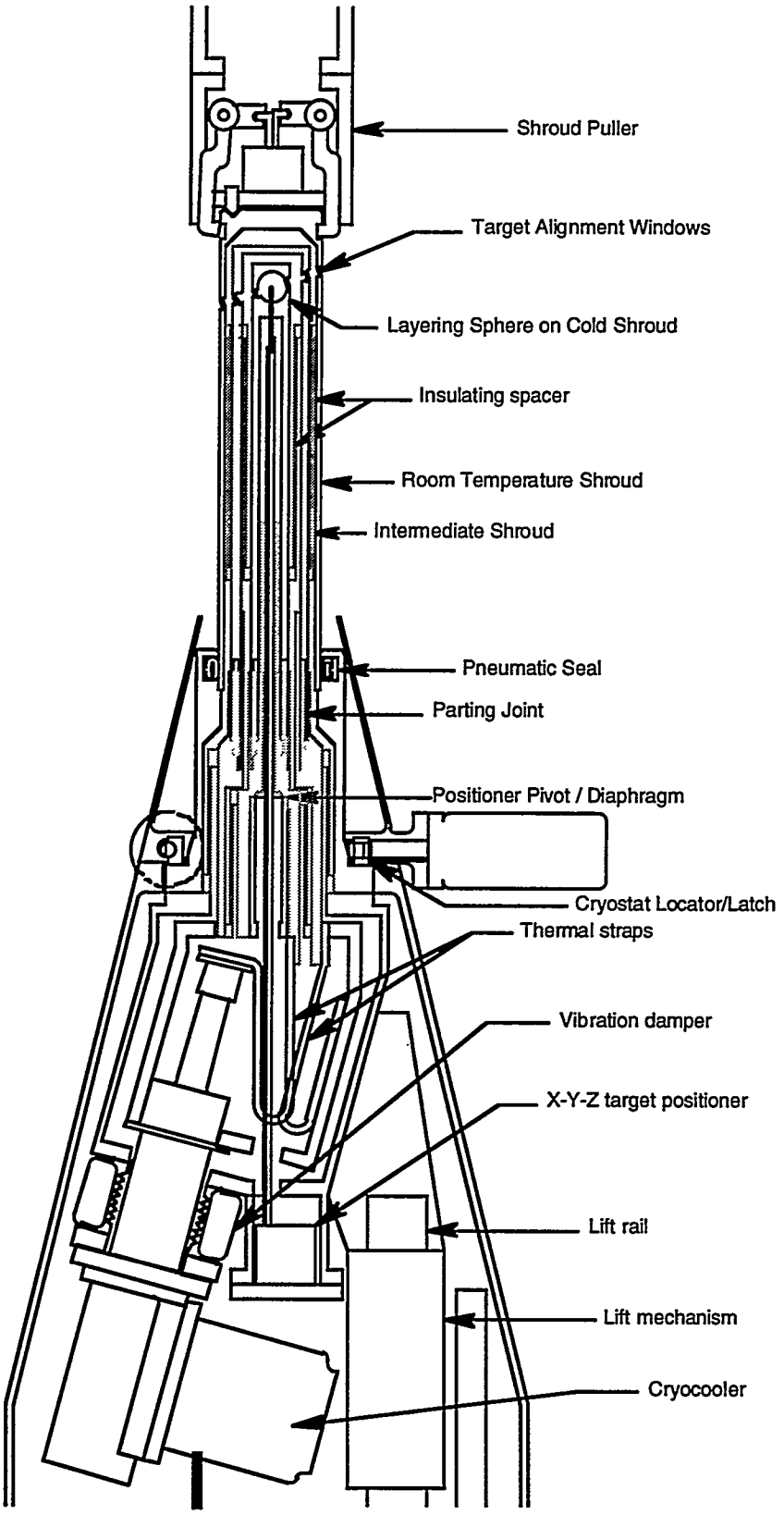

Fig. 6–8. Detailed layout of the moving cryostat.

6.12. SUMMARY OF CRYOGENIC TARGET SYSTEM ENGINEERING

FY95 saw the completion of all major subsystems of the D_2 fill and transport systems. Testing is well underway; all non-cryogenic components were tested and met specification. Cryogenic testing is underway. Design of the next major system, the cryogenic target positioning system was begun. A summary of the technical accomplishments for FY95 is given below.

Permeation Cryostat Control System. This system provides manual, automatic, and semi-automatic control of the pressure, temperature, and mechanical positioning for placement and removal of the target racks. Software for this system, using the LabVIEW program, was written and successfully tested. The system uses dual stereo-vision feedback from four CCD cameras whose digitized images can be viewed in real-time and on-screen within ICEPACC.

Gas Intensifier. Replacement of the chrome plated stainless steel intensifier piston with a polished tungsten carbide one alleviated the slight leaking problem. Additionally, teflon packing seals were replaced with Vespel to enhance tritium compatibility. The modified intensifier was tested and found to be essentially leak free (<0.1 psig pressure drop) at 20,000 psia for a duration of three days and 500 cycles.

Cryogenic Valves. The design, construction, and acceptance testing of the high pressure cryogenic valves were completed in FY95. The valves are composed of BeCu alloy, chosen for tritium compatibility and high thermal conductivity, and are actuated by a hydraulic hand pump located at the top of the permeation cryostat. Calculation of dead-volume within the valves indicate a maximum of 0.5 cc, with measured dead-volume of each cryogenic valve at 0.16 cc. Testing of these valves showed very low leak rates of 10^{-7}–10^{-10} std atm-cc/s (room temperature and 20 K respectively).

Pressure Transducers. Work on the cryogenic pressure transducer has not led to successful results thus far. The transducers still exhibit hysteresis effects and thus significant errors when cycled under cryogenic conditions. Additional work and tests are continuing.

Permeation Cell. Material selection for the permeation cell design was an underage-hardened BeCu (C17200) alloy, chosen for tritium compatibility and superior thermal and mechanical properties. Consistent leak-free sealing is insured by incorporation of replaceable BeCu ring seals into the design. The permeation cell was tested with two types of seal rings;

1) a BeCu seal coated with copper (~0.0007 in, thickness) and 2) a BeCu seal coated with gold (~0.0007 in. thickness). Both types of seal rings passed the leak rate tests at pressure (maximum of 22,100 psig at room temperature) with leak rates registering below 1.0×10^{-9} std atm-cc/s (design specification required a leak rate no greater than 1.0×10^{-8} std atm-cc/s). The permeation was also hydrostatically tested to 27,560 psig and passed.

Cryogenic Wrench. The cryogenic wrench to install and remove the permeation cell cap was designed, constructed, and tested successfully to 190 ft-lbs of torque in FY95. The cryowrench applies torque (to the permeation cell cap) and counter-torque (to the permeation cell body) with no net torque transferred to the permeation cryostat. Final testing for FY96 will involve complete torquing experiments conducted at 20 K.

Permeation Cryostat. The permeation cryostat, designed and built to GA specifications by Applied Engineering Technologies Limited, achieved temperatures as low as 25 K. This temperature will allow demonstration filling and cold transfer of targets. However, some redesign of the system will be required to reduce cool down times such that target filling can be accomplished in less than 24 hours.

Shroud Manipulator. Testing of the original shroud manipulator in its test stand resulted in galling of the bushings after a few tens of turns. After making modifications to improve the bearing alignment and bearing materials, the galling problem has been alleviated. The shroud is now installed in the permeation cryostat where it will be tested at cryogenic operating temperatures.

Cold Transfer Cryostat. The cold transfer cryostat is used to pick up a rack of four filled and mounted targets and transport them to the layering and insertion apparatus. The cold transfer cryostat has demonstrated the ability to pick up and set down the target rack into the permeation cell in the permeation cryostat. Two more tests remain to be completed before this device is ready to demonstrate cold transfer of filled targets — 1) measurement of the thermal loading the cold transfer cryostat places on the permeation cryostat during insertion, and 2) removal and re-installation of the cold transfer cryostat shrouds using the shroud manipulator while inside the permeation cryostat.

Mobile Power Cart. The mobile power cart was assembled and testing was successfully completed. A test plan was written, approved and released. The battery bank powered the compressor and the cart components for over 40 minutes. The cart was also successfully

maneuvered by one person, however an electrically powered cart may be purchased in the future.

Cryogenic Target Positioning System. Recent calculations have shown that a shroud withdrawal time of 100 ms (instead of 20 ms as originally estimated) will be acceptable. This will make engineering design of the withdrawal system much less complex. Two conceptual designs, an elevator concept and a moving cryostat design, have been considered and both appear feasible. The moving cryostat concept proved to be more flexible of the two, but selection of the final concept will be based on tests that are scheduled for early FY96.

7. PUBLICATIONS

Alexander, N.B., "Cryogenically Resealable Vacuum Seals," in the *Proceedings of the Tenth Target Fabrication Specialists' Meeting*, Taos, New Mexico, February 6–10, 1995.

Ankney, J.S., and Hoppe, M.L., "Chlorine Uptake by Plasma Polymerized CH Polymer Stored in Chlorine Gas," in the *Proceedings of the Tenth Target Fabrication Specialists' Meeting*, Taos, New Mexico, February 6–10, 1995.

Beighley, D.H., Baugh, W.A., and Stephens, R.B., "Hi-Voltage Electro-Static Shell Pick-Up Tool," in the *Proceedings of the Tenth Target Fabrication Specialists' Meeting*, Taos, New Mexico, February 6–10, 1995.

Bieri, R.L., "Thermal Modeling of Liquid Layering Experiment," in the *Proceedings of the Tenth Target Fabrication Specialists' Meeting*, Taos, New Mexico, February 6–10, 1995.

Bittner, D., Bieri, B., Monsler, M.J., Sater, J., Bernat, T., Giedt, W., Mapoles, E., and Sanchez, J., "Recent Results of Thermal Gradient Layering Experiments," in the *Proceedings of the Tenth Target Fabrication Specialists' Meeting*, Taos, New Mexico, February 6–10, 1995.

Bittner, D., Burmann, J., Sater, J., Sanchez, J., Giedt, W., Mapoles, E., and Pipes, J., "Measurement and Control of Liquid Hydrogen Mixtures on Capsules with Attached Fill Tubes," in the *Proceedings of the Tenth Target Fabrication Specialists' Meeting*, Taos, New Mexico, February 6–10, 1995.

Brown, L.C., Gibson, C.R., and Fagaly, R.L., "Target Insertion System Conceptual Design for OMEGA Upgrade," in the *Proceedings of the Tenth Target Fabrication Specialists' Meeting*, Taos, New Mexico, February 6–10, 1995.

Burman, J., Schroen-Carey, D., Letts, S., and Sanchez, J., "Fabrication Techniques for Cryogenic Targets," in the *Proceedings of the Tenth Target Fabrication Specialists' Meeting*, Taos, New Mexico, February 6–10, 1995.

Cheung, L., Boone, T., and Nelson, D., "Production of Large ICF Targets via Controlled-Mass Microencapsulation," in the *Proceedings of the Tenth Target Fabrication Specialists' Meeting*, Taos, New Mexico, February 6–10, 1995.

Fagaly, R.L., Alexander, N.B., Mangano, R.A., and Gibson, C.R., "High Pressure Target Fill System for the OMEGA Upgrade ICF Laser," in the *Proceedings of the Tenth Target Fabrication Specialists' Meeting*, Taos, New Mexico, February 6–10, 1995.

Fagaly, R.L., Alexander, N.B., Mangano, R.A., and Gibson, C.R., "High Pressure Tritium Fill System for the OMEGA Upgrade ICF Laser," in the *Proceedings of the Fifth Topical Meeting on Tritium Technology in Fission Fusion and Isotopic Applications,* Lake Maggiore, Italy, May 28 through June 3, 1995.

Gibson, J.B., Baugh, W.A., Brown, L.C., Husband, D.O., Hoppe, M.L., and Steinman, D.A., "Polyvinyl Alcohol (PVA) Coating Process at General Atomics," in the *Proceedings of the Tenth Target Fabrication Specialists' Meeting*, Taos, New Mexico, February 6–10, 1995.

Hendricks, C.D., Bieri, R., Casey, B., Dropinski, S., McClellan, M., and Motta, B., "The Photon Tunneling Microscope as a Characterization Tool," in the *Proceedings of the Tenth Target Fabrication Specialists' Meeting*, Taos, New Mexico, February 6–10, 1995.

Hoffer, J.K., Foreman, L.R., Mapoles, E., and Simpson, J., "Preliminary Experiments on the Beta-Layering Process in a Toroidal Cell," in the *Proceedings of the Tenth Target Fabrication Specialists' Meeting*, Taos, New Mexico, February 6–10, 1995.

Hoppe, M.L., "XRF Calibration for ICF Capsule Measurements Achieved Using GA Manufactured Standards," in the *Proceedings of the Tenth Target Fabrication Specialists' Meeting,* Taos, New Mexico, February 6–10, 1995.

Hoppe, M.L., "Use of Fill-Crate Improves Reliability and Efficiency of Hydrogen Out-Gassing Rate Measurements," in the P*roceedings of the Tenth Target Fabrication Specialists' Meeting*, Taos, New Mexico, February 6–10, 1995.

Husband, D.O., Brown, L.C., McQuillan, B.W., and Hoppe, M.L., "Production of Titanium-Doped Polystyrene Mandrels," in the *Proceedings of the Tenth Target Fabrication Specialists' Meeting*, Taos, New Mexico, February 6–10, 1995.

Kaae, J.L., "Coating of Small Particles by Chemical Vapor Deposition While the Particles are Fluidized," in the *Proceedings of the Materials Research Society Fall Meeting*, Boston, Massachusetts, December 2, 1994..

Kaae, J.L., and Wall, D.R., "The Effect of Micromachining Variables on the Surface Finish of Copper," in the *Proceedings of the Tenth Target Fabrication Specialists' Meeting*, Taos, New Mexico, February 6–10, 1995.

Mangano, R.A., Wier, W., Torres, T., and Fagaly, R.L., "Development of a Cryogenic Pressure Transducer for the UR/LLE Tritium Fill Station," in the *Proceedings of the Tenth Target Fabrication Specialists' Meeting*, Taos, New Mexico, February 6–10, 1995.

Mangano, R., and Stephens, R.B., "Destructive Tester for the Analysis of Fill Pressure and Composition of Single ICF Shells," in the *Proceedings of the Tenth Target Fabrication Specialists' Meeting*, Taos, New Mexico, February 6–10, 1995.

McQuillan, B., "Synthesis of Silicon-Containing Polymers," in the *Proceedings of the Tenth Target Fabrication Specialists' Meeting*, Taos, New Mexico, February 6–10, 1995.

Miller, W.J., Ankney, J.S., Beighley, D.H., Baugh, W.A., Brown, L.C., Gibson, J.B., Hoppe, M.L., Husband, D.O., Steinman, D.A., and Stephens, R.B., "Composite Polymer Capsule Production at General Atomics," in the *Proceedings of the Tenth Target Fabrication Specialists' Meeting*, Taos, New Mexico, February 6–10, 1995.

Monsler, M.J., "Theoretical Insight into the Thermal-Gradient Layering of Cryogenic H_2-D_2," in the *Proceedings of the Tenth Target Fabrication Specialists' Meeting*, Taos, New Mexico, February 6–10, 1995.

Monsler, M.J., Merkul'ev, Y.A., and Norimatsu, T., "Target Fabrication and Positioning," Section 3.3 of "Energy from Inertial Fusion," W.J. Hogan, editor, International Atomic Energy Agency, Vienna, ISBN 92-0-100794-9 (1995).

Overturf, G., Cook, R., Letts, S., Buckley, S., McClellan, M., and Schroen-Carey, D., "Progress in Development of Resorcinol/Formaldehyde Foam Shells," in the *Proceedings of the Tenth Target Fabrication Specialists' Meeting*, Taos, New Mexico, February 6–10, 1995.

Overturf, G.E., Buckley, S.R., Cook, R.C., and McClellan, M.R., "Process Issues Associated with Making Foam Microshells at LLNL," in the *Proceedings of the Tenth Target Fabrication Specialists' Meeting*, Taos, New Mexico, February 6–10, 1995.

Overturf, G.E., Cook, R., Letts, S., Buckley, S., McClellan, M.R., and Schroen-Carey, D., "Process Issues with Foam Shells," in the *Proceedings of the Tenth Target Fabrication Specialists' Meeting,* Taos, New Mexico, February 6–10, 1995.

Sater, J., Bittner, D., Bieri, R., Monsler, M., Sanchez, J., Bernat, T., Mapoles, E., and Giedt, W., "Liquid Hydrogen Layers in Plastic Capsules of Large Diameter," *Inst. Phys. Conf.*, **Ser. No. 140**, p. 397.

Schneir, I.G., and McQuillan, B.W., "Preparation of a Low Density Polymer Foam with Dopants to Improve Diagnostic Capabilities," in the *Proceedings of the Tenth Target Fabrication Specialists' Meeting*, Taos, New Mexico, February 6–10, 1995.

Schroen-Carey, D., Overturf III, G.E., Reibold, R., Buckley, S.R., Letts, S.A., and Cook, R., "Hollow Foam Microshells For Liquid-Layered Cryogenic Inertial Confinement Fusion Targets," J. Vac. Sci. Technol. A **13**, (1995).

Schultz, K.R., and T. Norimatsu, "Inertial Fusion Target Development for Ignition and Energy" in the *Proceedings of the IAEA Technical Committee Meeting on Drivers for Inertial Confinement Fusion*, Paris, France November 14–18, 1994.

Schultz, K.R., "Target Support for Inertial Confinement Fusion," in the *Proceedings of the Fusion Power Associates Meeting*, Washington, D.C., June 15–16, 1995, to be published in J. of Fusion Energy.

Schultz, K.R. "Inertial Fusion Target Development," in the *Proceedings of the Sixteenth Symposium on Fusion Engineering*, Urbana, Illinois, September 30 through October 1, 1995.

Simpson, J., "Point Spread Function Measurements and Maximum Entropy Deconvolution for Enhanced Image Resolution of D-T Solid Layers," in the *Proceedings of the Tenth Target Fabrication Specialists' Meeting*, Taos, New Mexico, February 6–10, 1995.

Steinman, D.A., and Hoppe, M.L., "Rapid Determination of Hydrogen Out-Gassing Rates of ICF Capsules by XRF," in the *Proceedings of the Tenth Target Fabrication Specialists' Meeting*, Taos, New Mexico, February 6–10, 1995.

Steinman, D.A., and Hoppe, M.L., "Argon Permeation Through Polyvinyl Alcohol (PVA) Coatings," in the *Proceedings of the 41st National Symposium and Topical Conferences of the American Vacuum Society,* Denver, Colorado, October 24–28, 1994.

Steinman, D.A., and Hoppe, M.L., "Argon Permeation Through Polyvinyl Alcohol (PVA) Coatings," in the *Proceedings of the Tenth Target Fabrication Specialists' Meeting*, Taos, New Mexico, February 6–10, 1995.

Stephens, R.B., "Precision Shell Characterization Using Radial Averaging of X-Ray Images," in the *Proceedings of the Materials Research Society Conference*, November 24 through December 2, 1994.

Stephens, R.B., "Precision Shell Characterization Using Radial Averaging of X-Ray Images," in the *Proceedings of the 41st National Symposium and Topical Conferences of the American Vacuum Society*, Denver, Colorado, October 24–28, 1994.

Stephens, R.B., "Light Scattering Limitations to Interferometric Characterization of Foam Shells," in the *Proceedings of the Tenth Target Fabrication Specialists' Meeting*, Taos, New Mexico, February 6–10, 1995.

Stone, G.F., Rivers, C.J., Spragge, M., and Wallace, R.J., "Fabrication and Testing of Gas Filled Targets for Large Scaled Plasma Experiments on NOVA," in the *Proceedings of the Tenth Target Fabrication Specialists' Meeting*, Taos, New Mexico, February 6–10, 1995.

Wilemski, G., Cook, R., Boone, T., Cheung, L., and Nelson, D., "Prediction of Phase Separation During the Drying of Polymer Shells," in the *Proceedings of the Tenth Target Fabrication Specialists' Meeting*, Taos, New Mexico, February 6–10, 1995.